SECONDARY PYROELECTRIC AND ELECTROCALORIC EFFECTS IN THIN FILMS

BY

TRONG TONG

DISSERTATION

Submitted in partial fulfillment of the requirements
for the degree of Doctor of Philosophy in Materials Science and Engineering
in the Graduate College of the
University of Illinois at Urbana-Champaign, 2015

Urbana, Illinois

Doctoral Committee:

Professor David G. Cahill, Chair
Professor Pascal Bellon
Professor Dallas R. Trinkle
Professor Shen J. Dillon

ABSTRACT

The pyroelectric and electrocaloric effect play an important role in many applications such as energy harvesting and solid-state cooling. This dissertation focuses on the characterization of the pyroelectric and electric coefficient in thin film using novel laser-based technique. The implementation of the systems is described in detail, and heat transport models are developed to interpret the experimental data. The temperature oscillation caused by the modulated laser power or the entropy change are calculated over a wide range of the modulation frequency. These techniques are applied to characterize $Pb(ZrTi)O_3$ and $Ba(SrTi)O_3$ films growth by Pulse Laser Deposition (PLD) and sol-gel method.

The secondary pyroelectric and electrocaloric contributions caused by clamping substrate effect are discussed. A wide range frequency analysis is applied to extract the secondary pyroelectric coefficient. The secondary pyroelectric effect is found to have the same dependence on applied field as the pyroelectric coefficient and is approximately 15% and 20% of the total response for $PbZr_{0.2}Ti_{0.8}O_3$ and $Ba_{0.6}Sr_{0.4}TiO_3$ grown by PLD, respectively. By comparing the pyroelectric and electrocaloric coefficient measured on the same devices, our result shows the secondary contribution to the

electrocaloric coefficient has the opposite sign as the primary effect and therefore reduces the overall entropy change of $Pb(ZrTi)O_3$ in an electric field. Finally, the sol-gel method is used to produce $Pb(ZrTi)O_3$ thin films. The sample fabrication is described in detail along with physical characterization and the pyroelectric measurement. Sol-gel PZT films are perovskite phase with (100) orientation. The pyroelectric coefficient is measured to be 135 μC m^{-2} K^{-1}.

ACKNOWLEDGEMENTS

Firstly, I would like to give many thanks to my advisor, Prof. David G. Cahill. He gave me an amazing opportunity to study for my PhD in an excellent institution, University of Illinois Urbana Champaign. His sharp ideas, excellent supports guided me through most difficult time during my PhD. What I have learnt from him is how to address and evaluate scientific problems, how to approach them in clever ways and last but not least how to do solid findings. I am also grateful to the other members of my thesis committee, Prof. Pascal Bellon, Prof. Dallas R. Trinkle and Prof. Shen J. Dillon for their guidance.

I enjoyed working with Prof. Lane W. Martin and his group members: Dr. Karthik Jambunathan, Dr. Anoop Damodaran, and Dr. Vengadesh Mangalam. Many great ideas and many excellent samples are produced. Thank you a lot.

I also cannot finish my PhD without valuable discussions with many collaborators: Prof. William P. King, Dr. Bikram Bhatia, Prof. Junquiao Wu, Dr. Deyi Fu, Dr. Alejandro Levander. Dr. Geoff L. Brennecka, Prof. David A. Payne. I really appreciate your help.

I have benefited from a lot of discussions with other members in Prof. Cahill's group: Richard Wilson, Joseph Feser, Gregory Hohense, Dongyao Li, Ji Yong Park, Jonlgo Park, Dongwook Oh, Tamlin Mathews, Andrew Hafeli, Gyungmin Choi, Jun Liu, and Yee Can Koh. Thank you very much.

I would like to thank to my parents, my younger sisters for their invariable presence and support.

Finally, my warmest gratitude goes to my wife, Thuy and my 3 years old daughter, An, for their encouragement, love and constant support.

A part of this work was supported by the Air Force Office of Scientific Research under Grant AF FA 9550-11-1-0073. The study of pyroelectric effects and materials was supported by the Office of Naval Research under Grant N00014-10-10525. The development of compositionally graded pyroelectric/electro-caloric layers was supported by the Defense Advanced Research Projects Agency (DARPA) under Grant N66001-11-1-4195 and the Army Research Office under Grant W911NF-10-1-0482. Experiments were carried out, in part, in the Materials Research Laboratory Central Facilities, University of Illinois, Urbana-Champaign.

TABLE OF CONTENTS

LIST OF FIGURES.....viii

CHAPTER 1 INTRODUCTION.....1

CHAPTER 2 PYROELECTRIC MEASUREMENT.....8
2.1 Introduction..... 8
2.2 Sample preparation and thermal conductivity measurement..... 10
2.3 Pyroelectric measurement setup..... 10
2.4 Heat transport theory..... 17
2.5 Temperature calculation..... 21
2.6 Experimental data..... 28
2.7 Sensitivity of the pyroelectric measurement..... 37

CHAPTER 3 SECONDARY PYROELECTRIC EFFECT OF THIN FILMS.39
3.1 Background and theory..... 39
3.2 Sample preparation..... 42
3.3 Measurement of Secondary Pyroelectric Effect..... 43
3.4 Conclusion..... 50

CHAPTER 4 ELECTROCALORIC MEASUREMENT.....52
4.1 Introduction..... 52
4.2 Electrocaloric measurement..... 53
4.3 Heat transport theory..... 55
4.4 Sensitivity of the electrocaloric measurement..... 60
4.5 Verifying the thermoreflectance coefficient measurement..... 61

CHAPTER 5 ELECTROCALORIC EFFECT OF THIN FILMS.....63
5.1 Background and theory..... 63
5.2 Sample preparation..... 68
5.3 Measurement of the pyroelectric and electrocaloric coefficient of PZT epitaxial layers..... 70
5.4 Field dependence of the pyroelectric and electrocaloric coefficients 73
5.5 Temperature dependence of the pyroelectric and electrocaloric coefficients..... 76
5.6 Conclusion..... 79

CHAPTER 6 PYROELECTRIC EFFECT OF SOL-GEL PZT THIN FILMS.80
6.1 Introduction 80
6.1.1 Precursor solution preparation 81
6.1.2 Deposition and crystallization of PZT thin films 83
6.2 PZT thin film characterization 84
6.3 Pyroelectric measurement 87
6.4 Conclusion 90

CHAPTER 7 CONCLUSIONS 91

APPENDIX A THERMAL CONDUCTIVITY OF InGaN ALLOYS 94
A.1 Introduction 94
A.2 Sample preparation 95
A.3 Sample characterization 96
A.4 Results 100
A.5 Calculation of the thermal conductivity of InGaN alloys 101
A.6 Comparison between experimental data with modeling 105
A.7 Conclusion 108

REFERENCES 109

LIST OF FIGURES

Figure 2.1 Schematic description of the pyroelectric measurement..... 12
Figure 2.2 Detail of optical setup of the pyroelectric measurement..... 13
Figure 2.3 Schematic diagram of connection of the devices to external instrument and the equivalent circuit..... 14
Figure 2.4 A typical configuration of our samples in which a Gaussian-shape laser beam with a power P_0 and $1/e^2$ radius w_0 is absorbed at the top layer (V). The ferroelectric film is sandwiched between two electrodes. In general, two electrode does not need to be the same material and number of layers is not limited. For example, for our samples, the top electrode includes two layers: $SrRuO_3$ and V..... 18
Figure 2.5 1D heat transport in a homogenous slab 18
Figure 2.6 Temperature oscillation $T(f, r, z)$ at the interface between the film and the top electrode ($z = 0$) as a function of radius r at different frequencies from 1 Hz to 10 MHz. The laser power P_0 = 1 mW, the laser spot size w_0 = 10 μm. The sample structure includes 150 nm V/20 nm $SrRuO_3$/150nm $Pb(ZrTi)O_3$/20 nm $SrRuO_3$/DSO substrate.22
Figure 2.7 Temperature oscillation $T(f, r, z)$ as a function of distance z at radius $r = 0$ and different frequencies from 1 Hz to 10 MHz. The laser power P_0 = 1 mW, the laser spot size w_0 = 10 μm. The sample structure: 150 nm V/20 nm $SrRuO_3$/150nm $Pb(ZrTi)O_3$/20 nm $SrRuO_3$/DSO substrate. 23
Figure 2.8 The average temperature within the top electrode radius and PZT film thickness as a function of frequency from 1 Hz to 10 MHz. The laser power P_0 = 1 mW, the laser spot size w_0 = 10 μm, the top electrode radius a = 50 μm. The sample structure: 150 nm V/20 nm $SrRuO_3$/150nm $Pb(ZrTi)O_3$/20 nm $SrRuO_3$/DSO substrate. 26
Figure 2.9 The phase angle between $T_{avg}(f)$ and the heat flux at the surface of the sample. 27
Figure 2.10 The average temperature within the top electrode radius and film thickness as a function of frequencies from 1 Hz to 10 Mhz for PZT film thicknesses of 100 nm, 1 μm and 10 μm. The laser power P_0 = 1 mW, the laser spot size w_0 = 10 μm, the top electrode radius a = 50 μm. The sample structure: 150 nm V/20 nm SRO/ PZT/20 nm SRO/DSO substrate. 29

Figure 2.11 The pyroelectric current calculated from Eq. (2.13) as a function of frequency. The pyroelectric coefficient is set to be 1. The laser power P_0 = 1 mW, the laser spot size w_0 = 10 μm, the top electrode radius a = 50 μm. The sample structure: 150 nm V/20 nm SRO/ PZT/20 nm SRO/DSO substrate. 30
Figure 2.12 The measured pyroelectric current as a function of frequency at 1st, 3rd and 5th harmonics without a low-pass filter. The sample structure is Pt(150nm)/Cr(10nm)/PZT(180nm)/SRO(25nm)/DSO. The laser power is 5 mW, laser spot size is 4.7 μm. Note that the frequencies at 3rd and 5th harmonics are scaled by a factor of 3 and 5 respectively for easy comparison. 32
Figure 2.13 Relative phases of the oscillating heat flux, *F*, temperature oscillations created by the heat flux, *T(f)*, and the measured ac current, *I(f)*. When non-pyroelectric currents are negligible in comparison with the pyroelectric current, the measured current leads the temperature change by 90°. The temperature change lags the heat flux by a phase angle, , that depends on frequency. The phase angle of the current, , is measured by the lock-in amplifier. 33
Figure 2.14 The phase shift introduced by electrical components measured by replacing the sample with a photodiode. 34
Figure 2.15 Frequency dependence of the amplitude of the pyroelectric current. Measured data are shown as open circles and the solid line is the model calculations for a fixed value of the pyroelectric coefficient. (b) The measured phase angle of the current (open circles),, and the phase angle of the pyroelectric current (solid line) calculated from the phase angle of the temperature, for the BST/STO sample at zero bias voltage. The good match between the measured and calculated phase supports our assertion that non-pyroelectric currents are negligible in these experiments. The sample structure is V(150 nm)/ SRO (20 nm)/ $BaSrTiO_3$ (150 nm)/ SRO(25nm)/ $SrTiO_3$. The laser power is 6 mW, laser spot size is 10.3 μm. 35
Figure 2.16 Sensitivity of the calculated amplitude of the temperature oscillations, see Eq. (2.15), as a function of selected parameters in the thermal model as a function of heater frequency for a PZT film on a DSO substrate. The radius of the top contact is 50 μm. Sensitivity to the laser power is unity. 38
Figure 3.1 Frequency dependence of the pyroelectric coefficient of the $Ba_{0.6}Sr_{0.4}TiO_3$ layer grown on a $SrTiO_3$ substrate. The radius of the top contact of the devices is (a) 50 μm and (b) 100 μm. 44
Figure 3.2 Hysteresis of the pyroelectric coefficient of PZT and BST films measured at 20 Hz and 20 kHz at room temperature. The x-axis of each plot is the DC bias voltage that is applied to the capacitors.

The time between changes in the bias voltage is ~30 s and the increment between values of the bias voltate is 0.2 V. 46
Figure 3.3 Secondary pyroelectric coefficient of PZT and BST films due to the thermal expansion mismatch between the film and substrate as a function of the bias voltage. The right-hand axis of each plot is corresponding converse piezoelectric coefficient d_{31} calculated based on Eq.(3.3). 50
Figure 4.1 Schematic description of the electrocaloric measurement 53
Figure 4.2 Detail of the optical setup of the electrocaloric measurement 54
Figure 4.3 Thermal model for bidirectional heat conduction into the V film and substrate. The film is divided into thin slabs with the thickness of dz. The heat flux of each slab, *dF*, creates a temperature change at the sample surface. The total temperature is sum of the temperature changes . is the heat transport matrix for a part of the sample at a distance *z* from the bottom layer and is the heat transport matrix for a part of the sample at a distance *z* from the top layer. 58
Figure 4.4 Temperature change at the top electrode as a function of frequency for different film thicknesses (h = 100 nm, 200 nm and 1 μm). The electrocaloric coefficient μC m^{-2} K^{-1}; Amplitude of applying voltage E_0 = 1 V; T = 300 K. Sample structure: V (150 nm)/ SRO (20 nm)/ PZT (h)/ SRO (20 nm)/ DSO 59
Figure 4.5 Sensitivity of the calculated temperature change at the top electrode, see Eq.(4.9), as a function of selected parameters in the thermal model as a function of frequency for a PZT film on a DSO substrate. 61
Figure 4.6 A schematic of the 2-omega method to measure the thermoreflectance coefficient. 62
Figure 5.1 a) Frequency dependence of the pyroelectric current; and (b) frequency dependence of the temperature change of the V film for a PZT/GSO capacitor at room temperature. Measured data are shown as open circles and the solid lines are the model calculations used to determine (a) the total pyroelectric coefficient Π = -170 μC m^{-2} K^{-1}; and (b) the total electrocaloric coefficient, Σ = -130 μC m^{-2} K^{-1}. The laser power used in the pyroelectric measurement is 1 mW. The DC bias voltage and AC voltage used in the electrocaloric measurement are 1.4 V and 1 V, respectively. 71
Figure 5.2 Hysteresis measurement of the total pyroelectric, electrocaloric coefficient and polarization of the PZT layers at room temperature. For the electrocaloric and pyroelectric measurements, a DC bias voltage is applied to the capacitors and the time between changes in the bias voltage is ~30 s with a increment of 0.1 V. Polarization is measured at a frequency of 1 kHz. 75

Figure 5.3 Dependence on sample temperature of the total electrocaloric (triangle symbols) and pyroelectric (square symbols) coefficients of PZT epitaxial layers on $DyScO_3$ and $GdScO_3$ substrates. 77
Figure 5.4 Temperature dependence of the *difference* between the total electrocaloric coefficient and pyroelectric coefficient of PZT epitaxial layers due to the secondary contribution. The converse piezeoelectric coefficient d_{33} calculated based on Eq. (5.6). The error bar is calculated with uncertainties of the pyroelectric and electrocaloric measurement to be 5%..... 78
Figure 6.1 Schematic of the PZT solution precursor preparation..... 83
Figure 6.2 X-ray diffraction patterns of PZT thin films at different annealing temperatures. A pattern of the substrate is included for comparison. 85
Figure 6.3 RBS measurement of PZT thin films with one (a) and two (b) spin coating layers 86
Figure 6.4 Frequency dependence of the amplitude of the pyroelectric current of the PZT film with the thickness of 174 nm. Measured data are shown as open circles and the solid line is the model calculations for a fixed value of the pyroelectric coefficient. The laser power is 10 mW. The top electrode radius is 50 μm. 88
Figure 6.5 The frequency dependence of the average temperature amplitude and phase angle of the PZT film on Pt/Ti/SiO2/Si substrate..... 89
Figure A.1 (a) XRD θ-2θ scan patterns for selected $In_xGa_{1-x}N$ samples in the vicinity of the (0002) reflection. (b) XRD c-lattice parameter of $In_xGa_{1-x}N$ *(fig. A.1 cont.)* alloys vs. In composition measured by RBS. The solid line shows the prediction of Vegard's law; the good agreement suggests that the $In_xGa_{1-x}N$ layers are fully relaxed. (c) Full-width-at-half-maximum (FWHM) of the $In_xGa_{1-x}N$ (0002) reflection vs. In composition. 98
Figure A.2 (a) The thermal conductivity (Λ) at room temperature of $In_xGa_{1-x}N$ alloys as a function of In fraction compared to the predictions of the modified Callaway model. Previously reported thermal conductivities of GaN, InN and $In_xGa_{1-x}N$ alloys are included for comparison. The open-square and open-circle is the thermal conductivity of pure GaN (Ref. [106]) and pure InN (Ref. [107]) respectively. The dashed line is calculated for the limit of large layer thickness; the solid line is calculation for a layer thickness of d = 200 nm. (b) Ratio of the measured thermal conductivity from this work to the calculated thermal conductivity (Λ_{DCM}) at each thickness as a function of In content. 102

CHAPTER 1

INTRODUCTION

Pyroelectricity describes the change in the polarization of a material with temperature. The polarization change is explained by a displacement of cation centers to anion centers caused by the asymmetry of the potential energy[1]. The pyroelectric effect is commonly used in heat sensing, detectors of infrared radiation, thermal imaging and energy harvesting. [1-3]. For pyroelectric harvesting applications, Bowen *et. al*[3] provided a recent review of energy harvesting of pyroelectric effect and comparison with piezoelectric energy harvesting, potential materials and electronic systems for energy storage. Sebald *et al.*[4] proposed using cyclic pumping to increase energy conversion efficiency by increasing the heat oscillation frequency.

Although the theory of the pyroelectric effect has been developed back to 1970, the physics of pyroelectricity is still poorly understood at microscopic scale. [5-7]Recently, using molecular dynamic to study $LiNbO_3$, Peng *et al.* showed that pyroelectricity stems from the anharmonic change in crystal structure with temperature.[8] The total pyroelectric effect comes from primary and secondary contributions. The primary contribution is the change of polarization under constant strain condition. [9,10]. The secondary

contribution comes from the change of the polarization due to thermal expansion induced strain via the piezoelectric effect. [1,9-13]. The primary contribution has two parts: intrinsic and extrinsic. [9]The intrinsic part arises from the change of polarization in single domains while the extrinsic part is due to the domain wall movement.

There has been a lot of effort to study the secondary effect. A calculation by Zook *et al.*[13] indicated that the pyroelectric response is reduced in clamped thin films. Whatmore *et al.*[1] showed that if frequencies of alternating heat flux matches the mechanical resonance frequencies, the secondary effect can be important. The secondary pyroelectric coefficient is also enhanced by laminate structures due to different thermal expansion and stiffness.[14]. Yang *et al.*[15] replaced thin films by a ZnO nanowire arrays which provide good stability and high characteristic coefficient of heat flow conversion into electricity, ~ 0.05 - 0.08 Vm^2/W. Recently, Karthik *et al.*[9] pointed out that the secondary contribution could be as large as 50% of the total effect.

The pyroelectric measurement involves measuring either the spontaneous polarization or currents created by the change of charges at surfaces of materials in response to change of the polarization.[11] It is often categorized into three groups based on methods to temperature of materials. 1) Constant temperature measurement: [16-18] the polarization is measured using the Sawyer-Tower bridge at different temperatures. 2) Temperature

ramp techniques[19-22]: the pyroelectric current flow between two contacts is collected under continuous heating or cooling. 3) Periodic temperature change techniques: Materials are heated by periodic heat sources such as a modulated light source or laser. [23,24]

The electrocaloric effect is an inverse effect of the pyroelectricity which describes the reversible temperature change of materials under an applied electric field. This effect has potential application in energy scavenging and solid-state refrigeration [25,26] The physics of the electrocaloric effect is even less understood than the pyroelectric effect because measuring the entropy change is challenging and the secondary effects are not well understood.

At macroscopic level, a general consideration of the electrocaloric effect is based on the Maxwell relation between the entropy and electric displacement:

$$\left(\frac{dS}{dE}\right)_{T,\varepsilon \text{ or } \sigma} = \left(\frac{dP}{dT}\right)_{E,\varepsilon \text{ or } \sigma} \tag{1.1}$$

Where $\frac{dP}{dT}$ is the pyroelectric coefficient, $\frac{dS}{dE}$ is the electrocaloric coefficient, T is the ambient temperature, ε is strain, σ is stress, E is electric field. The adiabatic temperature change ΔT_a can be expressed as:

$$\Delta T_a = -T \int_{E_1}^{E_2} \frac{1}{C}\left(\frac{dP}{dT}\right)_{E,\varepsilon \text{ or } \sigma} dE \tag{1.2}$$

C is the heat capacity. This relation indicates that, to achieve a large electrocaloric temperature change, the materials have to possess a large

pyroelectric coefficient over a broad electric field. Noted that this relation does not take into account the field induced phase transition contribution, e.g., the field induced structural transition[27]. The electrocaloric effect can be also derived from the Landau-Devonshire phenomenological theory[28], in which the Gibbs free energy of a ferroelectric material is expressed as a function of the polarization P, electric field E and stress σ. In general, the model predicts that a large electrocaloric effect can be achieved at close proximity of the Curie temperature.[29] [28,30]Furthermore, the strain due to thermal expansion mismatch, domain wall displacement or the clamping effect of a substrate can play an important role in enhancing the total electrocaloric response. [29,31,32]. These contributions are often considered as the secondary electrocaloric effect.

Electrocaloric measurement can be categorized into two groups: "direct" and "indirect". The indirect method[33] is based on the thermodynamic Maxell relation (See Eq. (1.1)). The pyroelectric coefficient is measured as a function of the electric field, and then the electrocaloric temperature change is calculated from Eq. (1.2). Because of difficulties in measuring the pyroelectric coefficient directly, the polarization is often measured as a function of temperature instead. The indirect method was the approach used in many recent studies. Mischenko *at al.* measured a giant electrocaloric effect of ΔT=12 K for $PbZr_{0.95}Ti_{0.05}O_3$ produced by an electric field of 480 kV cm^{-1} at an initial temperature of 220 ^{o}C.[34] A large

electrocaloric effect (~ 12°C) in the ferroelectric poly (vinylidene fluoride-trifluoroethylene- chlorofluoroethylene) (P(VDF-TrFE)) copolymer was also reported by Neese *at al.*[35]. Peng *et al.* used the indirect method to characterize relaxor ferroelectric $Pb_{0.8}Ba_{0.2}ZnO_3$ thin films which shows a giant $\Delta T = 45.3$ K at the transition temperature.

In the direct method, the temperature or heat flux is measured directly using thermometers or calorimeters. [36-39] Studies by Kar-Narayan *et al.*[36], Lu *et al.*[39] and Bai *et al.*[40] have revealed disagreement between the direct and indirect methods. Good agreement was found by Goupil *et al.*[41] and in the first principles simulations of Ponomareva *et al.*[42].

The use of thin epitaxial layers enables great flexibility for engineering the properties of the ferroelectric layers by varying epitaxial strain, composition and thickness. [43-47] However, accurate characterization of epitaxial layers confronts many challenges.[26] Thermally stimulated leakage current can dominate the pyroelectric current at high temperature and fields[48] and so limits understanding of the physics of pyroelectricity. Measuring the temperature or entropy change of the epitaxial layers is even more challenging compared to bulk materials. Therefore, better approaches are needed to advance the understanding of these effects in thin films.

The main objective of this dissertation is to develop novel laser-based methods to characterize the pyrolectric and electrocaloric effect of thin films.

These techniques enable us to measure directly the secondary contribution to the pyroelectric and electrocaloric effect.

This dissertation is organized as follows:

Chapter 2 presents the wide frequency range, laser-based pyroelectric technique. The design and implementation of the pyroelectric system are developed from Time Domain Thermoreflectance (TDTR) setup. A heat transport model to calculate the temperature oscillation caused by the modulated laser power is described in detail. Sample preparation, thermal response, detail setup, phase correction and sensitivity of the measurement to parameters in each frequency regime are discussed.

In Chapter 3, the pyroelectric measurement technique is applied to characterize (BaSr)TiO_3 (BST) and Pb(ZrTi)O_3 (PZT) epitaxial films grown on $SrTiO_3$, $DyScO_3$ and $GdScO_3$ by pulse laser deposition (PLD). With a wide frequency range (1 Hz – 10 MHz), this method provides a unique way to measure the secondary pyroelectric effect in thin films clamped on substrates by analyzing the difference between the pyroelectric coefficients at high and low frequencies. A theory of the substrate clamping effect in thin films is described. The secondary pyroelectric effect is found to be approximately 15% and 20% of the total response for PZT and BST films respectively and has the same dependence on applied field as the pyroelectric coefficient.

In Chapter 4, we present a laser-based electrocaloric technique to measure the electrocaloric effect directly. Implementation, heat transport

model to relate the measured temperature at the sample surface to the heat flux created by the electrocaloric effect and sensitivity of the technique to parameters are described in detail.

In Chapter 5, we discuss the applications of the pyroelectric and electrocaloric techniques to measure the pyroelectric and electrocaloric effects of PZT epitaxial layers as a function of temperature and electric field. Using ability to measure both the pyroelectric and electrocaloric coefficient independently, we can quantify the secondary electrocaloric contribution to the total electrocaloric effect, which is created by a combination of piezoelectric and elastocaloric effects.

In Chapter 6, we turn to PZT films fabricated by sol-gel method, which has been mainly used to create materials with a giant electrocaloric effect. Details of fabrication process are described. XRD and RBS measurement is used to characterize crystal structure, composition and thickness of films. PZT films have (100) preferred orientation and tetragonal symmetry. The pyroelectric coefficient is measured to be ~ 135 W m^{-2} K^{-1} and the secondary contribution is not observed.

CHAPTER 2

PYROELECTRIC MEASUREMENT

Sections of this chapter have been published in "Secondary pyroelectric effect of epitaxial layers revealed by wide-frequency range measurement of the pyroelectric coefficient", T. Tong, J. Karthik, Lane W. Martin, and David G. Cahill, Phys. Rev. B **90**, 094116 (2014) and "Reduction of the electrocaloric entropy change of $PbZr_{0.2}Ti_{0.8}O_3$ epitaxial layers due to an elastocaloric effect", T. Tong, J. Karthik, R. V. K. Mangalam, Lane W. Martin, and David G. Cahill, Phys. Rev. B **90**, 094116 (2014)

2.1 Introduction

In this chapter, we describe the wide range frequency pyroelectric measurement using modulated intensity laser combined with multilayered thermal transport model. The pyroelectric coefficient is defined as the change of the spontaneous polarization to the temperature $\Pi = \frac{dP}{dT}$, here P is the polarization and T is temperature. To facilitate the measurement of the pyroelectric coefficient, a capacitor structure often is fabricated with top and bottom electrodes and materials under study sandwiched in between. The temperature then is changed either using a heating stage with periodic

temperature change[9] or light[23] [24], which is absorbed to produce the temperature change. The pyroelectric current response to the polarization change is described as following:

$$i = \frac{dP}{dt} = \frac{dP}{dT}\frac{dT}{dt} = \Pi\frac{dT}{dt} \tag{2.1}$$

Here t is time. We noted that for small temperature change ΔT , dP/dT could be considered a constant at that temperature and the current only depends on the rate of temperature change. This means the faster temperature change, the higher response current. Hence, it is difficult to achieve a large current using the heating stage-based method with low frequency temperature change. The light-based method can overcome this limitation. In 1955, Chynoweth[23] at Bell Laboratory developed a dynamic method to measure the pyroelectric effect. Although, it does not provide a quantitative calculation for the pyroelectric coefficient, it provided a good direct method to study the pyroelectric effect under applied electrical field and at elevated temperature. Later, Lang *et al.* developed the Laser Intensity Modulation Method (LIMM) [24] to measure the spatial distribution of polarization. The frequency modulation of the laser intensity of LIMM is from 100 Hz to 100 kHz.

We constructed a wide range frequency measurement system, which allows us to measure the pyroelectric coefficient of thin films. This system combines an optical setup to and a novel analytical model, which enable to calculate the temperature change within the thin films under periodic

heating of the laser power. Below, we will present the optics and electrical instrumentation.

2.2 Sample preparation and thermal conductivity measurement

Capacitor structures are fabricated to facilitate the pyroelectric measurement. Layers under study are deposited on substrates which have electrically conductive layers on top. These layers will play a role as the bottom electrodes of the devices. Circular top electrodes with radius of 50 μm and 100 μm are patterned by photolithography. Any metal which can efficiently absorb the laser power can be used as the top electrode. Here, we choose Vanadium (V) because of its compatibility with the fabrication process. The thermal conductivity of V is measured by a 4-point probe system. The thermal conductivity of the films is measured by Time Domain Thermoreflectance technique. [49] The thickness of the V layer is measured by picosecond acoustics. [50]

2.3 Pyroelectric measurement setup

Figure 2.1 is the schematic diagram of the pyroelectric measurement. A laser modulated by an Electro-Optic Modulator (EOM) is focused on a capacitor structure to create temperature oscillations. The pyroelectric current is measured by a lock-in amplifier, which is synchronized with the laser modulation by a function generator. We modified the available optical

setup of Time Domain Thermorefectance (TDTR) [49] technique at Materials Research Laboratory at Illinois (UIUC). The schematic in Figure 2.2 includes the essential components of our system. The Ti:sapphire vertically polarized laser emits a train of pulses with duration of ~ 0.1ps and repetition rate of ~ 80 MHz. The wavelength is tunable between 710-900 nm. The laser beam is passed through an optical isolator to prevent the back reflections and is attenuated by combining a ½ waveplate with a polarizer in the optical isolator. The beam is split into a pump and probe beam by a polarized beam splitter (PBS). The power of the pump beam is modulated by an Electro-Optic Modulator (EOM) at frequency f (f = 1 Hz – 10 MHz) to create a square-wave modulation on the beam. The bias voltage is adjusted to minimize the output laser power (below 1% of the total power) when the EOM is in the OFF state. To do that, we set the modulation frequency below 1Hz then measure the laser power while adjusting the bias voltage. The laser power measured after the EOM is ~ 1 – 10 mW. The laser beam then is focused on the sample surface using an objective lens. In our lab, objective lens 2X, 5X, 10X and 20X are used to create rms laser spot sizes of ~ 28, 11.7, 6.1 and 2.7 μm respectively. A CCD camera placed on the path of the reflective beam from the sample surface plays a role as a microscope. It enables imaging of the sample surface to know if the laser is focused on the sample surface and where the laser beam is focused on. It also helps to position the micro tip to make contact with the top electrode of samples. The Ti:Sapphire laser is used

in our setup due to its availability of MRL facility, however in principle, we can use either continuous or pulse laser.

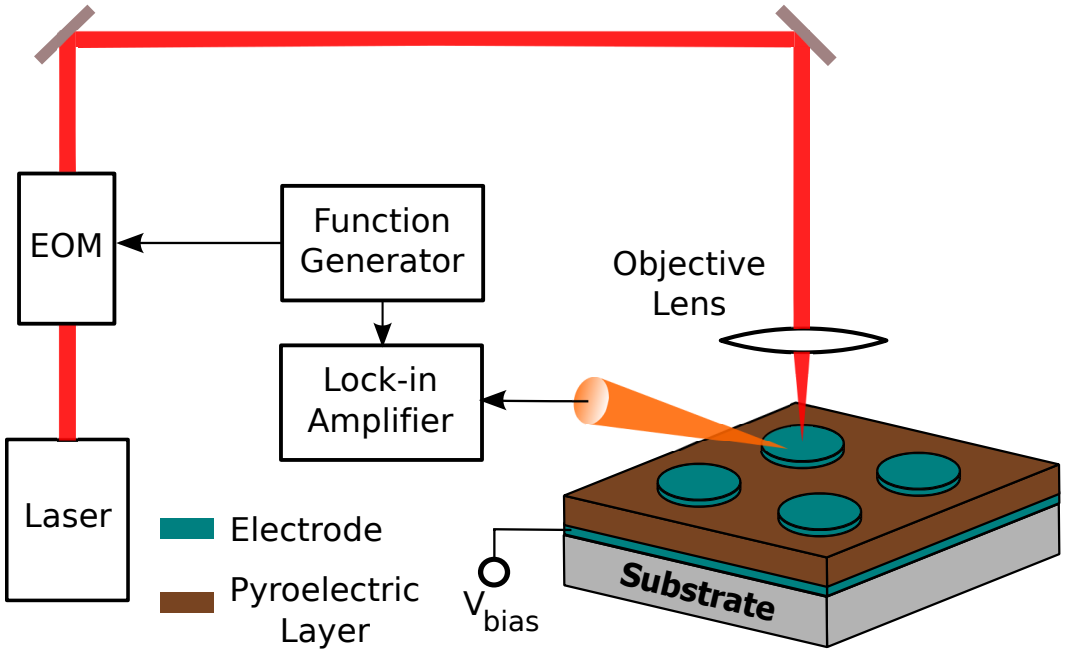

Figure 2.1 Schematic description of the pyroelectric measurement

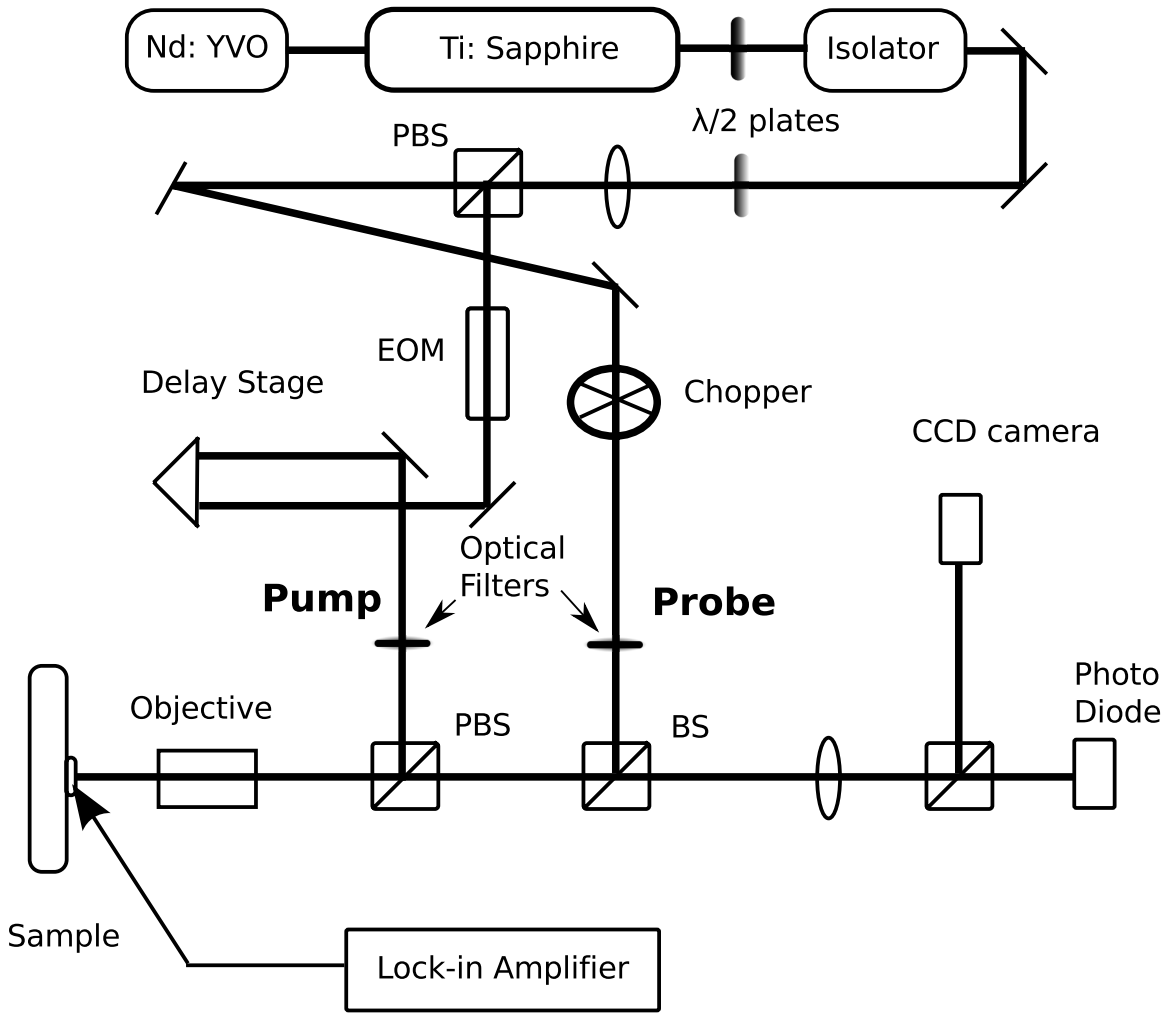

Figure 2.2 Detail of optical setup of the pyroelectric measurement

The samples are mount to a stage using conductive silver paint. We use a micro tip to make contact with the top electrode and a micro-positioner to move the tip precisely within micrometer range. The contact with the bottom electrode can be made easily by scratching the samples and then pouring the conductive silver paint on top of it. We only need to make sure the scratches are deep enough to touch the bottom electrode. Often, it is good enough to make a contact by pouring the silver paint over the edge of the samples. It is convenient for positioning the tip with the help of the CCD

camera if using only one probe tip. We use the Signatone Shield probe tip holder which includes a 24" 50Ω mini coax cable with BNC termination. The cable is then connected to the external equipment, e.g., the lock-in amplifier through 50Ω BNC cable. To apply voltage on the samples, a programmable power supply is used. The circuit is described in Figure 2.3

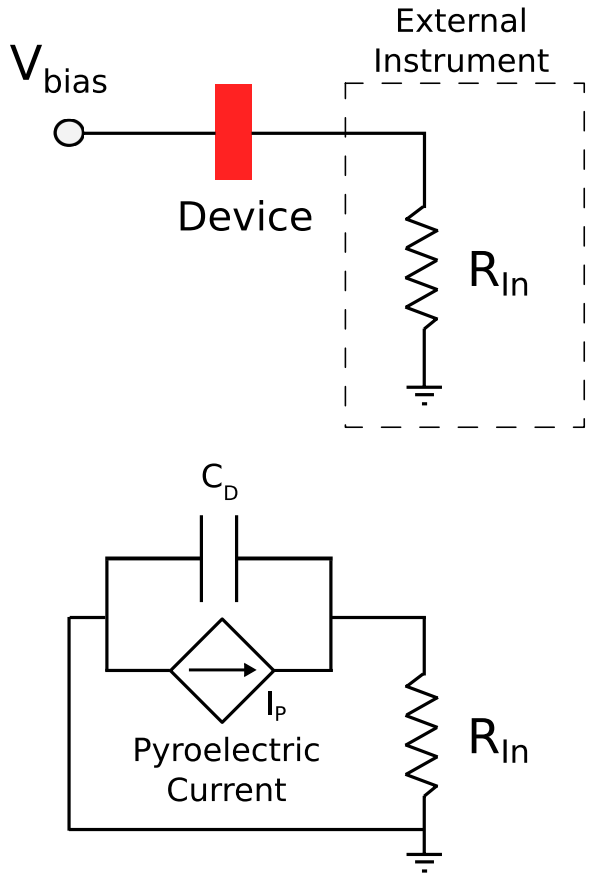

Figure 2.3 Schematic diagram of connection of the devices to external instrument and the equivalent circuit.

R_{In} is the input impedance of external instrument. Here we can describe the device and effect of the capacitance of the cable by an equivalent circuit which includes a capacitor, C_D and a current source, I_P in parallel. C_D is effective capacitor of the device and cables. If the total capacitance Z_C =

$1/\omega C_D >> R_{In}$ the capacitance will have no effect on the measurement. There are several ways to prevent the capacitance effect: 1) use low input impedance; 2) minimize the device capacitor by reducing the top electrode area and the cable capacitor by reducing the length of the cable; 3) use low modulation frequencies. When taking into account the capacitance, the signal will be suppressed by a factor $1/(iR_{In}C_D\omega + 1)$.

To maximize signal-to-noise ratio, we used three different configurations for three frequency regimes. For low frequency regime, f < 1 kHz, the devices are connected directly to an audio-frequency lock-in amplifier (SR830) operating in the current mode. In this mode, the input impedance of SR830 is 1 kΩ and the pyroelectric current will pass through this resistor to convert into a voltage signal which will be measured by the lock-in amplifier. Advantage of working in this current mode is that the lock-in amplifier can measure very small currents (~pA). Hence it is suitable for measuring the pyroelectric current which is very small at low frequencies while the effect of the capacitance is negligible. At higher frequencies, the capacitance will reduce the signal. For 1 kHz < f < 100 kHz, to minimize the effect of the capacitance, the devices are connected to a low noise pre-amplifier (SR445A) before passing through the lock-in amplifier. Noted that the upper limit frequency 100 kHz is determined by the highest working frequency of the lock-in amplifier SR830. The pre-amplifier has an input impedance of 50 Ω which will suppress the capacitance effect. The output of

the preamplifier is connected to SR830 which is set to the voltage mode. In the voltage mode, SR830 has high-Z impedance. The gain of the preamplifier is 2 times higher than the setting value because it is fed to a high-Z load.

For 100 kHz < f < 10 MHz, we used the rf lock-in amplifier (SR844) instead of SR830. The most important difference between SR844 and SR830 is that SR830 can measure harmonic of frequencies separately while SR844 is mixed with a square-wave signal as a result, it detects all odd harmonics. To remove that odd harmonics, we used a programmable low-pass filter. Because the filter has the input impedance of 50 Ω, we removed the preamplifier then replaced it by the filter. The attenuation slop is set to be 24dB/octave and gain is 1. We found that the cut-off frequency 2 times higher than the modulation frequency is good enough to remove the odd harmonics.

The function generator generates the square-wave signal at the frequency f for the EOM and plays a role as the reference signal for the lock-in amplifier. All equipment (lock-in amplifier, function generator, programmable filter, programmable power supply) are controlled by a computer via GPIB ports by Labview. The output of the lock-in amplifier has two parts: in-phase X and out-of-phase Y. These values are in-phase and out-of-phase components of the measured pyroelectric, which are recorded, then fit with a thermal transport model to extract the pyroelectric coefficient.

2.4 Heat transport theory

In our measurement, the samples are heated by a periodic heat source, specifically a laser power modulated by a square wave at frequency *f*. This will create a temperature change which has two parts: a steady-state temperature change (DC part) and a oscillating temperature change which includes first harmonic *f* and its odd harmonics 3*f*, 5*f* ... However, as described above, only first harmonic is measured, hence we can consider the heat source as an sinusoidal wave power $P = P_0 e^{i\omega t}$ with amplitude P_0 related to the measured laser power after EOM P_m by $P_0 = \frac{4}{\pi} P_m$. Eq. (2.1) can be written in frequency domain as

$$I(\omega) = \Pi i\omega T(\omega) \tag{2.2}$$

Therefore, the central problem here is to calculate the temperature $T(\omega)$ to extract the pyroelectric current Π.

The multiple-layer heat transport problem by a periodic heating source is solved very nicely in TDTR technique[49], and later expanded and solved for the bidirectional heat transport problem by Schmidt[51]. Essentially, those works provided solutions for the temperature change at the position where the laser power absorbed. Here, I applied the same methodology to calculate the temperature oscillation within the film.

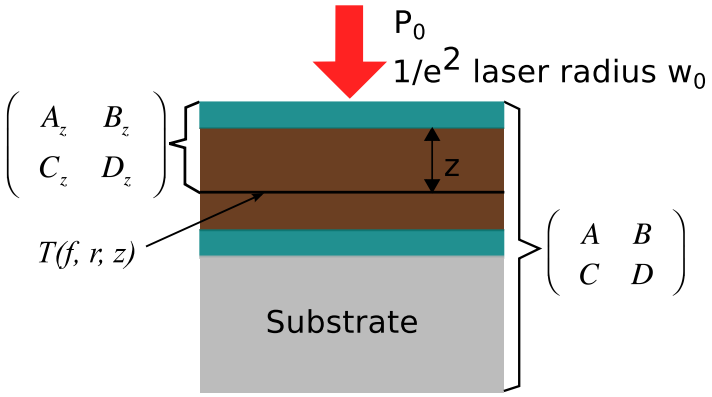

Figure 2.4 A typical configuration of our samples in which a Gaussian-shape laser beam with a power P_0 and $1/e^2$ radius w_0 is absorbed at the top layer (V). The ferroelectric film is sandwiched between two electrodes. In general, two electrode does not need to be the same material and number of layers is not limited. For example, for our samples, the top electrode includes two layers: $SrRuO_3$ and V.

In cylindrical coordinate, we calculate the oscillating temperature $T(f,r,z)$ at radius r and distance z (z is calculated to the interface of the ferroelectric film and the right above layer) (See Figure 2.4). f is the frequency of the heating source, $f = \omega / 2\pi$. We start from relation between heat flux and temperature in frequency domain at the top and bottom of a homogeneous slab with the thermal conductivity Λ, specific heat capacity C and thickness d (See Figure 2.5)

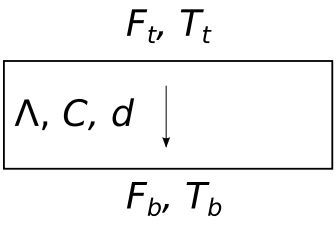

Figure 2.5 1D heat transport in a homogenous slab

Heat is transferred in one direction from the top to bottom is governed by following equation:

$$\begin{pmatrix} T_b \\ F_b \end{pmatrix} = \begin{pmatrix} \cosh(qd) & -\frac{1}{\Lambda q}\sinh(qd) \\ -\Lambda q \sinh(qd) & \cosh(qd) \end{pmatrix} \begin{pmatrix} T_t \\ F_t \end{pmatrix} \tag{2.3}$$

Here $q = \sqrt{i\omega C / \Lambda}$. For a configuration of N layers, we can write the similar relation:

$$\begin{pmatrix} T_b \\ F_b \end{pmatrix} = M_N M_{N-1} \ldots M_1 \begin{pmatrix} T_t \\ F_t \end{pmatrix} = \begin{pmatrix} A & B \\ C & D \end{pmatrix} \begin{pmatrix} T_t \\ F_t \end{pmatrix} \tag{2.4}$$

Here M_j (j = 1, N) is individual matrix of each layer. $\begin{pmatrix} A & B \\ C & D \end{pmatrix}$ is a heat transport matrix of the N layers.

Applying this equation to our problem, we have following equations

$$\begin{pmatrix} T_b \\ F_b \end{pmatrix} = \begin{pmatrix} A & B \\ C & D \end{pmatrix} \begin{pmatrix} T_S \\ F_S \end{pmatrix} \tag{2.5}$$

$$\begin{pmatrix} T_Z \\ F_Z \end{pmatrix} = \begin{pmatrix} A_Z & B_Z \\ C_Z & D_Z \end{pmatrix} \begin{pmatrix} T_S \\ F_S \end{pmatrix} \tag{2.6}$$

Here, T_S, T_b, T_z and F_S, F_b, F_z are temperature and heat flux at the surface of samples, the bottom of samples and position z. $\begin{pmatrix} A & B \\ C & D \end{pmatrix}$ and $\begin{pmatrix} A_Z & B_Z \\ C_Z & D_Z \end{pmatrix}$ are the heat transport matrixes of the entire sample and a part of the sample from distance z to the surface. Applying boundary condition $T_b = 0$, T_z can be calculated as following from Eq. (2.5) and (2.6):

$$T_z = (-A_z \frac{D}{C} + B_z)F_S \tag{2.7}$$

For our problem, we have Gaussian distributed laser power. Hence a convenient method is to use Hankel transform to convert the laser power distribution from real space into k-space. T_z is calculated in k-space using Eq.(2.7) and is converted back to real space.

The laser power can be described as following:

$$F(r) = \frac{2P_0}{\pi w_0^2} \exp\left(-\frac{2r^2}{w_0^2}\right) \tag{2.8}$$

Here P_0 is the amplitude of the absorbed laser power and w_0 is $1/e^2$ radius. The Hankel transform of $F(r)$ is

$$F(k) = \frac{P_0}{2\pi} \exp\left(-\frac{k^2 w_0^2}{8}\right) \tag{2.9}$$

We note that Eq. (2.3) - (2.7) are still valid for our case where the heat is not only transported to the substrate but also spread out laterally. As shown in [51], the only difference is $q = \sqrt{k^2 + i\omega C/\Lambda}$ instead of $q = \sqrt{i\omega C/\Lambda}$ to include the lateral heat distribution. Combining Eq. (2.9) and (2.7) we have:

$$T_z = (-A_z \frac{D}{C} + B_z)F(k) = \frac{P_0}{2\pi}(-A_z \frac{D}{C} + B_z)\exp\left(-\frac{k^2 w_0^2}{8}\right) \tag{2.10}$$

Taking the inverse Hankel transform of T_z gives us the final solution of $T(f, r, z)$ in real space

$$T(f,r,z) = \frac{P_0}{2\pi}\int_0^\infty (-A_z \frac{D}{C} + B_z)kJ_0(kr)\exp(-\frac{k^2 w_0^2}{8})dk \tag{2.11}$$

Here $J_0(kr)$ is the zero-oder Bessel function.

2.5 Temperature calculation

In this section, we will calculate the temperature oscillation *T(f, r, z)* for a typical sample structure of our measurement. The sample has five layers, 150 nm V/ 20 nm $SrRuO_3$ (SRO)/ 150 nm $Pb(ZrTi)O_3$ (PZT)/ 20 nm $SrRuO_3$/ $DyScO_3$ (DSO) substrate. The thermal conductivity and heat capacity of V, SRO, PZT and DSO is shown in Table 2.1. The thermal conductivity of SRO, PZT and DSO is measured using TDTR technique.

Table 2.1 Thermal conductivity and heat capacity of V, SRO, PZT and DSO

	Thermal Conductivity ($W\ m^{-1}\ K^{-1}$)	Heat Capacity ($J\ cm^{-3}\ K^{-1}$)
V	21	3.0[a]
SRO	3.8	3.0[b]
PZT	1.5	2.74[c]
DSO	2.7	2.7

[a]Ref. [79]
[b]Ref. [78]
[c]Ref. [77]

The laser power P_0 is 1mW and the laser spot size is 10 μm. Figure 2.6 plots *T(f, r, z)* at the interface between the top electrode and PZT as a function of radius *r* for different frequencies from 1 Hz to 10 MHz. We can see that the temperature has a Gaussian-like distribution shape with maximum temperature change is ~ 11.8 K at the center and decays with the increasing radius. At low frequencies, heat is spread out further than at high

frequencies. Figure 1.7 shows *T(f, r, z)* as a function of distance z at the center (*r* = 0). The temperature slightly decreases with increasing z.

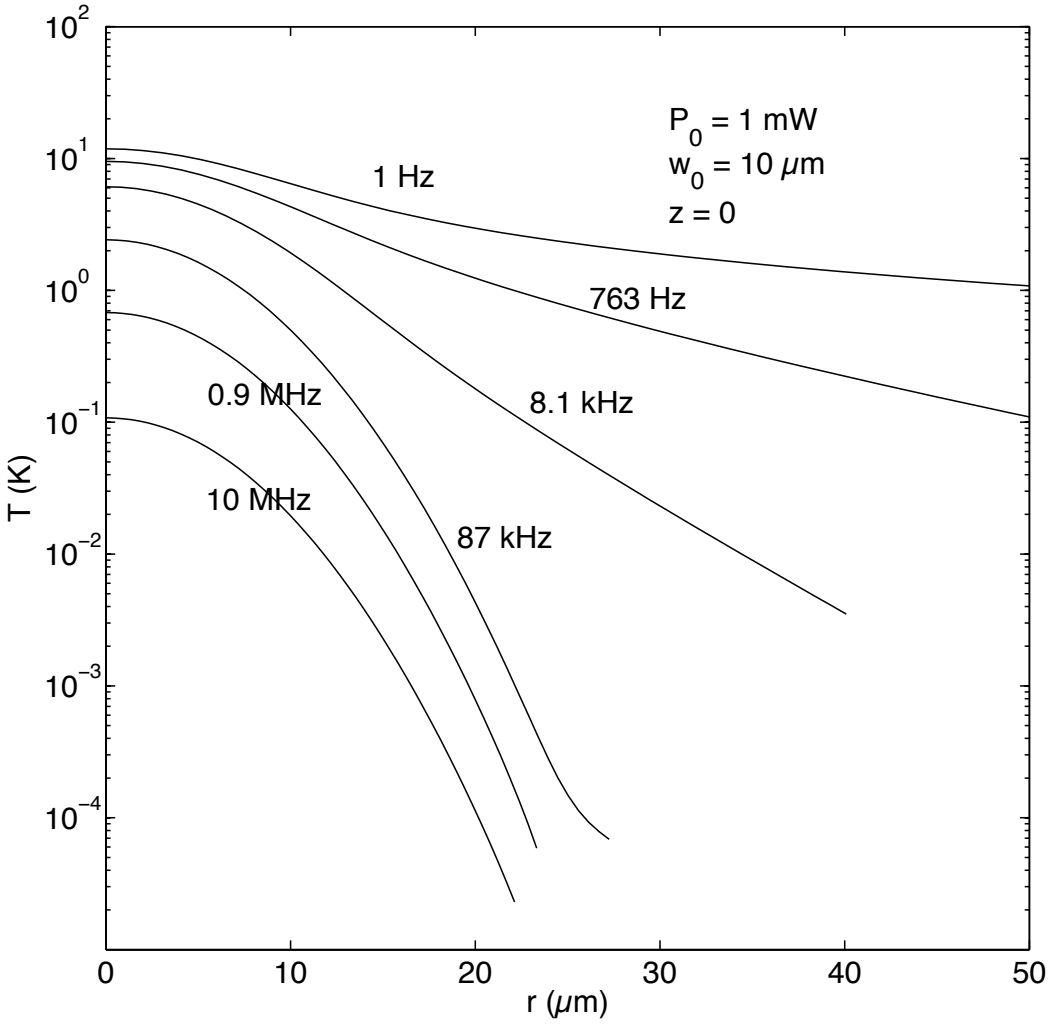

Figure 2.6 Temperature oscillation *T(f, r, z)* at the interface between the film and the top electrode (*z* = 0) as a function of radius *r* at different frequencies from 1 Hz to 10 MHz. The laser power P_0 = 1 mW, the laser spot size w_0 = 10 μm. The sample structure includes 150 nm V/20 nm $SrRuO_3$/150nm $Pb(ZrTi)O_3$/20 nm $SrRuO_3$/DSO substrate.

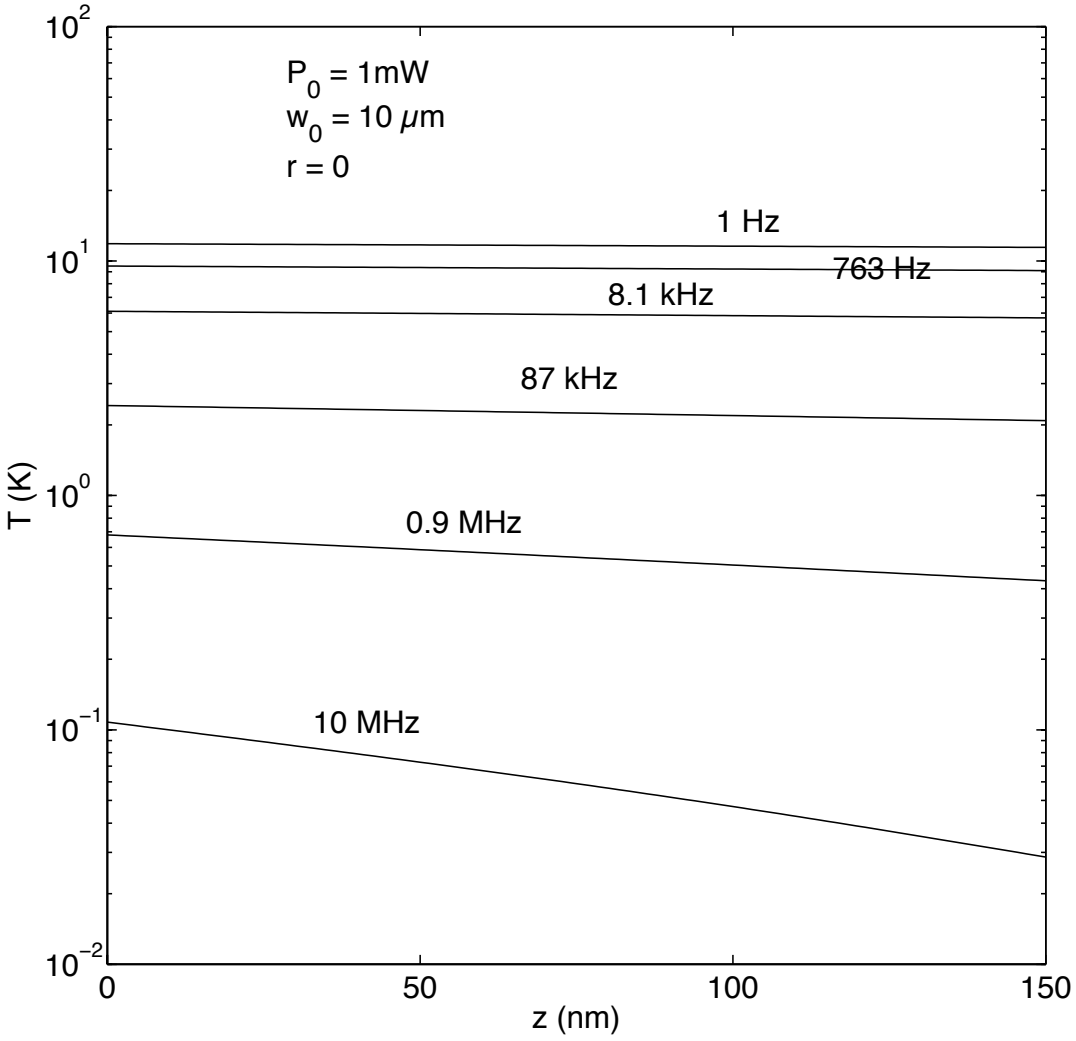

Figure 2.7 Temperature oscillation *T(f, r, z)* as a function of distance z at radius $r = 0$ and different frequencies from 1 Hz to 10 MHz. The laser power P_0 = 1 mW, the laser spot size w_0 = 10 μm. The sample structure: 150 nm V/20 nm $SrRuO_3$/150nm $Pb(ZrTi)O_3$/20 nm $SrRuO_3$/DSO substrate.

For the pyroelectric measurement, the pyroelectric current is collected by the top electrode. This current can be expressed as a sum of the currents created by dipole moments in a volume under the top electrode. Hence, for a circular top electrode, the total pyroelectric current can be written as

$$I(f) = i2\pi f \Pi \pi a^2 \int_0^a \int_0^h \frac{1}{h\pi a^2} T(f,r,z) 2\pi r dr dz \tag{2.12}$$

or

$$I(f) = i2\pi f \Pi \pi a^2 T_{avg}(f) \tag{2.13}$$

Here, a is radius of the top electrode, h is the thickness of films. $T_{avg}(f)$ is defined as the average temperature oscillation:

$$T_{avg}(f) = \frac{1}{h\pi a^2} \int_0^a \int_0^h T(f,r,z) 2\pi r \, dr \, dz \tag{2.14}$$

Note that $T_{avg}(f)$ is a complex with a amplitude to be the amplitude of the temperature oscillation and a phase angle to be the phase lag between the temperature oscillation and the heat flux at the sample surface. Figure 2.8 shows $T_{avg}(f)$ as a function of frequency. At low frequencies f < 100 Hz, the temperature is almost constant and decreases quickly with increasing frequencies. It decreases even faster for f > 1 MHz. The phase angle is shown in Figure 2.9. At low frequencies f < 100 Hz, the phase angle is small which indicates that the heat flux and the temperature are in-phase, while at middle frequencies (1 kHz < f < 100 kHz), the phase difference is about 45°.

To understand how the heat flux is transported to the substrate, we compare the thermal penetration in the substrate, $d = \sqrt{\Lambda / (\pi f C)}$ to the laser

spot size w_0. At low frequencies (f < 1 kHz), $d > w_0$ and heat spreads both laterally and perpendicular to the substrate surface. In the low frequency limit, the temperature change is in-phase with the heat flux and scales with $1/\Lambda_{sub}$, where Λ_{sub} is the thermal conductivity of the substrate. In the high frequency limit (f > 1 MHz), $d < w_0$ and heat transport is approximately one-dimensional, normal to the surface of the sample, and the temperature change is mainly determined by the thermal properties of the films (PZT). At intermediate frequencies (1 kHz < f < 100 kHz), the temperature change is proportional to $1/\sqrt{i\omega\Lambda_{sub}C_{sub}}$ which results in a ≈45° difference between the heat flux and $T_{avg}(f)$.

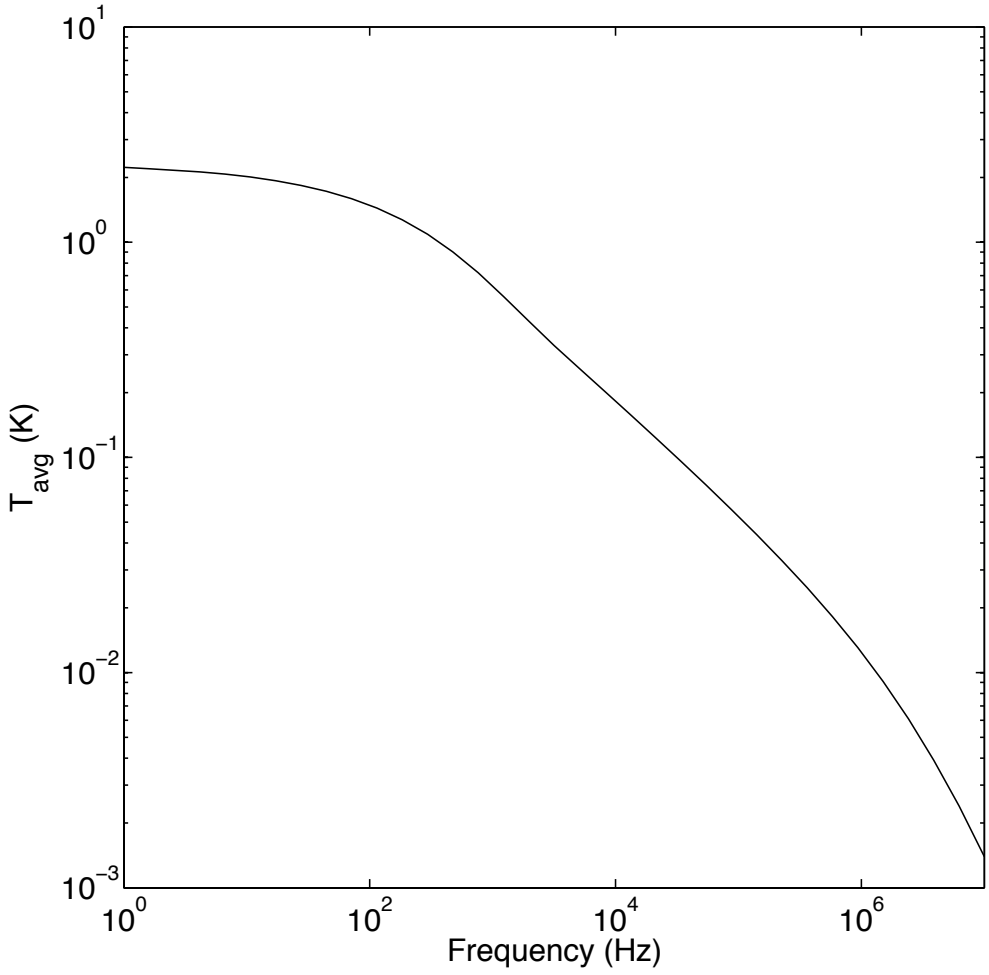

Figure 2.8 The average temperature within the top electrode radius and PZT film thickness as a function of frequency from 1 Hz to 10 MHz. The laser power P_0 = 1 mW, the laser spot size w_0 = 10 μm, the top electrode radius a = 50 μm. The sample structure: 150 nm V/20 nm $SrRuO_3$/150nm $Pb(ZrTi)O_3$/20 nm $SrRuO_3$/DSO substrate.

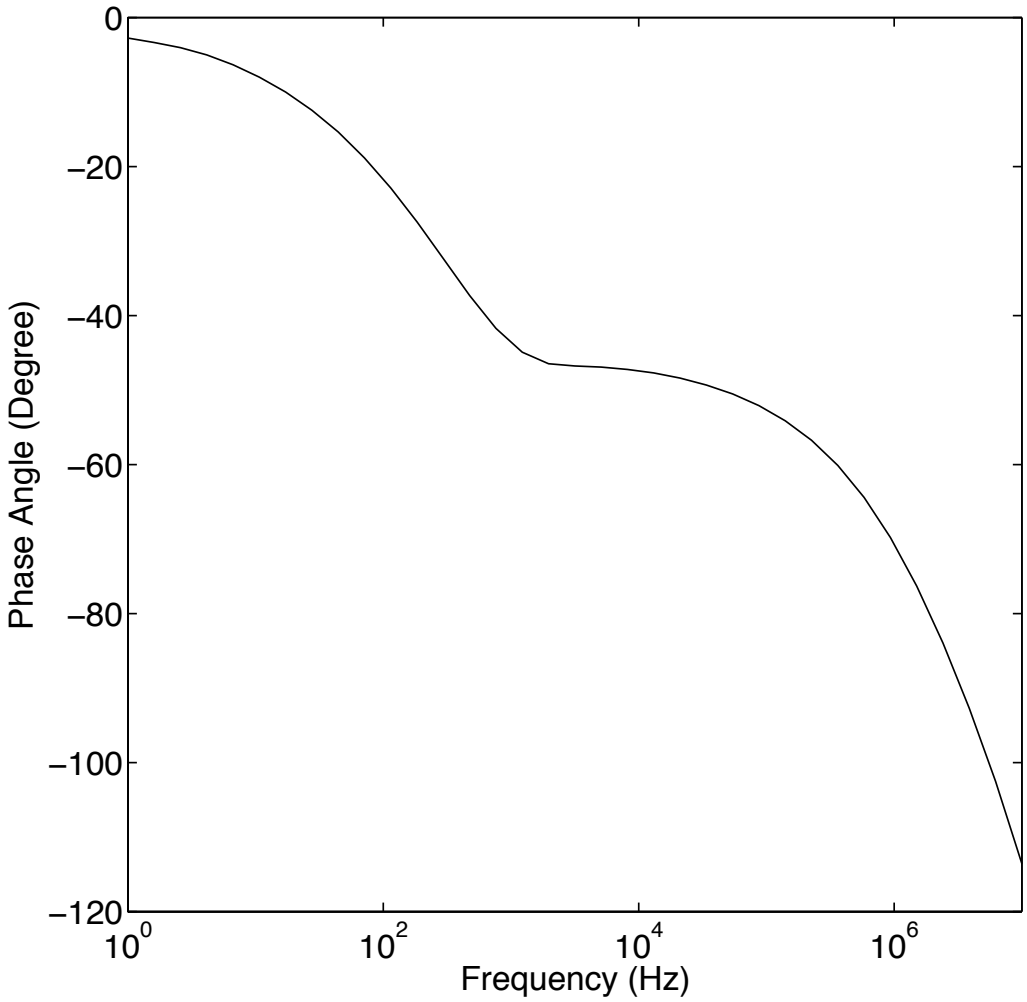

Figure 2.9 The phase angle between $T_{avg}(f)$ and the heat flux at the surface of the sample.

Figure 2.10 shows the temperature $T_{avg}(f)$ as a function of frequencies calculated for different film thicknesses (100 nm, 1 μm and 10 μm). We see that that with increasing of the thickness, the temperature drops faster with increasing frequencies. However, for f < 1 kHz, the temperatures are the same for 3 cases. It can be explained by considering the fact that at low frequencies when the thermal penetration depth d much larger than the film thickness, the temperature is uniform across the film thickness and

determined by the thermal conductivity of the substrate. At higher frequencies, the temperature is significantly decreased with the film thickness so the overall average temperature is smaller. To see how the film thickness affects the pyroelectric measurement, we calculate the pyroelectric current based on Eq. (2.13) (Π is set to 1). The result is shown in Figure 2.11. The pyroelectric current does not increase with the frequency higher than 1 kHz for the thick film (h = 10 μm).

2.6 Experimental data

As described in section 2.2, the laser intensity is modulated by a square-wave. As a result, the temperature oscillation is composed of odd harmonics. To confirm that we measured the pyroelectric current at *f, 2f, 3f, 4f, 5f* while maintaining the same laser power. The lock-in amplifier is set to detect each harmonic. For even harmonics, there is no pyroelectric current. For odd harmonics, the pyroelectric current is measured and plotted in Figure 2.12. Because the pyroelectric current is proportional to frequencies, it is also proportional to harmonic index number (n). However, the laser power amplitude at harmonic n is proportional to $1/n$ (see Fourier transform of a square-wave). Hence, the pyroelectric current at harmonics only depends on the temperature oscillation at *f, 3f, 5f* ... with the same laser power.

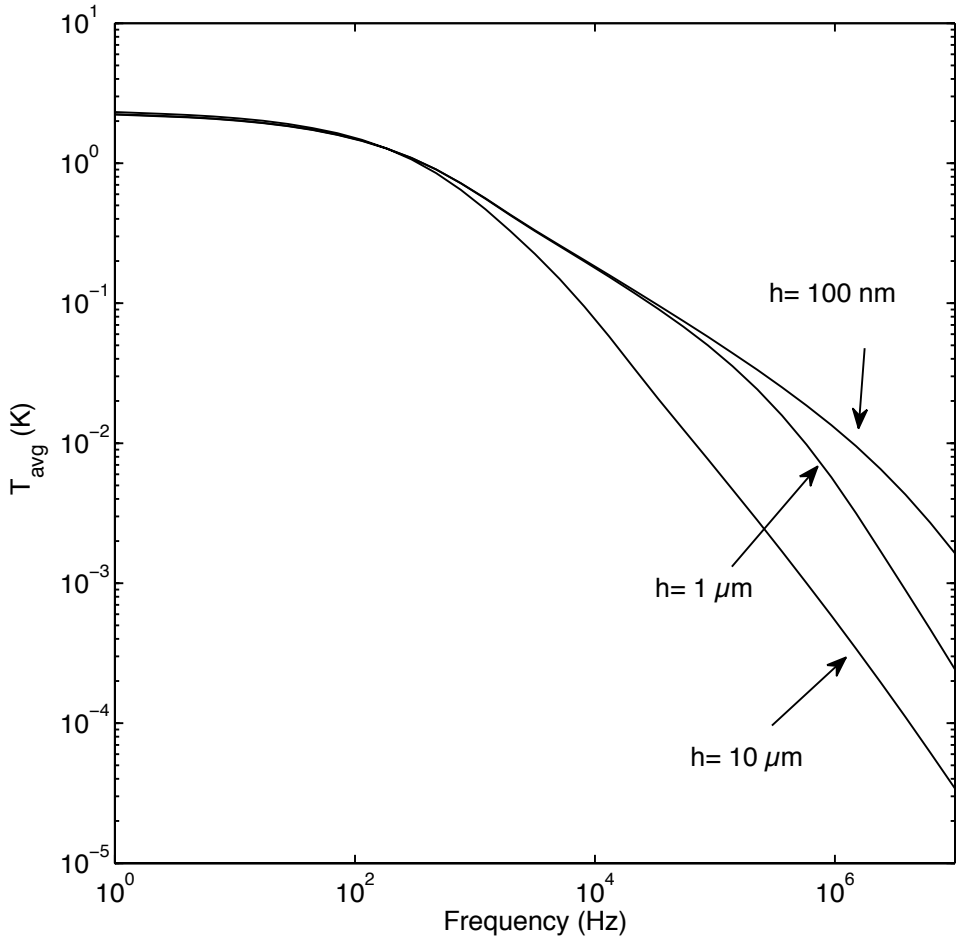

Figure 2.10 The average temperature within the top electrode radius and film thickness as a function of frequencies from 1 Hz to 10 Mhz for PZT film thicknesses of 100 nm, 1 μm and 10 μm. The laser power P_0 = 1 mW, the laser spot size w_0 = 10 μm, the top electrode radius a = 50 μm. The sample structure: 150 nm V/20 nm SRO/ PZT/20 nm SRO/DSO substrate.

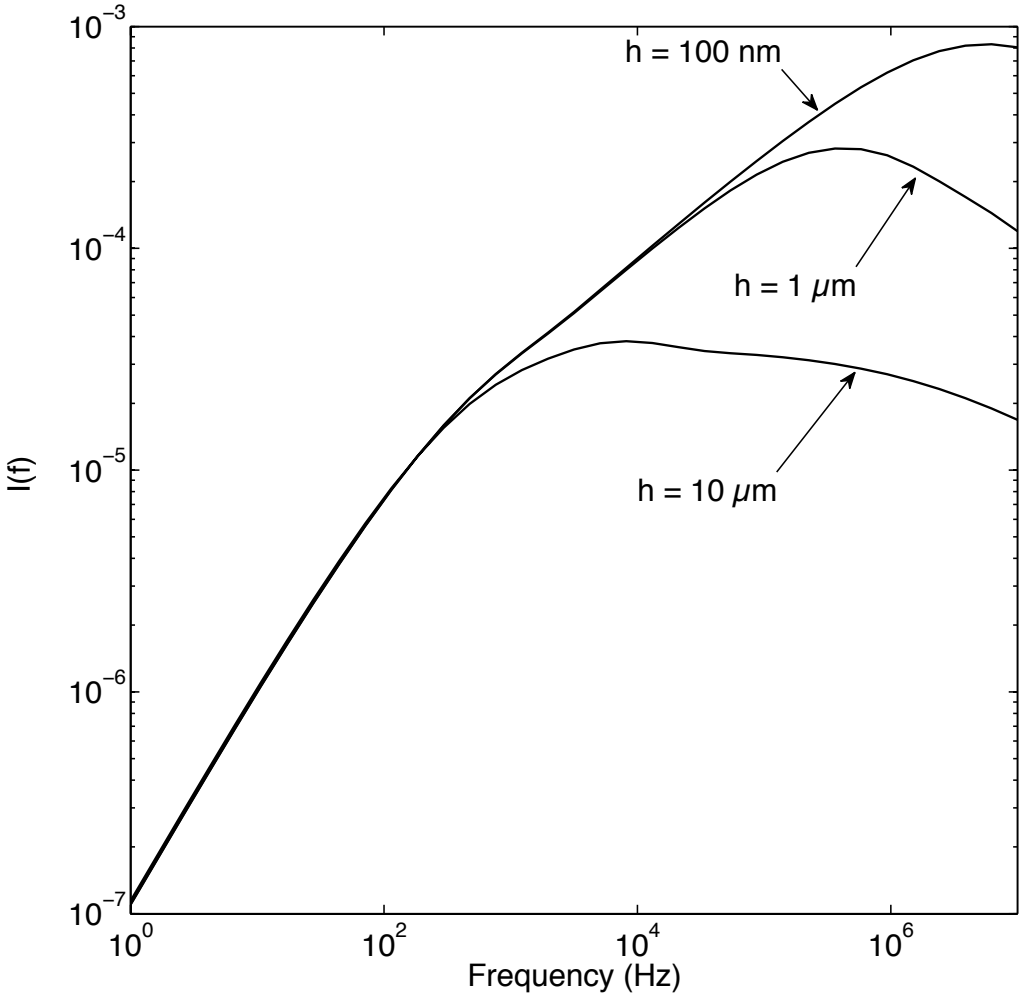

Figure 2.11 The pyroelectric current calculated from Eq. (2.13) as a function of frequency. The pyroelectric coefficient Π is set to be 1. The laser power P_0 = 1 mW, the laser spot size w_0 = 10 μm, the top electrode radius a = 50 μm. The sample structure: 150 nm V/20 nm SRO/ PZT/20 nm SRO/DSO substrate.

In section 2.5, we have presented the phase angle of the temperature oscillation. The measured phase angle of the pyroelectric current is related directly to one of the temperature oscillation but more complicated due to the phase shift introduced by electronics. Figure 2.13 shows a schematic representation of the relative phases between laser power, pyroelectric current and temperature. The pyroelectric current leads the oscillating

temperature by 90° (the pyroelectric current is proportional to derivative of the temperature to time) while the temperature lags behind the heat flux at a phase angle which depends on frequency as described in section 2.5. The phase angle of the pyroelectric current is measured by the lock-in amplifiers. However, at high frequencies the measured phase angle of the pyroelectric current is also affected by the electrical components. Hence, to accurately measure the phase of the pyroelectric current, we replace the sample with a photodiode and measure the current generated by the photodiode under an incident laser power with the same electronics. The phase angle of the photodiode is used to correct for the electrical phase shifts. The corrected phase of the pyroelectric current is the difference between the measured phase of the pyroelectric current and the phase of the photodiode current. The rise-time of the photodiode is ~ 1 ns.

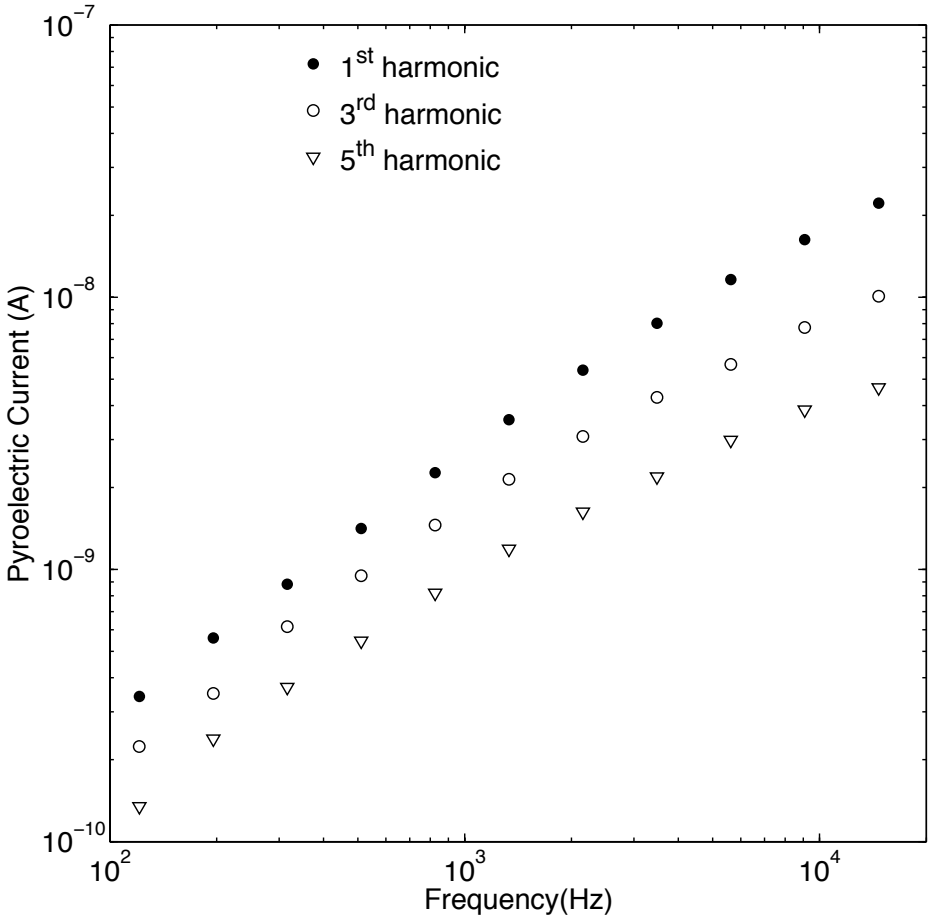

Figure 2.12 The measured pyroelectric current as a function of frequency at 1st, 3rd and 5th harmonics without a low-pass filter. The sample structure is Pt(150nm)/Cr(10nm)/PZT(180nm)/SRO(25nm)/DSO. The laser power is 5 mW, laser spot size is 4.7 μm. Note that the frequencies at 3rd and 5th harmonics are scaled by a factor of 3 and 5 respectively for easy comparison.

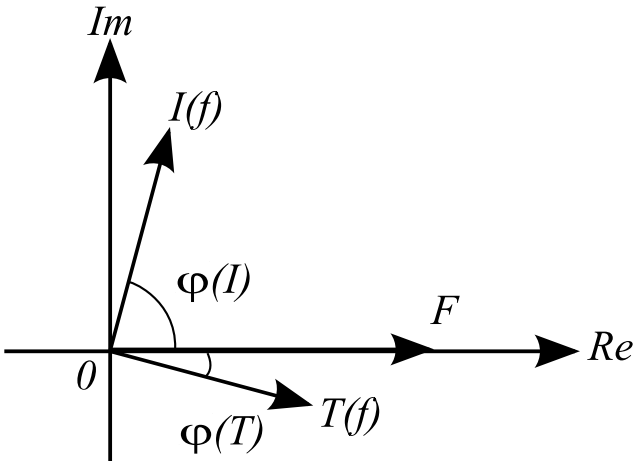

Figure 2.13 Relative phases of the oscillating heat flux, *F*, temperature oscillations created by the heat flux, *T(f)*, and the measured ac current, *I(f)*. When non-pyroelectric currents are negligible in comparison with the pyroelectric current, the measured current leads the temperature change by 90°. The temperature change lags the heat flux by a phase angle, $\varphi(T)$, that depends on frequency. The phase angle of the current, $\varphi(I)$, is measured by the lock-in amplifier.

Ideally, the photodiode current is in the same phase with the heat flux. However, as shown in Figure 2.14, at $f > 200$ kHz, there is a significant phase shift caused by the electronic components. Noted that with a high speed photodiode (rising time ~ 1 ns, approximately a frequency in order of GHz), the capacitance of the photodiode does not introduce a phase shift within the frequency range of our measurement. Hence, the measured phase shift can be used as a correction for the measured phase of the pyroelectric current. However, the capacitance effect of the sample cannot be corrected by this way as discussed below.

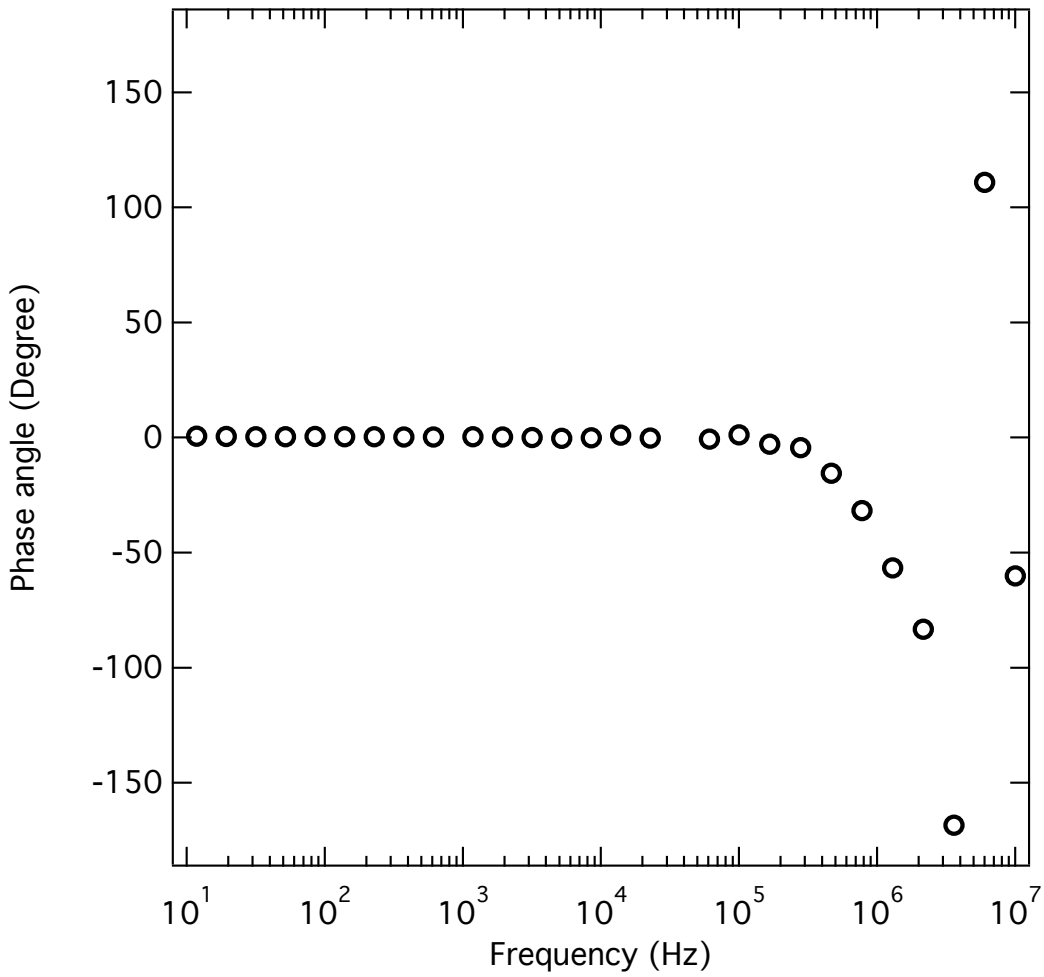

Figure 2.14 The phase shift introduced by electrical components measured by replacing the sample with a photodiode.

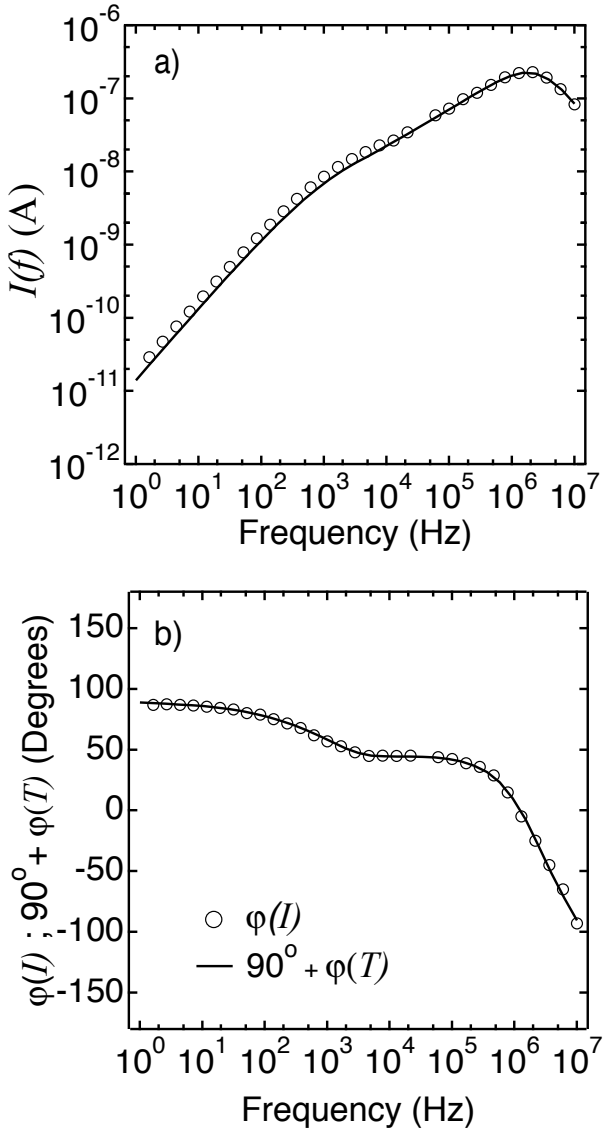

Figure 2.15 Frequency dependence of the amplitude of the pyroelectric current. Measured data are shown as open circles and the solid line is the model calculations for a fixed value of the pyroelectric coefficient. (b) The measured phase angle of the current (open circles), $\varphi(I)$, and the phase angle of the pyroelectric current (solid line) calculated from the phase angle of the temperature, $90^{o}+\varphi(T)$ for the BST/STO sample at zero bias voltage. The good match between the measured and calculated phase supports our assertion that non-pyroelectric currents are negligible in these experiments. The sample structure is V(150 nm)/ SRO (20 nm)/ $BaSrTiO_3$ (150 nm)/ SRO(25nm)/ $SrTiO_3$. The laser power is 6 mW, laser spot size is 10.3 μm.

Figure 2.15 compares the experimental data and model calculation for the amplitude and phase of the pyroelectric current relative to the heat flux.

The pyroelectric coefficient is only parameter to be adjusted to get the best fit to the data. At low frequencies (f < 1 kHz), the temperature change is in-phase with the heat flux and scales with $1/\Lambda_{sub}$, where Λ_{sub} is the thermal conductivity of the substrate. In this low-frequency limit, the amplitude of the pyroelectric current is proportional to ω, the temperature is in-phase with the heat flux, and the phase of the pyroelectric current leads the heat flux by 90 degrees.

At high frequencies, f > 3 MHz, the capacitive reactance of the device and cables are comparable to the R=50 Ω input impedance of the lock-in amplifier used in the pyroelectric measurement. Therefore, the signal is suppressed by a factor $1/(iRC\omega+1)$ where C is effective capacitance of the device and cables. We adjust C to have the best fit at high frequencies and find values of C in range of 300 – 400 pF. For our measurement, capacitances of the devices is on the order of 100 pF and the total BNC cable length is ~2.3 m. Since a typical BNC RG-58 cable has a capacitance of ~100 pF/m, our fitting data of C is on the order of the total equivalent capacitance of the circuit.

At intermediate frequencies (1 kHz < f < 200 kHz), the temperature change is approximately proportional to $1/\sqrt{i\omega\Lambda_{sub}C_{sub}}$ which results in a ≈45° difference between the pyroelectric current and the heat flux. The heat flux and amplitude of the pyroelectric current therefore scales with $1/\sqrt{\omega}$.

2.7 Sensitivity of the pyroelectric measurement

To evaluate the accuracy of measurement due to the propagation of errors from the values of the material properties, we define the sensitivity of the temperature response to each parameter in the thermal model by:

$$S_\beta(f) = \frac{\partial \ln T_{avg}(f)}{\partial \ln \beta} \tag{2.15}$$

Where β is one of the parameters in the thermal model, i.e., thermal conductivity Λ, heat capacity C, or thickness h of each layer. In Figure 2.16, we plot the sensitivity of the temperature calculation to the most important input parameters in the thermal model as a function of frequency. At low frequencies, the calculation is mostly sensitive to Λ_{sub} while at high frequencies the heat capacity and thickness of V and PZT are the most important parameters. At intermediate frequencies, the thermal effusivity of the substrate, $e_{sub} = \sqrt{\Lambda_{sub} C_{sub}}$, is the most important parameter.

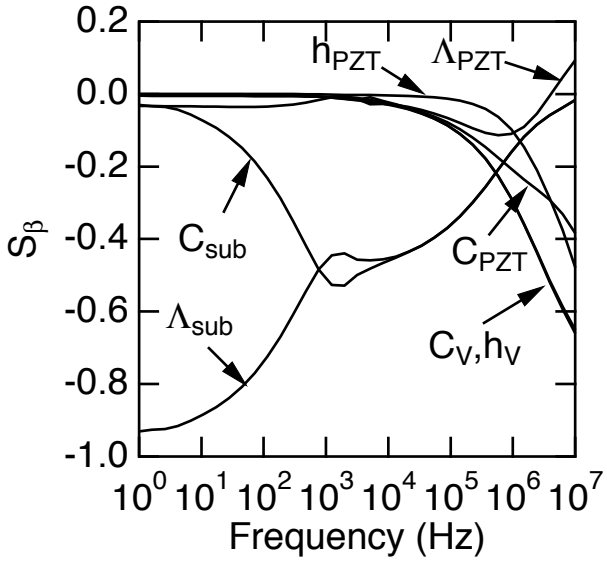

Figure 2.16 Sensitivity of the calculated amplitude of the temperature oscillations, see Eq. (2.15), as a function of selected parameters in the thermal model as a function of heater frequency for a PZT film on a DSO substrate. The radius of the top contact is 50 μm. Sensitivity to the laser power is unity.

CHAPTER 3

SECONDARY PYROELECTRIC EFFECT OF THIN FILMS

Sections of this chapter have been published in "Secondary pyroelectric effect of epitaxial layers revealed by wide-frequency range measurement of the pyroelectric coefficient", T. Tong, J. Karthik, Lane W. Martin, and David G. Cahill, Phys. Rev. B **90**, 094116 (2014)

3.1 Background and theory

A principle application of pyroelectricity is in detectors of infrared radiation. [1] More recently, novel application of pyroelectric materials have employed epitaxial layers and microfabricated devices to enable new functions, e.g., high frequency thermal-to-energy conversion. [15,52] The use of thin epitaxial layers enables engineering of the properties of the ferroelectric layers by varying epitaxial strain and composition.[43-47] The relative roles of intrinsic, extrinsic, and secondary effects are not well established. [5-7] Typically, the change in polarization with increasing temperature is attributed to increasing thermal disorder of electric dipoles. Using molecular dynamics studies, Peng and Cohen recently showed that the origin of pyroelectricity of $LiNbO_3$ is the result of changes in crystal structure with temperature driven by anharmonicity of lattice vibrations. [8]

A measurement of the pyroelectric coefficient dP/dT is the sum of the primary pyroelectric coefficient (what would be measured if the sample could be held at constant strain) and the secondary pyroelectric coefficient which arises from the fact that pyroelectric materials are also piezoelectric and thus thermal expansion (or, more specifically, thermal expansion mismatch between a substrate and thin film) gives rise to a shape change and corresponding stress that can drive an additional change in the polarization with temperature. [9,13,53] Studies of the secondary pyroelectricity of bulk materials have been carried out by many researchers and have been reported to be both negligible[54] and highly significant[55-57] in different systems.

In pyroelectric measurement of a thin film on a thick substrate, the film is free to expand in the thickness direction. However, in the in-plane direction, a film is constrained by its substrate. For the case of a film attached to a substrate and the bulk substrate temperature is fixed, the "planar-clamped" pyroelectric coefficient, Π_1, is described by (see Eq. 8 of Ref. [13])

$$\Pi_1 = \Pi - \frac{2d_{31}\alpha_1}{s_{11} + s_{12}} \tag{3.1}$$

Here Π is the pyroelectric coefficient at constant stress, d_{31} is the piezoeletric coefficient, α_1 is the thermal expansion coefficient of the film, s_{11} and s_{12} are components of the elastic compliance tensor of the film. If the

substrate has the same temperature change as the film, the effective pyroelectric coefficient, Π_2 is (see Eq. 9 of Ref. [13])

$$\Pi_2 = \Pi - \frac{2d_{31}(\alpha_1 - \alpha_{1s})}{s_{11} + s_{12}} \tag{3.2}$$

Here, α_{1s} is the thermal expansion of the substrate. These relationships between the pyroelectric and piezoelectric effect (Eq. (3.1) and Eq. (3.2)) are general and independent of the composition of the films.

We applied a laser-based method to measure the pyroelectric coefficient of epitaxial layers over a wide frequency range. $Ba_{0.6}Sr_{0.4}TiO_3$ (BST) and $PbZr_{0.2}Ti_{0.8}O_3$ (PZT) epitaxial layers are measured under varying static electric fields. The BST and PZT are selected as the subject of our study because deposition conditions and lattice structures are well established. [58,59] At high heating frequencies, the thermal diffusion distance is small compared to the lateral size of the capacitor structure we use to measure the pyroelectric coefficient; the measured pyroelectric coefficient is Π_1 described by Eq. (3.1). At low heating frequencies, the thermal diffusion distance is large compared to the lateral size of the capacitor and the measured pyroelectric coefficient is Π_2 described Eq. (3.2). Thus, by comparing measurements at high and low frequencies, we determine the contribution to the pyroelectric coefficient from in-plane thermal expansion. $\Pi_2 - \Pi_1 = 2d_{31}\alpha_{1s} / (s_{11} + s_{12})$.

3.2 Sample preparation

Capacitor structures are fabricated from heterostructures of 20 nm $SrRuO_3$/150 nm BST or PZT /20 nm $SrRuO_3$ grown on $SrTiO_3$ (STO), $DyScO_3$ (DSO), or $GdScO_3$ (GSO) substrates by pulsed-laser deposition and an MgO hard mask. [59] $SrRuO_3$, $PbZr_{0.2}Ti_{0.8}O_3$ and $Ba_{0.6}Sr_{0.4}TiO_3$ layers were fabricated by pulsed-laser deposition employing a KrF excimer laser (wavelength = 248 nm). Ceramic $SrRuO_3$, $Pb_{1.1}Zr_{0.2}Ti_{0.8}O_3$ and $Ba_{0.6}Sr_{0.4}TiO_3$ targets were used for the growth. The $SrRuO_3$ layer (thickness = 20 nm) was deposited at 630 °C in an oxygen pressure of 100 mTorr with a laser fluence of 1.75 J/cm^2 at a laser repetition rate of 12 Hz. $PbZr_{0.2}Ti_{0.8}O_3$ and $Ba_{0.6}Sr_{0.4}TiO_3$ films (thickness = 150 nm) were grown from PZT and BST targets respectively with the same compositions. After growth, all the samples were cooled in 700 Torr pressure of oxygen to room temperature at 5 K/min. The thickness of the films is determined by deposition time and rate, which is calibrated for each material. The patterned SRO top electrode is fabricated using an MgO hard mask. $SrRuO_3$ (SRO) is used as top and bottom electrodes because of its good metallic conductivity and lattice matching with perovskite substrates. These capacitor structures enable us to efficiently collect the pyroelectric current produced by heating the PZT or BST films with a modulated laser.

The radius of SRO top electrodes is 50 μm or 100 μm. Vanadium (V) films, ≈150 nm thick, are sputtered on top of the SRO top electrodes to

produce an optically opaque layer that absorbs the incident laser power. Any metal which can efficiently absorb the laser power can be used as the top electrode. Here, we choose V because of its compatibility with the fabrication process.

3.3 Measurement of Secondary Pyroelectric Effect

As described in sec 2.6, the pyroelectric coefficient is adjusted to get the best fit between the data with the modeling. However, as shown in Figure 2.1(b), at low frequencies the measured current is higher than predicted by the model when using a pyroelectric coefficient fit to the high frequency data. If instead we adjust the pyroelectric coefficient to fit the experimental data to the model calculation at each frequency, we find $dP/dT \approx$ -230 μC m^{-2} K^{-1} for f < 1 kHz and $dP/dT \approx$ -170 μC m^{-2} K^{-1} for f > 10 kHz, see Figure 3.1(a).

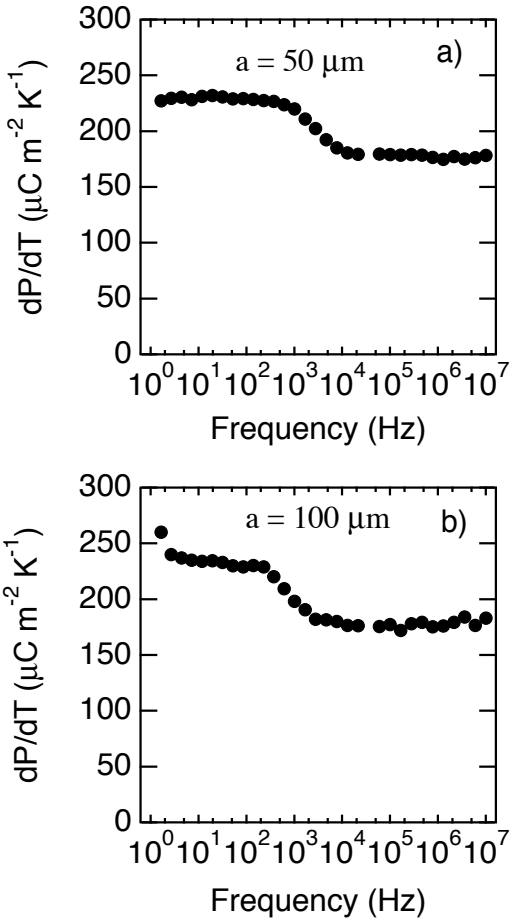

Figure 3.1 Frequency dependence of the pyroelectric coefficient of the $Ba_{0.6}Sr_{0.4}TiO_3$ layer grown on a $SrTiO_3$ substrate. The radius of the top contact of the devices is (a) 50 μm and (b) 100 μm.

The apparent frequency dependence of dP/dT is explained by the secondary contribution to the total pyroelectric current due to the combination of the piezoelectric effect and the thermal expansion of the film and substrate. At low frequency, the thermal penetration depth is large to the radius of the device and the film expands or contracts with the substrate in the plane of the film. As a result, an additional current is generated by the polarization change that arises via the piezoelectric effect. At high frequency, the lateral dimensions of the film do not change because the film is clamped

to the substrate and the near surface layer of the substrate cannot expand laterally. Therefore, at high frequency, the contribution to the secondary pyroelectric from the lateral thermal expansion is zero. The difference between the pyroelectric coefficient at low and high frequencies can be calculated by subtracting Eq. (3.1) and (3.2)

$$\Delta\Pi = \Pi_2 - \Pi_1 = \frac{2d_{31}\alpha_{1s}}{s_{11} + s_{12}} \tag{3.3}$$

Typically, d_{31} is negative which is consistent with our result ($\Delta\Pi < 0$).

The change in the pyroelectric coefficient is centered at a frequency of approximately 3 kHz. This transition frequency is independent of the laser spot size: we repeated the measurement with $1/e^2$ radii of the laser spot sizes between 2.5 and 25 μm and observed no change of the transition frequency. The transition frequency *does* depend on the radius of the top contact. For devices with a top contact that is a factor of two larger (radius of 100 μm), the transition frequency shifts to ≈700 Hz (See Figure 3.1(b)); i.e., the transition frequency scales inversely with the square of the radius of the top contact as expected if the transition frequency is determined by the condition that the thermal penetration depth is comparable to the radius of the top electrode.

Our complete set of data for the pyroelectric coefficient of PZT and BST films on different substrates ($DyScO_3$ – DSO, $GdScO_3$ - GSO) under DC bias voltages at low (20 Hz) and high frequency (20 kHz) are summarized in Figure 3.2. To apply a bias voltage to the films, we put the devices in series with the input impedance of the lock-in amplifier. One terminal of the voltage

source is connected to the top electrode and the other terminal is connected to ground potential. Because of the high resistance of the PZT or BST films (> 1 MΩ), the bias voltage is dropped completely across the films.

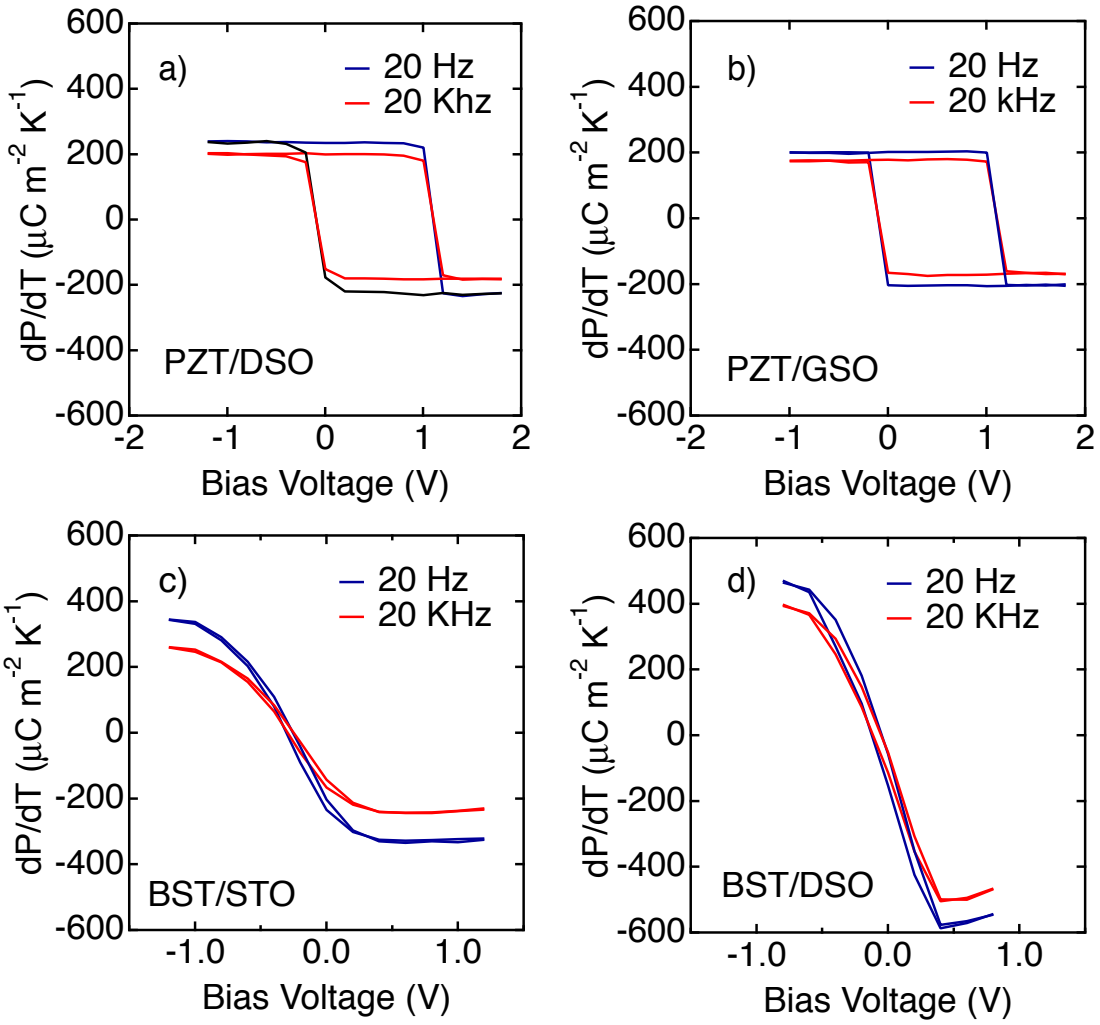

Figure 3.2 Hysteresis of the pyroelectric coefficient of PZT and BST films measured at 20 Hz and 20 kHz at room temperature. The x-axis of each plot is the DC bias voltage that is applied to the capacitors. The time between changes in the bias voltage is ~30 s and the increment between values of the bias voltate is 0.2 V.

We observe hysteresis in the pyroelectric coefficients that resembles the polarization measurements. For the PZT samples (Figure 3.2(a),(b)), the

rectangular-like hysteresis loop is explained by the fact that the films are polarized either up or down with a well-defined coercivity. At the coercive voltages, the pyroelectric coefficient changes sign in response to the change in polarization between these two states.

By contrast, for BST films the pyroelectric coefficient depends on the applied field (Figure 3.2(c),(d)). Since the hysteresis loops are narrow, BST is better described as a relaxor ferroelectric[60-63] [64]which typically has a broad ferroelectric transition[61] and nanoscale polar regions. [62] For an ideal relaxor ferroelectric with randomly oriented nanodomains, the pyroelectric coefficient is zero at zero field and increases with increasing field because of increasing alignment of the nanodomains under an applied field. Our samples are not ideal, however, because the pyroelectric coefficient does not vanish at zero field but is instead shifted by a small amount toward negative bias voltage. dP/dT eventually saturates at high field when all nanodomains are oriented in the field direction.

Figure 3.3 shows the electric field dependence of the secondary pyroelectric coefficient, i.e., the difference between low and high frequency measurements of the total pyroelectric coefficient. Using Eq. (3.3), we calculate the inverse piezoelectric constant d_{31}; d_{31} determined by this approach is of the same order of magnitude with reported values for PZT films. [65,66] We observe that d_{31} shows the same behavior as the pyroelectric coefficients.

The magnitude of the secondary pyroelectric coefficient provides insight about the origin of the pyroelectric effect in these samples. The secondary pyroelectric effect has been theoretically studied for epitaxial layers. [9,13,67] The secondary contribution for PZT was estimated to be approximately 10% of the total response by Karthik *et al.* using Eq. 3.2 and reported value of d_{31}^{f} .[13,67] However, using a thermodynamic model for a polydomain PZT thin films, Karthik *et al.* in a later work predicted a secondary pyroelectric contribution as high as 50% of the total response when taking into account the strain dependence of the polarization and the strain dependence of the volume fraction of domains oriented normal to the film. [9] Furthermore, the thermodynamic model predicts that the secondary effect is only weakly-dependent on the fraction of out-of-plane oriented domains (c-domains). Zook's calculation can be applied to both monodomain and polydomain samples because strain dependence of the polarization and the volume fraction of domain are both reflected in the piezoelectric coefficient d_{31}^{f} . Our result shows that the secondary contribution due to the in-plane thermal expansion of the substrate is less than 15% for the PZT films and 20% for the BST films. In addition, the secondary coefficient is approximately the same for PZT films on DSO and GSO substrates.

We used piezoresponse force microscopy (PFM) to characterize the domain structure of PZT and BST films. The *c*-domains fraction of the PZT film on DSO and GSO is ~ 92% and 75%, respectively, while the BST films

show no domain structure. This results are consistent with previous studies on PZT epitaxial layers and BST films[62]. The thermodynamic model predicts the total pyroelectric coefficient increases with decreasing fraction of the *c*-domain. [67] However, our data shows insignificant differences between the total pyroelectric coefficient for the PZT films on the DSO and GSO substrate. This could arise from domain wall pining resulting in a smaller extrinsic contribution which largely depends on the strain and domain fraction. [9] Moreover, the wide range frequency data shows no frequency dependence of the pyroelectric coefficient up to 10 MHz. This result suggests to us that domain walls are pinned at all frequencies. Recently, Botea *at. al* reported a pyroelectric coefficient (~ 1.9×10^{-3} C m^{-2} K^{-1} about 10 times higher that our measured values) of PZT epitaxial layers grown on $SrTiO_3$ substrates. [68] The 90^o ferroelectric domains and the compressive misfit strain are suggested to be causes for this giant value. More studies are needed to directly study the contribution of the domain wall movement to the overall pyroelectric coefficient.

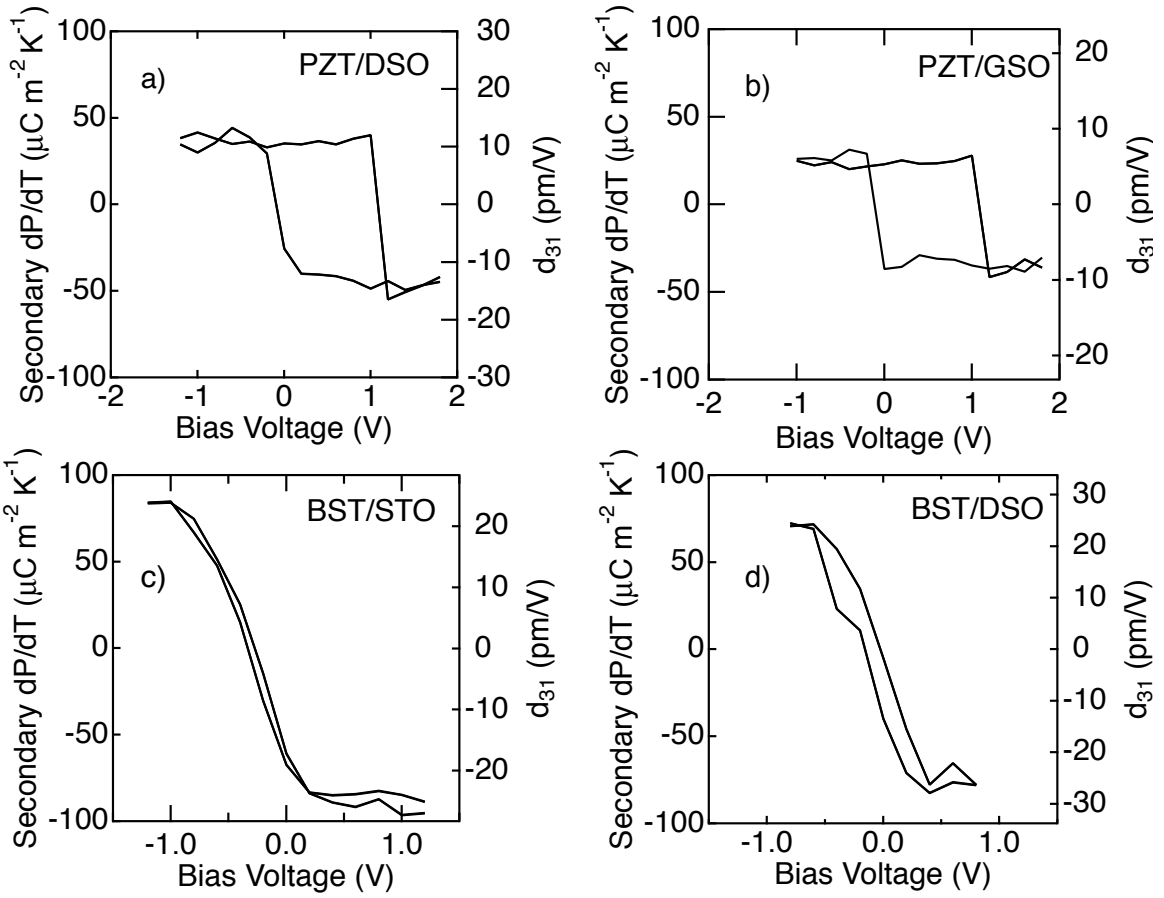

Figure 3.3 Secondary pyroelectric coefficient of PZT and BST films due to the thermal expansion mismatch between the film and substrate as a function of the bias voltage. The right-hand axis of each plot is corresponding converse piezoelectric coefficient d_{31} calculated based on Eq.(3.3).

3.4 Conclusion

In conclusion, we describe a wide frequency-range method to measure the pyroelectric coefficient of epitaxial thin films of pyroelectric materials with high accuracy. A multilayer thermal transport model is developed to solve the temperature oscillation created by the laser power. By analyzing the difference of the pyroelectric coefficients at high and low frequency which

is caused by the clamped effect of the films on the substrates, the secondary contribution of the pyroelectric coefficient is measured. The secondary contribution to the pyroelectric coefficient of the PZT and BST films are measured to be ~ 15% and 20% respectively. The piezoelectric coefficient d_{31} is calculated from the secondary effect. Our method enables studies of the secondary pyroelectric effect of clamped films directly and can be applied to studies of materials with potentially large pyroelectric and piezoelectric effect. For example, we speculate that secondary effect could play a particularly important role in PZT films with composition near the morphotropic phase boundary.

CHAPTER 4

ELECTROCALORIC MEASUREMENT

A part of this chapter has been published in "Reduction of the electrocaloric entropy change of $PbZr_{0.2}Ti_{0.8}O_3$ epitaxial layers due to an elastocaloric effect", T. Tong, J. Karthik, R. V. K. Mangalam, Lane W. Martin, and David G. Cahill, Phys. Rev. B **90**, 094116 (2014)

4.1 Introduction

In this chapter, we describe a laser-based electrocaloric measurement using a laser beam to measure directly the temperature change of thin films generated by the electrocaloric effect. The electrocaloric effect is an inverse effect of the pyroelectricity which describes the reversible temperature change of materials under an applied electric field. We use the same capacitor structure as described in the pyroelectric measurement for the electrocaloric measurement. The electrocaloric effect is introduced by applying a sinusoidal voltage to the devices. The temperature change is measured by using the top electrode as a thermometer and the laser beam will measure change of the reflectivity of the top electrode response to the temperature change.

4.2 Electrocaloric measurement

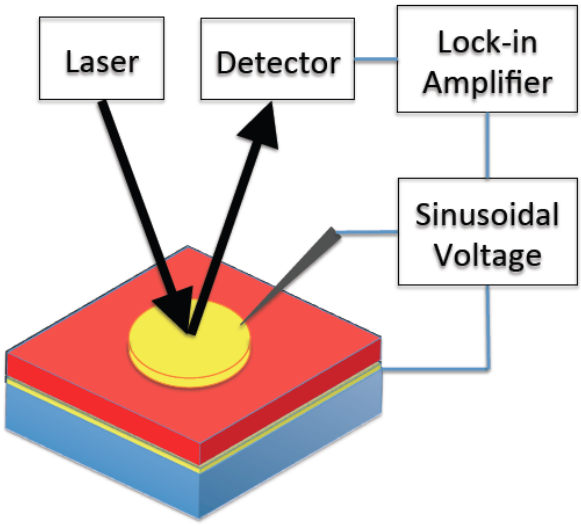

Figure 4.1 Schematic description of the electrocaloric measurement

Figure 4.1 is the schematic diagram of the pyroelectric measurement. A sinusoidal voltage (AC voltage) with an offset (DC voltage) generated by a function generator is connected to the device. The frequency range is from 100 kHz to 10 MHz. The temperature changes ΔT created by the electrocaloric effect is measured through changes of the optical reflectivity of the top electrode by monitoring the intensity change of a laser beam reflected from the top electrode.

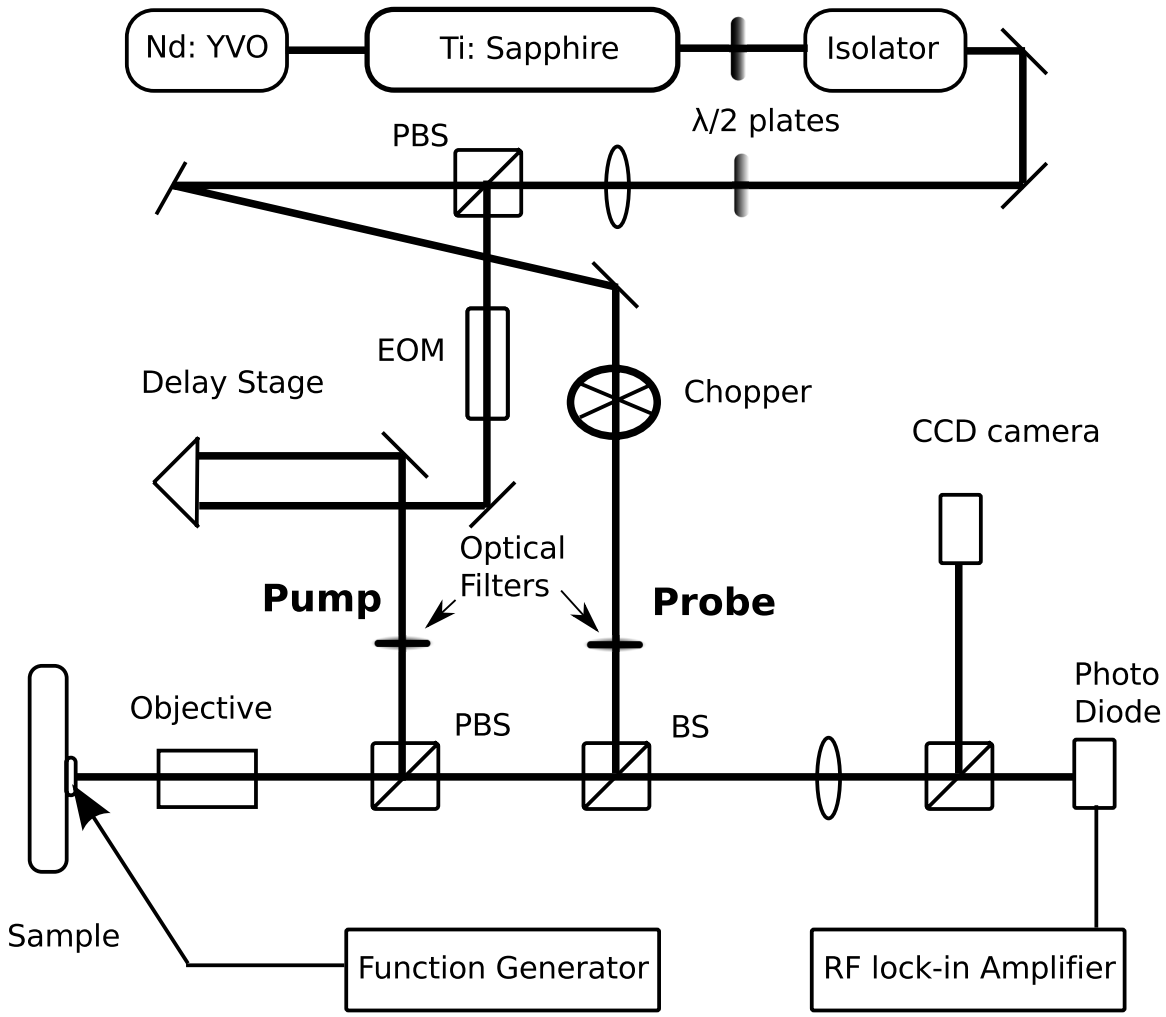

Figure 4.2 Detail of the optical setup of the electrocaloric measurement

We use the probe beam instead of the pump beam as in the pyroelectric measurement (See Figure 4.2). The probe beam is modulated at ~ 200 Hz by a mechanical chopper to suppress noise caused by scattering of the pump beam by surface roughness. The probe beam then is focused on the sample surface using an objective lens. Because the top electrode is much larger than the laser spot size and the temperature is uniform over the surface (described below), the choice of objective lens is not critical and the laser spot size is not

important. The reflected probe beam from the sample is focused on a Si photodiode by a 300 mm objective lens. The signal from the photodiode which has frequency components of $f \pm 200$ Hz is demodulated by the rf lock-in amplifier (SR844) at frequency f and a computer-based locking amplifier at 200 Hz.

The temperature change of the top electrode is determined from: [49]

$$\Delta T(t) = \frac{\sqrt{2}}{G}\frac{V(t)}{V_0}\frac{dT}{dR}R \tag{4.1}$$

Here, R is the reflectivity of the top electrode, dR/dT is the thermoreflectance coefficient of the top electrode, $V(t)$ is the voltage signal measured by the lock-in amplifier, V_0 is the average dc voltage generated by the photodiode, and G is the gain of the pre amplifier. We chose V as the thermal transducer because it has a large value of $(1/R)(dR/dT)$ at the wavelength of 785 nm [69] and more stable at high temperatures. We measure $dR/dT \approx$ 0.79 x 10^{-4} K^{-1} which agrees with the reported data (0.76 x 10^{-4} K^{-1}). [69]

4.3 Heat transport theory

Under an applying sinusoid voltage, the heat power generated within the by the entropy change in adiabatic condition has the form:

$$F = \frac{dQ}{dt} = T\frac{dS}{dt} = T\frac{dS}{dE}\frac{dE}{dt} = T\Sigma E_0 2\pi f e^{-i2\pi ft} \tag{4.2}$$

Here, T is the ambient temperature, E_0 is the amplitude of the oscillating electric field applied to the capacitors, t is time, f is the frequency of the oscillating electric field and Σ or dS/dE is the total electrocaloric coefficient. With the same electric field, the heat is proportional to frequency. However, the higher frequencies produce lower temperature excursion. Detail of the heat calculation enables us to find an optimal working frequency range. The heat is carried bidirectionally to the substrate and the top electrode. In our experiment, we select reasonable low value of E_0 as a trade-off between signal-to-noise and linearity of the response. High frequencies ar e required to achieve high heat flux to produce a significant temperature change. In our electrocaloric measurement, the frequency range is 100 kHz to 10 MHz. The electrocaloric coefficient is determined by the heat flux, which can be calculated with the knowledge of the measured temperature change at the top electrode and the thermal properties of each layer. Since the electrode radius (50 μm) is much larger than the thermal penetration depth, $d = \sqrt{\Lambda/(\pi f C)} \simeq 0.2$ - 2 μm, heat transport is approximately one-dimensional. The generated heat flux is uniform within the ferroelectric layer. A bidirectional heat flow model[51] is used to take into account the heat flux distribution over the ferroelectric layers.

To quantify the relationship between the temperature at the sample surface and the heat generated uniformly within the ferroelectric films; we solve the 1D problem for a heat flux generated in a thin slab of ferroelectric

film, $dF = Fdz$ (See Figure 4.3) and then sum the contributions from all slabs. Here F is the heat created per volume unit. For each slab, the heat dF diffuses to the substrate and the top electrode. We define multiple layers from the slab to the substrate to be system and from the slab to the top electrode to be system 2. Each system is described by a transport matrix, which is multiplication of matrices of individual layers (See section 2.4). We write the relation between the temperature and heat flux at the sample surface, bottom and the position z:

$$\begin{pmatrix} T_t \\ F_t \end{pmatrix} = \begin{pmatrix} A_2 & B_2 \\ C_2 & D_2 \end{pmatrix} \begin{pmatrix} T_z \\ F_{z2} \end{pmatrix} \tag{4.3}$$

and

$$\begin{pmatrix} T_b \\ F_b \end{pmatrix} = \begin{pmatrix} A_1 & B_1 \\ C_1 & D_1 \end{pmatrix} \begin{pmatrix} T_z \\ F_{z1} \end{pmatrix} \tag{4.4}$$

Applying boundary conditions: $F_t = 0$ (no heat escaped from the surface to surrounding); $F_b = 0$; total heat flux at z: $F_0 = F_{z1} + F_{z2}$. We can write:

$$\begin{aligned} C_2 T_z + D_2 F_{z2} &= 0 \\ C_1 T_z + D_1 F_{z1} &= 0 \end{aligned} \tag{4.5}$$

After some algebra, we have:

$$T_z = \left(\frac{-D_1 D_2}{C_2 D_1 + C_1 D_2} \right) F_0 \tag{4.6}$$

Hence the temperature at the sample surface is:

$$T_t = A_2 T_z + B_2 F_{z2} = A_2 T_z + B_2 \left(-\frac{C_2}{D_2} \right) T_z = \left(\frac{A_2 D_2 - B_2 C_2}{D_2} \right) T_z = \left(\frac{B_2 C_2 - A_2 D_2}{C_2 D_1 + C_1 D_2} D_1 \right) F_0 \tag{4.7}$$

Replacing F_0 by the heat flux of a slab dF; T_t by $d(\Delta T)$, the total temperature change at the sample surface, ΔT_V related to heat flux F by:

$$\Delta T_V = \int_0^h \left(\frac{B_2 C_2 - A_2 D_2}{C_2 D_1 + C_1 D_2} D_1 \right) dF = F \int_0^h \left(\frac{B_2 C_2 - A_2 D_2}{C_2 D_1 + C_1 D_2} D_1 \right) dz \quad (4.8)$$

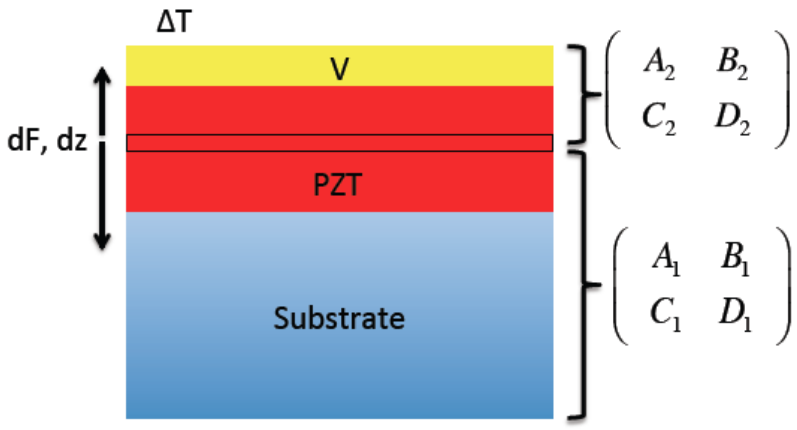

Figure 4.3 Thermal model for bidirectional heat conduction into the V film and substrate. The film is divided into thin slabs with the thickness of dz. The heat flux of each slab, dF, creates a temperature change $d(\Delta T)$ at the sample surface. The total temperature ΔT is sum of the temperature changes $d(\Delta T)$. $\begin{pmatrix} A_1 & B_1 \\ C_1 & D_1 \end{pmatrix}$ is the heat transport matrix for a part of the sample at a distance z from the bottom layer and $\begin{pmatrix} A_2 & B_2 \\ C_2 & D_2 \end{pmatrix}$ is the heat transport matrix for a part of the sample at a distance z from the top layer.

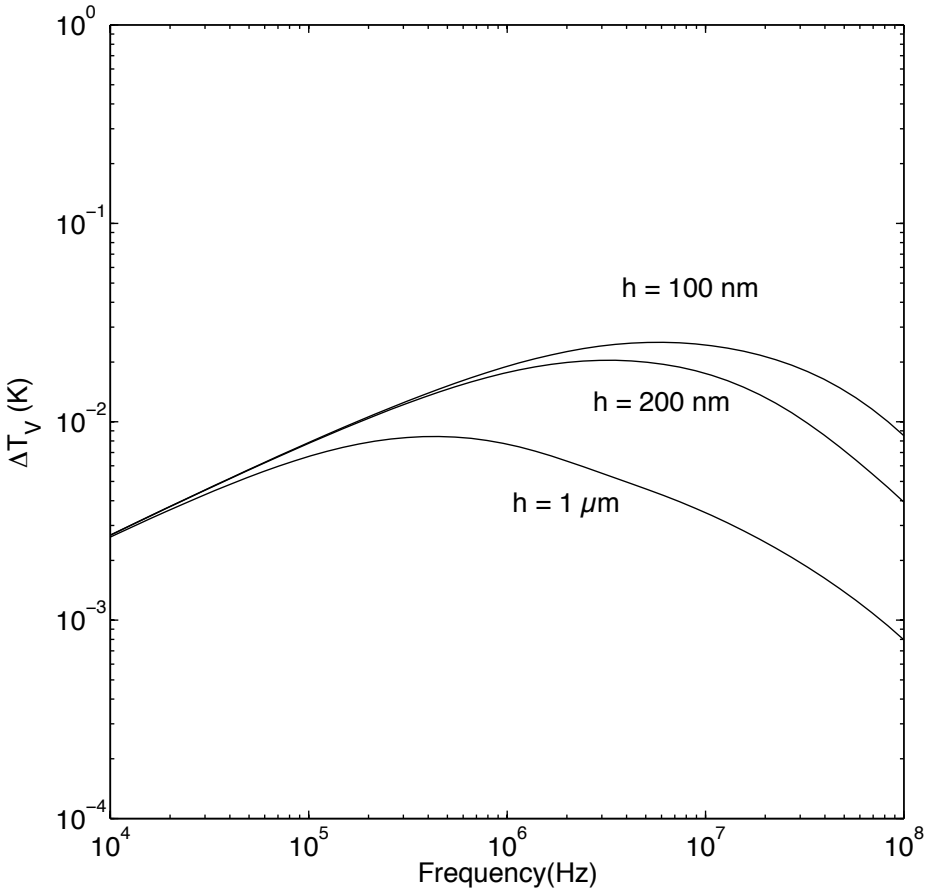

Figure 4.4 Temperature change at the top electrode as a function of frequency for different film thicknesses (h = 100 nm, 200 nm and 1 μm). The electrocaloric coefficient $\Sigma = 100$ μC m^{-2} K^{-1}; Amplitude of applying voltage E_0 = 1 V; T = 300 K. Sample structure: V (150 nm)/ SRO (20 nm)/ PZT (h)/ SRO (20 nm)/ DSO.

Figure 4.4 shows example calculations of the temperature change at the top electrode based on Eq. (4.8) and (4.2). The temperature change increases with the increasing frequencies and reaches to maximum at 3 MHz – 10 MHz for the film thickness of 100 nm. The peak of the temperature change is shifted to lower frequencies when the film thickness increases. Furthermore, the maximum temperature change also decreases. The

temperature changes are converged at low frequencies. This can be explained by considering the fact that at low frequency limit when the thermal penetration depth is larger than the film thicknesses, the film thickness has no effect on the temperature change at the sample surface. Hence, the temperature change only depends on the total heat generated within the film. Because the total heat is the same with the same applying voltage, (the heat density is smaller but the film volume is higher), the temperature change is unchanged.

4.4 Sensitivity of the electrocaloric measurement

To evalulate the sensitivity of the electrocaloric measurement, we define the sensitivity of the temperature change response to each parameter in the thermal model by:

$$S_{\beta}(f) = \frac{\partial \ln T_V(f)}{\partial \ln \beta} \tag{4.9}$$

Where β is one of the parameters in the thermal model, i.e., thermal conductivity Λ, heat capacity C, or thickness h of each layer. In Figure 4.5 we plot the sensitivity of the temperature calculation to the most important input parameters in the thermal model as a function of frequency. At low frequencies, the calculation is mostly sensitive to Λ_{sub} and C_{sub} while at high frequencies the heat capacity and thickness of V and PZT are the most important parameters.

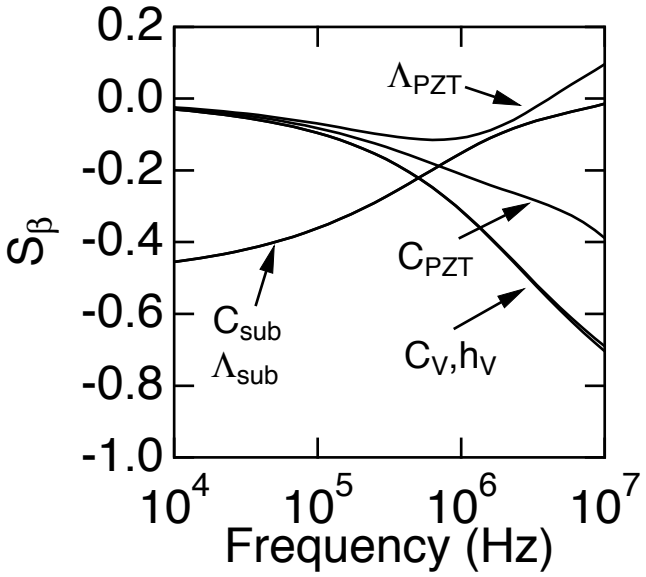

Figure 4.5 Sensitivity of the calculated temperature change at the top electrode, see Eq(4.9), as a function of selected parameters in the thermal model as a function of frequency for a PZT film on a DSO substrate.

4.5 Verifying the thermoreflectance coefficient measurement

We confirm the accuracy of the measurement of dR/dT by using a 2-omega method (See Figure 4.6). A metal pattern (Al) is produced by a photolithography through a mask on a SiO_2 substrate. A sinusoidal voltage is applied on the metal line to produce an oscillating temperature at a frequency of 2 times of a source frequency. A laser beam is used to probe the temperature change through the change of the thermal reflectivity of the metal line. By using a thermal model, [70] the temperature change of the metal line is calculated and then dR/dT is extracted through Eq. (4.1).

dR/dT measured by the 2-omega method ($dR/dT \approx 0.81 \times 10^{-4}$ K^{-1}) and the TDTR method are in good agreement with each other.

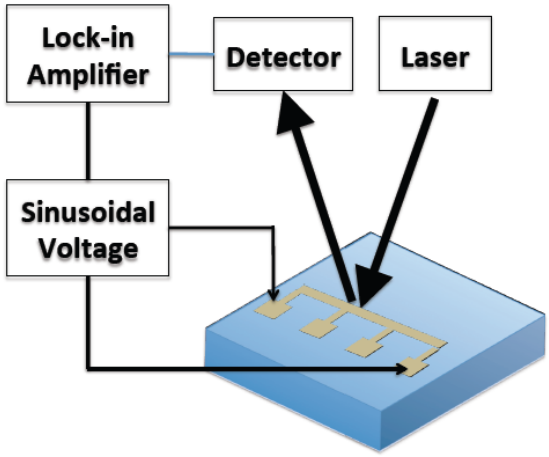

Figure 4.6 A schematic of the 2-omega method to measure the thermoreflectance coefficient.

CHAPTER 5

ELECTROCALORIC EFFECT OF THIN FILMS

Sections of this chapter have been published in "Reduction of the electrocaloric entropy change of $PbZr_{0.2}Ti_{0.8}O_3$ epitaxial layers due to an elastocaloric effect", T. Tong, J. Karthik, R. V. K. Mangalam, Lane W. Martin, and David G. Cahill, Phys. Rev. B **90**, 094116 (2014)

5.1 Background and theory

Heat engines convert thermal energy to work and pump heat against a temperature gradient. While most practical heat engines are based on the large entropy difference between the vapor and condensed phases of a working fluid, there is increasing interest in using the physics of materials to build efficient solid-state heat engines. For example, thermoelectric generators use the entropy of charge carriers in semiconductors to convert a steady flow of heat to electrical power. Caloric effects in which the entropy of a material changes in response to an external field have potential application in energy scavenging and solid-state refrigeration. [25,26]

Our work is focused on the electrocaloric effect where the entropy of a material is modulated by an electric field. While the inverse of the

electrocaloric effect, the pyroelectric effect, has been widely studied, the electrocaloric effect is less studied due, in part, to the significant experimental challenge of direct measurements of the temperature change.

The total pyroelectric coefficient can be described as the sum of primary and secondary contributions: [10]

$$\Pi = \frac{dP}{dT} = \Pi' + \Pi'' \tag{5.1}$$

Where P is the electrical polarization, and T is temperature. The primary pyroelectric coefficient $\Pi' = \left(\frac{dP}{dT}\right)_{E,\varepsilon}$ describes the change of polarization with respect to temperature at constant strain (ε) and electric field (E). The secondary pyroelectric coefficient, $\Pi'' = \sum_i d^*_{ijk} c_{jklm} \alpha_{lm}$, is the contribution to the change in polarization from thermal expansion combined with the piezoelectric effect. [10] Here, d^*_{ijk} is the direct piezoelectric coefficient; the notation of the superscript asterisk is typically used to differentiate the direct piezoelectric coefficient from the converse piezoelectric coefficient d_{ijk}. c_{jklm} is the fourth-rank elastic constant tensor, and α_{lm} is the second-rank thermal expansion coefficient tensor. For materials with tetragonal symmetry and replacing the fourth-rank tensor notation with conventional two-index notation, Π'' is [3][10]

$$\Pi'' = 2\alpha_1(d^*_{31}c_{11} + d^*_{31}c_{12} + d^*_{33}c_{13}) + \alpha_3(2d^*_{31}c_{13} + d^*_{33}c_{33}) \tag{5.2}$$

As discussed below, in our experiment, the lateral expansion of the PZT layers is zero because the films are confined by the substrate. Hence, the secondary coefficient reduces to $\Pi'' = d_{33}^{*} c_{33} \alpha_3$. Generally, d_{33}^{*} is positive for PZT films[71] hence $\Pi'' > 0$ while $\Pi' < 0$.

Similarly, we separate the total electrocaloric coefficient into the primary and secondary contributions:

$$\Sigma = \frac{dS}{dE} = \Sigma' + \Sigma'' \tag{5.3}$$

where S is entropy and E is the electric field. The primary electrocaloric coefficient $\Sigma' = \left(\frac{dS}{dE} \right)_{T,\varepsilon}$ describes the change of entropy in response to an applied field at constant strain and temperature. The secondary coefficient, $\Sigma'' = \sum_i C d_{ijk} \gamma_{jk}$, results from changes in the vibrational entropy created by the elastic strain due to the piezoelectric effect. [72] Here, γ_{jk} is the generalized Grüneisen parameter tensor which relates changes in stress to changes in internal energy at constant strain for an anisotropic material, [49] d_{ijk} is the converse piezoelectric coefficient, and C is the volumetric heat capacity at constant volume. For tetragonal symmetry

$$\Sigma'' = C(2 d_{31} \gamma_1 + d_{33} \gamma_3) \tag{5.4}$$

Here $\gamma_1 = \frac{1}{C}(c_{11}\alpha_1 + c_{12}\alpha_1 + c_{13}\alpha_3)$ and $\gamma_3 = \frac{1}{C}(2c_{13}\alpha_1 + c_{33}\alpha_3)$ [6]and Σ'' reduces to $\Sigma'' = d_{33}\gamma_3 C$ for a clamped film. Σ'' has the opposite sign as Σ' ($\Sigma' < 0;\ \Sigma'' > 0$): with increasing electric fields the PZT layers expand and, due to

anharmonicity, the vibrational frequencies of the lattice are reduced. This softening of the lattice vibrations increases the vibrational entropy. [72] On the other hand, an increasing field lowers the entropy of the system associated with the polarization by the primary electrocaloric effect. These opposing mechanisms reduce the overall entropy change that is achievable.

The thermodynamic Maxwell relation shows that the pyroelectric and electrocaloric coefficients are equal at constant strain or stress condition. (see Eq. 35 Ref. [73]):

$$\begin{aligned} \Pi' &= \Sigma' \\ \Pi\big|_{\sigma} &= \Sigma\big|_{\sigma} \end{aligned} \tag{5.5}$$

Hence the secondary pyroelectric and electrocaloric coefficient are equal, $\Pi'' = \Sigma''$ under constant stress condition. The derivations of Π'' and Σ'' for tetragonal symmetry case (Eq. (5.2) and (5.4)) agree with this result because the direct and converse piezoelectric coefficients are equal (Eq. 2 Ref [74]).This relation is the basis of the so-called "indirect" method to study the electrocaloric effect both theoretically and experimentally. [34,36,37,39,41,42]

However, for clamped films, the difference between the total electrocaloric coefficient and the total pyroelectric coefficient is $\Sigma - \Pi = \Sigma'' - \Pi'' = d_{33}\gamma_3 C - d_{33}^{*} c_{33}\alpha_3$. Both the direct and converse piezoelectric coefficients (the so-called effective coefficients) are both reduced by a factor of ~2 compared to an unclamped film. [71] The calculation by Lefki *et al.* shows that the effective direct piezoelectric coefficient is larger than the effective

converse one (see Eq. 2 and 3 Ref. [71]) because of a contribution from the mechanical deformation of the substrate. However, in our measurement the substrate is fixed so $d_{33}^{*} = d_{33}$. Therefore, we simplify the equation for $\Sigma - \Pi$ as

$$\Sigma - \Pi = d_{33}(\gamma_3 C - c_{33}\alpha_3) = 2d_{33}c_{13}\alpha_1 \tag{5.6}$$

Thus, a measurement of the difference between the total coefficients captures the first term in the following expression for the secondary electrocaloric coefficient, $\Sigma'' = d_{33}\alpha_1(2c_{13} + c_{33})$ where we have set $\alpha_1 = \alpha_3$. For PZT, c_{13} = 68 GPa, c_{33} = 113 GPa[75], and α_1 = 5.4 x 10^{-6} K^{-1}. [67] Since $2c_{13} \approx c_{33}$, $\Sigma'' \approx 2(\Sigma - \Pi)$.

In this study, we use two novel laser-based methods to independently measure the total pyroelectric (Π) and electrocaloric coefficients (Σ) of PZT epitaxial layers. Because our measurements are performed with high-frequency thermal fields, the mechanical conditions of our electrocaloric measurements are the same as for the pyroelectric measurements; *i.e.*, the in-plane strain is zero. Combining these methods allows us to quantify the secondary contribution to the total electrocaloric coefficient. We find that the secondary electrocaloric effect significantly reduces the total electrocaloric response and should be considered in evaluating the performance of electrocaloric materials and heat engines.

5.2 Sample preparation

Capacitor structures are fabricated from heterostructures of 20 nm $SrRuO_3$/150 nm PZT/20 nm $SrRuO_3$ grown on $DyScO_3$ (DSO) (110) and $GdScO_3$ (GSO) (110) substrates by pulsed-laser deposition. Compositionally homogeneous single-layer $PbZr_{0.2}Ti_{0.8}O_3$ films (thickness = 150 nm) were grown from PZT targets with the same composition at 630 °C in an oxygen pressure of 200 mTorr at a laser fluence of 2 J/cm^2 and a laser repetition rate of 3 Hz. Compositionally-graded heterostructures (thickness=150 nm) were synthesized from $Pb_{1.1}Zr_{0.2}Ti_{0.8}O_3$ and $Pb_{1.1}Zr_{0.8}Ti_{0.2}O_3$ targets at 600˚C at a laser fluence of 1.9 J/cm^2 in 200 mTorr of oxygen and a laser repetition rate of 3 Hz. Compositionally graded heterostructures were synthesized by continuously varying the composition from $PbZr_{0.2}Ti_{0.8}O_3$ to $PbZr_{0.8}Ti_{0.2}O_3$ using a programmable target rotator (Neocera, LLC) that was synced with the excimer laser. We use PZT layers as the subject of our study because deposition conditions and lattice structures are well established. [58] These capacitor structures enable us to apply electric fields in the electrocaloric measurement and collect the pyroelectric current in the pyroelectric measurement. Circular SRO top electrodes with radius of 50 μm or 100 μm are patterned by photolithography utilizing an MgO hard-mask process. [59] We prepared and measured three samples: two compositionally homogenous $PbZr_{0.2}Ti_{0.8}O_3$ (PZT20:80) epitaxial layers on DSO and GSO substrates, and one compositionally graded heterostructure which smoothly transitions from

$PbZr_{0.2}Ti_{0.8}O_3$ to $PbZr_{0.8}Ti_{0.2}O_3$ from the GSO substrate to the surface (Graded-PZT). [76] Vanadium (V) films, ≈150 nm thick, are sputtered on top of the SRO top electrodes to produce an optical transducer that absorbs the incident laser power and provides a strongly temperature dependent optical reflectivity, *i.e.*, a high thermoreflectance, for measurements of the electrocaloric coefficient. [69]

Thermal conductivities of each layer and the thermoreflectance coefficients of the V film are measured by time domain thermoreflectance (TDTR). [49] The thickness of the V film is measured by picosecond acoustics. [50] These properties are used as input parameters of thermal transport models for the pyroelectric and electrocaloric measurement (See Table 4.1).

Table 5.1 Thermophysical properties of PZT, DSO, GSO, SRO and V measured by TDTR and from literatures used in the thermal transport calculation.

	25 (°C)	75 (°C)	150 (°C)	220 (°C)
C_{PZT} (J m^{-3} K^{-1})[a]	$2.7x10^6$	$2.9x10^6$	$3.1x10^6$	$3.2x10^6$
Λ_{PZT} (W m^{-1} K^{-1})	1.5	1.5	1.5	1.5
C_{SRO} (J m^{-3} K^{-1})[b]	$3.00\ x10^6$	$3.1\ x10^6$	$3.17\ x10^6$	$3.24\ x10^6$
Λ_{SRO} (W m^{-1} K^{-1})	3.9	3.9	3.9	3.9
C_{DSO}*Λ_{DSO} (J W m^{-4} K^{-2})	$7.3\ x10^6$	$7.3\ x10^6$	$7.3\ x10^6$	$7.3\ x10^6$
C_{GSO}*Λ_{GSO} (J W m^{-4} K^{-2})	$7.3\ x10^6$	$7.3\ x10^6$	$7.3\ x10^6$	$7.3\ x10^6$
C_V (J m^{-3} K^{-1})[c]	$2.95x10^6$	$2.97x10^6$	$3.0x10^6$	$3.06x10^6$
Λ_V (W m^{-1} K^{-1})	21	21	21	21

[a] Ref. [77]
[b] Ref. [78]
[c] Ref. [79]

5.3 Measurement of the pyroelectric and electrocaloric coefficient of PZT epitaxial layers

Figure 5.1(a) shows the dependence of the pyroelectric current for a PZT/GSO capacitor on modulation frequency. The pyroelectric coefficient is adjusted to get the best fit between the measured current and the model calculation. We find Π= -170 μC m^{-2} K^{-1}. Figure 5.1(b) shows the dependence of the temperature change of the V film as a function of frequency for a PZT20:80/GSO capacitor. A DC bias voltage of 1.4 V is applied on the capacitor along with the AC voltage of amplitude of 1 V to produce a voltage that varies from 0.4 V to 2.4 V. (We determined empirically that the range of linearity extends to an AC voltage of amplitude 1 V.) The DC voltage is chosen to make sure that the ferroelectric layers do not switch polarization states under applied voltages. As shown below, by varying the DC bias voltage, we probe the hysteresis behavior of the electrocaloric coefficient. Adjusting the electrocaloric coefficient to get the best fit between the experimental data and the modeling calculation yields Σ = -130 μC m^{-2} K^{-1} for the PZT20:80 epitaxial layer on the GSO substrate. The adiabatic electrocaloric temperature change within the PZT layer is calculated as

$$\Delta T_a = -\frac{1}{C} T \frac{dS}{dE} \Delta E \tag{5.7}$$

Using the measured electrocaloric coefficient $dS/dE = \Sigma$ = -130 μC m^{-2} K^{-1}, $\Delta T_a \approx$ 0.1 K for a field change of 6.7 MV m^{-1}. We emphasize that our

electrocaloric method measures the total heat generated within the PZT layers through measuring the temperature change of the V film. The measured temperature change plotted in Figure 5.1(b) is much smaller than the adiabatic temperature change, *i.e.*, the temperature change of the PZT layer if the PZT layer was thermally isolated from the V film and substrate. While wires and contact tips needed to drive the electrocaloric effect are present, it does not affect the temperature measurement because of high modulation frequencies of the electric field.

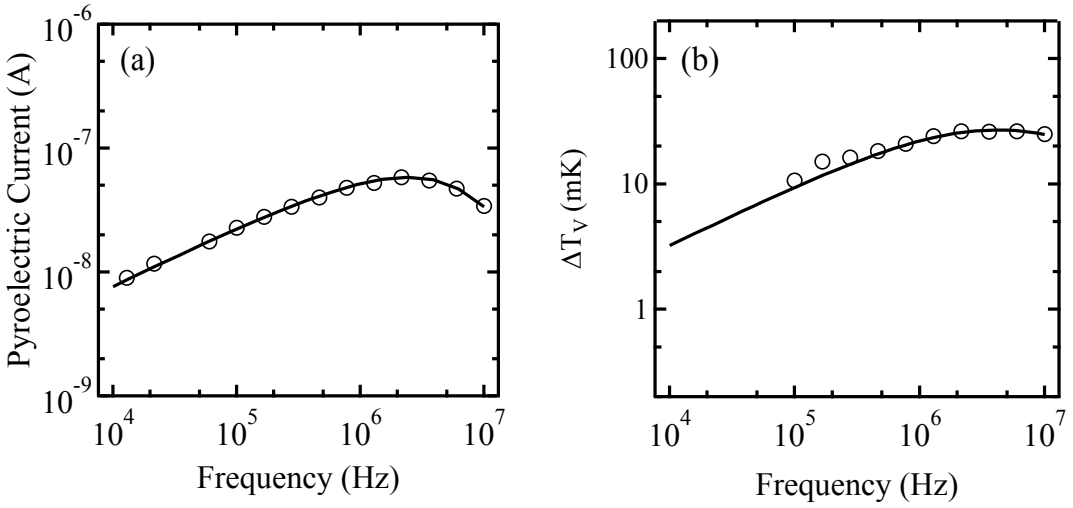

Figure 5.1 a) Frequency dependence of the pyroelectric current; and (b) frequency dependence of the temperature change of the V film for a PZT/GSO capacitor at room temperature. Measured data are shown as open circles and the solid lines are the model calculations used to determine (a) the total pyroelectric coefficient Π = -170 μC m^{-2} K^{-1}; and (b) the total electrocaloric coefficient, Σ = -130 μC m^{-2} K^{-1}. The laser power used in the pyroelectric smeasurement is 1 mW. The DC bias voltage and AC voltage used in the electrocaloric measurement are 1.4 V and 1 V, respectively.

The errors in our measurements depend largely on the uncertainties in the measurement of the laser power, ≈5%, and uncertainties of the

thermophysical properties of the materials in the capacitor structure, typically ≈10%. The sensitivity of the measurement to the various experimental parameters, *i.e.*, the error propagation, has been discussed in section 2.7 and 4.3. Propagation of errors from the thermophysical properties to the pyroelectric and electrocaloric data is similar; the propagation of errors from the laser power, however, has opposite sign. Therefore, the uncertainty in the *difference* between the pyroelectric and electrocaloric data is relatively insensitive to uncertainties in the thermophysical properties and mostly depends on the uncertainty in the measurement of the laser power. As a specific example, we estimate that measurements summarized by Figure 5.1 have total uncertainties of 10%, *i.e.*, $\Pi = -170 \pm 17$ μC m^{-2} K^{-1} and $\Sigma = -130 \pm 13$ μC m^{-2} K^{-1} while the uncertainty in the difference, $\Pi - \Sigma = -40 \pm 15$ μC m^{-2} K^{-1} is given by the sum of the contribution of the uncertainty of the laser power to the uncertainty in each measurement.

In our measurement, the detector is at an image of the sample surface so a small translation of the sample surface does not change the reflectivity. Another factor that could affect the optical reflectivity of the V films is strain. However, the lateral strain of V film is zero at high frequencies. Joule heating by the leakage currents under DC bias has no effect on the electrocaloric measurement because the look-in amplifier only picks up the temperature changes that are synchronous with the modulation frequency of

the electric field while the Joule heating is at double the modulation frequency.

We noted that in our electrocaloric and pyroelectric measurement, PZT layers are clamped on the fixed substrates. For the pyroelectric measurement, because of high modulation frequency of the heating laser (100 kHz – 10 Mhz), heat is confined laterally. Therefore, there is no in-plane contraction of the substrate and the PZT layers only contract in the out-of-plane direction. For the electrocaloric measurement, because the radius of the devices is very small compared to the size of the samples, the PZT layers only contract in the out-of-plane direction due to the converse piezoelectric effect.

5.4 Field dependence of the pyroelectric and electrocaloric coefficients

To directly compare the pyroelectric and electrocaloric coefficients, the two coefficients must be measured at the same bias field. Therefore, we measure the pyroelectric and electrocaloric coefficient as a function of DC bias voltage. For all 3 samples, our result shows that the pyroelectric and electrocaloric coefficient are not equal at the same field. Furthermore, the pyroelectric and electrocaloric coefficients show hysteresis that is consistent with the polarization measurement (Figure 5.2). The hysteresis curves for the polarization and the pyroelectric and electrocaloric coefficient are shifted horizontally. This shift could arise from slight differences in the top and

bottom contacts, trapped charges for the homogeneous PZT layer and the presence of strain gradients for the compositionally-graded PZT layer. [76,80-82] The coercive voltages in the pyroelectric measurement are smaller than the corresponding coercive voltages in the polarization measurement. This difference is explained by the fact that the bias voltage in the pyroelectric and electrocaloric measurement is changed slowly, with ~30 seconds intervals between each value of the bias voltage, while the polarization is measured at 1 kHz.

Furthermore, the electrocaloric hysteresis loops are even narrower than the pyroelectric curves. A smaller DC voltage is required to switch polarization in the electrocaloric measurement than the pyroelectric measurement because of the additional AC voltage used in the electrocaloric measurement. The pyroelectric and electrocaloric coefficients are independent of the DC voltage up to 3 V.

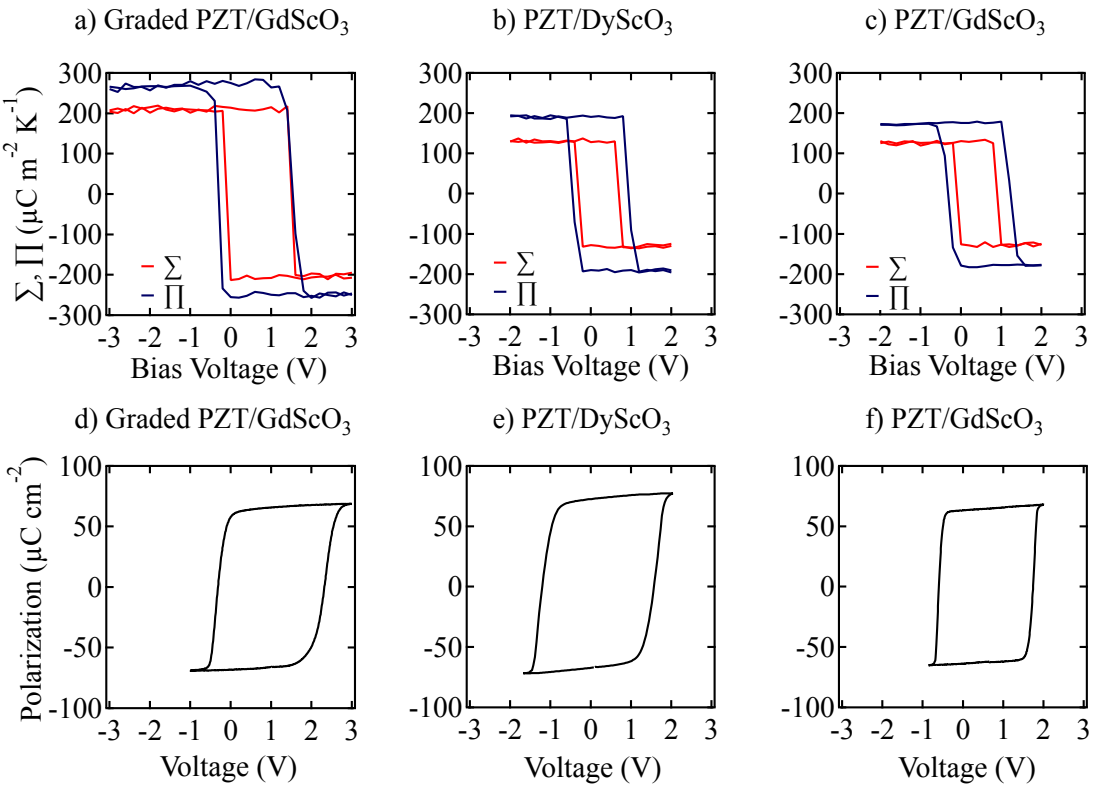

Figure 5.2 Hysteresis measurement of the total pyroelectric, electrocaloric coefficient and polarization of the PZT layers at room temperature. For the electrocaloric and pyroelectric measurements, a DC bias voltage is applied to the capacitors and the time between changes in the bias voltage is ~30 s with a increment of 0.1 V. Polarization is measured at a frequency of 1 kHz.

The field dependence of the electrocaloric effect has been studied previously for bulk materials. [83-86] However, in the prior work reported in Refs. [84-87], the adiabatic temperature changes are measured as a function of the change in electric field ($\Delta E = E_2 - E_1$ and E_1 is often chosen to be 0). For our measurement of the electric-field dependence, the amplitude of oscillating electric field which drives the electrocaloric effect, ΔE, is fixed and the DC bias voltage slowly varied from point-to-point. Since the adiabatic temperature change depends not only on ΔE but also on the polarization

state, our measurement provides a more complete picture of how the entropy changes with a small variation in electric field.

Our key result is that the measured electrocaloric and pyroelectric coefficients are not equal. If we calculate the adiabatic temperature change using the field dependence of the measured pyroelectric coefficient predicted and the Maxell relation, $\Delta T_a = -\frac{T}{C}\int_{E_1}^{E_2}\left(\frac{dP}{dT}\right)_E dE = -\frac{T}{C}\int_{E_1}^{E_2}\Pi(E)dE$, we find $\Delta T_a \approx$ 0.14 K for ΔE = 6.7 MV m^{-1} for the PZT20:80/DSO layer. This indirect measurement of the adiabatic temperature change is 40% higher than the value obtained by the direct measurement, 0.10 K. Note that while the conventional indirect method for the electrocaloric measurement extracts dP/dT from the temperature dependence of the polarization at different field[34], our pyroelectric measurement directly measures the dependence of dP/dT on electric field.

5.5 Temperature dependence of the pyroelectric and electrocaloric coefficients

To further probe the differences between Σ and Π, we measured the pyroelectric and electrocaloric coefficients as a function of temperature from room temperature to 220 ^{o}C for the three PZT epitaxial layers (Figure 5.3). The pyroelectric coefficient (square symbols) increases with elevated temperature for all samples while the electrocaloric coefficient (triangles) has a weaker dependence on temperature. The graded-PZT layer has a higher

pyroelectric coefficient and electrocaloric coefficient than the homogeneous layers.

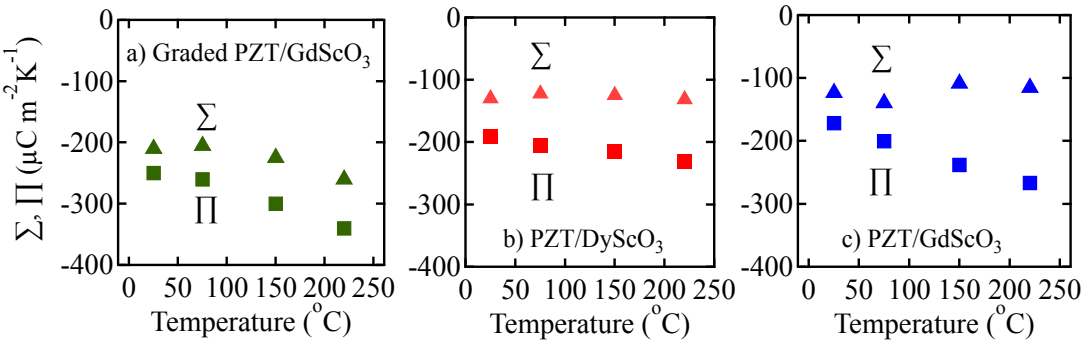

Figure 5.3 Dependence on sample temperature of the total electrocaloric (triangle symbols) and pyroelectric (square symbols) coefficients of PZT epitaxial layers on $DyScO_3$ and $GdScO_3$ substrates.

Our data are in qualitative agreement with the result from Ref. [36]. In Ref. [36], the temperature change measured by the direct method is smaller than the temperature change inferred by the indirect method. The difference increases from ~ 10 % at the room temperature to ~ 40% at ~340 K and then decreases with further increases in temperature.

Figure 5.4 shows the difference between the total pyroelectric and electrocaloric coefficients. The corresponding value of d_{33} using Eq. (5.6), is plotted as the right-hand axis in Figure 5.4. The values of d_{33} fall in the same range with those reported for PZT layers. [87,88] We see that d_{33} increases with increasing temperature for all samples, consistent with previous studies of PZT epitaxial layers[89] and $LiTaO_3$ crystals. [90]

At high temperatures, the secondary electrocaloric coefficient by piezoelectric strain and the elastocaloric effect is comparable to the primary coefficient. For example, for the PZT20:80/$GdScO_3$ sample at 200°C, $\Sigma \approx -100$ μC m^{-2} K^{-1}; $\Sigma - \Pi \approx 150$ μC m^{-2} K^{-1}; and therefore $\Sigma' \approx -400$ μC m^{-2} K^{-1} and $\Sigma'' \approx 300$ μC m^{-2} K^{-1}.

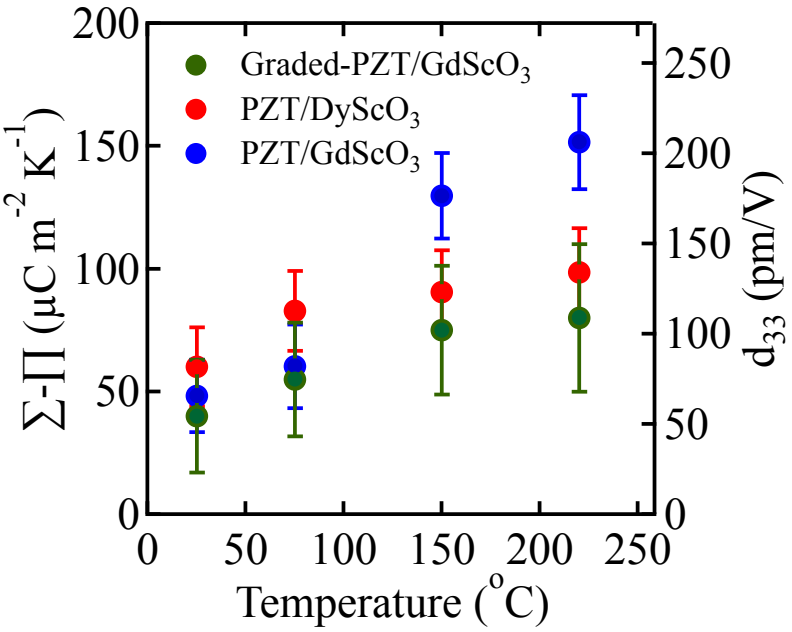

Figure 5.4 Temperature dependence of the *difference* between the total electrocaloric coefficient and pyroelectric coefficient of PZT epitaxial layers due to the secondary contribution. The converse piezoelectric coefficient d_{33} calculated based on Eq. (5.6). The error bar is calculated with uncertainties of the pyroelectric and electrocaloric measurement to be 5%.

Large elastocaloric effects have been found in shape-memory alloys[91] and predicted theoretically for $Ba_{0.5}Sr_{0.5}TiO_3$ (BST). [90] A temperature change of ~ 9 K is estimated for BST with a strain of 0.008. The authors of Ref. [90]attributed this giant elastocaloric effect of BST to a stress-induced

ferroelectric structural phase transition. For a qualitative comparison, using Eq. (5.7), we estimate a temperature change ~ 1.5 K under the same strain for our PZT layers. While the stand-alone elastocaloric effect can be comparable to the electrocaloric effect, our data shows that elastocaloric effect induced by piezoelectric effect competes with the electrocaloric effect for typical ferroelectric materials.

5.6 Conclusion

We anticipate that our novel methods for studying the electrocaloric and pyroelectric effect in thin epitaxial layers will provide new insights on caloric effects in pyroelectric and ferroelectric materials. These methods overcome experimental limitations of previous techniques that previously restricted widespread study of caloric effects in thin layers. Our results show that secondary, mechanical effects produce a significant contribution to the entropy change for clamped films.

CHAPTER 6

PYROELECTRIC EFFECT OF SOL-GEL PZT THIN FILMS

6.1 Introduction

Sol-gel method (solution deposition) has been used as early as the 19th century[92] in the ceramic industry for the development of glass from colloidal solutions of metal alkoxides. It is also a common method to produce ceramic products such as film, monoliths and membranes. [93,94] While physical deposition such as molecular beam expitaxy (MBE) and pulsed laser deposition (PLD) can produce films with greater structural perfection, sol-gel method offers many advantages: reliable films over large area (up to 10 cm^2)can be synthesized with proper executed process; and low cost (no requirement of complex vacuum systems)[95]. Furthermore, with development of film-on-foil technology, the sol-gel method is realized as being highly scalable, tend to be more robust for integrating ferroelectric films in electronic devices.[95] By utilizing a carrier substrate that enables high temperature processing, ferroelectric films can be fabricated before embedding in devices.

We followed the sol-gel process which has been successfully used to fabricate ferroelectric thin films[34,96-98] to synthesize $PbZr_{0.2}Ti_{0.8}O_3$ thin films. X-ray diffraction and Rutherford back scattering are used to characterize physical properties of the thin films. Finally, we applied the wide range frequency pyroelectric technique to measure the pyroelectric coefficient of the PZT thin films.

6.1.1 Precursor solution preparation

Precursor solutions are synthesized using the hybrid sol-gel chelate route (IMO process) (See Figure 6.1). [34,95] First, lead acetate trihydrate is dissolved in methanol. The mixture is refluxed at 70 ^oC for 2 hours followed by cooling down to room temperature. The amount of methanol used in this step is about 1/6 of the total methanol volume in the final PZT solutions. The refluxing temperature should not be too high (> 90 ^oC) to prevent lead oxidation. At the same time, zirconium propoxide and titanium butoxide is mixed at a stoichiometry ratio and quickly stirred in ~ 1 minute. Then 4 equivalents of acetic acid is added to the mixture followed by stirring in ~ 5 minutes before adding a methanol volume which is ~ 1/6 the total methanol volume in final PZT solutions. The resultant solution is stirred at room temperature for 2 hours. The lead solution and zirconium and titanium solutions are mixed and stirred for 1 hour followed by adding 8 equivalents of acetic acid. Finally, methanol is added to adjust the concentration of the PZT solutions to 0.4M. We note that because zirconium propoxide and titanium

propoxide will hydrolyze when exposed to humid air quickly (in a matter of minutes, especially titanium propoxide), mixing and stirring the mixture of zirconium and titanium precursors before adding acetic acid should not be longer than a couple of minutes. Longer stirring time will result a more homogeneous mixture but preventing hydrolysis is more important. The mixture should be clear and have no visible solids. After adding acetic acid, the solution will be stable in the air because acetic acid serves as a chelating agent to slow down the hydrolysis of the alkoxide species. To prevent lead loss during the thermal treatment step, 10% lead excess is used. After aging for 24 hours, the PZT solution is passed through 0.2 μm filters.

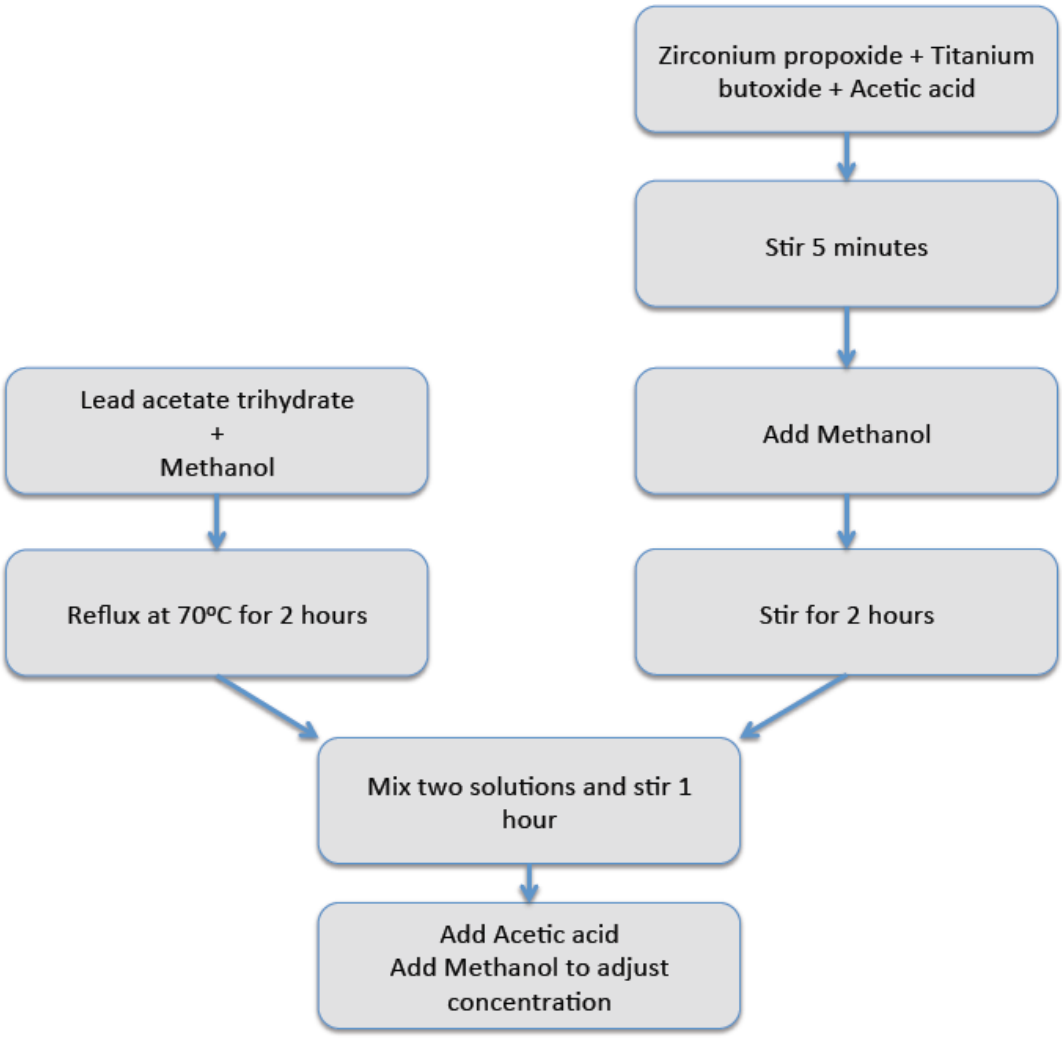

Figure 6.1 Schematic of the PZT solution precursor preparation

6.1.2 Deposition and crystallization of PZT thin films

The PZT thin films are deposited on Pt(111)/Ti/SiO_2/Si substrates by multiple spin coating of the precursor solutions. Each layer is spin coated for 30 seconds at 3000 rpm followed by heating at 350 ^{O}C on a hot plate. The thickness of each layer is ~ 84 nm. The final thin films are annealed at ~ 650

^{O}C in a box furnace for 10 minutes. The furnace is preheated to the desired temperature to mimic rapid thermal anneal. We made samples with the thickness of ~ 84 nm and 174 nm.

6.2 PZT thin film characterization

XRD was performed on the PZT films with one and two coating layers to study the crystal structure of the films. Figure 6.2 shows the X-ray diffraction patterns for the PZT films at different annealing temperatures. The XRD pattern of the substrate alone is included for comparison. For all samples, the phase intensity of platinum is high because the PZT films are thin. The X-ray diffraction pattern reveals that the fabricated PZT films are perovskite phase with no pyrochlore phase. The XRD graph shows that the texture of the films exhibited an (100) orientation preference with the tetragonal crystal structure (a = 3.9539 Å, c = 4.1319 Å). The preparation of the sol solution, the spin-coating process and the heat treatment are effective for the phase development of PZT films.

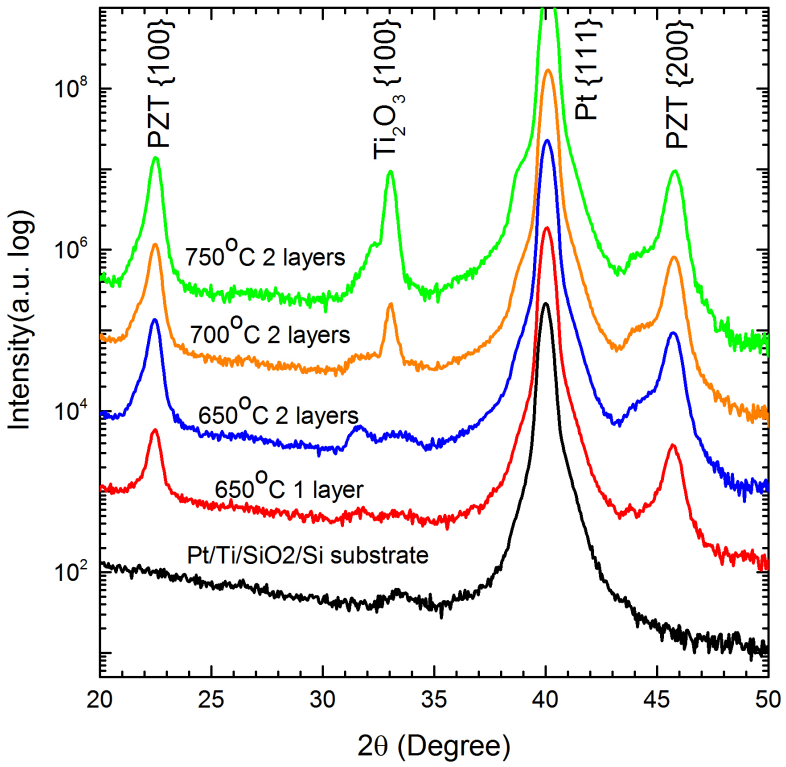

Figure 6.2 X-ray diffraction patterns of PZT thin films at different annealing temperatures. A pattern of the substrate is included for comparison.

The precise thickness and composition of the PZT films are measured by the Rutherford Back Scattering (RBS). Figure 6.3 shows the RBS spectra of the PZT films with one (a) and two (b) spin coating layers. We can see that the Pt spectrums are highest and overlap with the Zr and Ti spectrums. To differentiate the Zr and Ti spectrums from the spectrums, the incident angle of ion beams are changed to zero. The thickness of the PZT thin films for one and two spin coating layers is 84 nm and 174 nm respectively. The Zr and Ti compositions are 19% and 81% respectively. This concentration is chosen for comparison with PZT films grown by PLD technique as discussed in Chapter 3 and 5

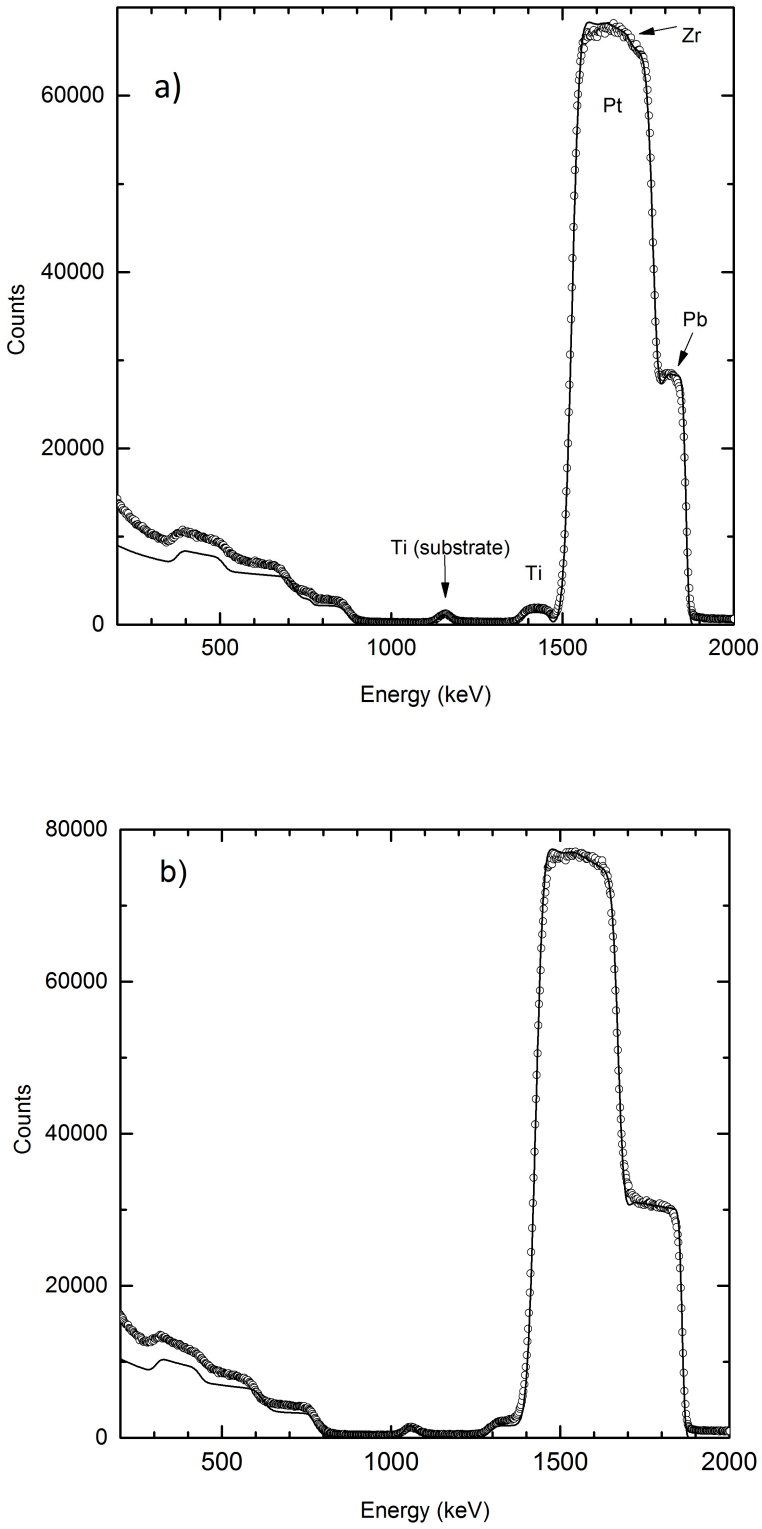

Figure 6.3 RBS measurement of PZT thin films with one (a) and two (b) spin coating layers

6.3 Pyroelectric measurement

Figure 6.4 shows the pyroelectric measurement of the PZT film with the thickness of 174 nm. The pyroelectric coefficient is measured to be 135 μC m^{-2} K^{-1}. The pyroelectric current is proportional to f for the f < 100 MHz and reaches to a peak at f ~ 1 MHz. Note that we adjusted capacitances of devices to get the best fit at high frequency (f > 1 MHz). We did not observe the secondary effect which will cause an increasing pyroelectric coeffient at the low frequency limit (See Section 3.3).

To explain this observation, we calculated the average temperature T_{avg} as a function of frequency (See Figure 6.5). We can see that T_{avg} is almost constant for f < 100 MHz then decreases with increasing frequencies (See Figure 6.5(a)) and the phase angle is about zero which means that the temperature is in phase with the heat flux. This is due to the fact that the Si substrate has a high thermal conductivity (~ 140 W m^{-1} K^{-1}) which results in long thermal penetration depth. Therefore, the temperature is homogenous over a broader frequency range compared with one of the PZT films on DSO substrates with a very low thermal conductivity ~ 2.7 W m^{-1} K^{-1}). The frequency at which the thermal penetration depth in the Si substrates is equal that in the DSO substrates is ~ two order of magnitude higher than the frequency for the DSO substrates, $\frac{f_{Si}}{f_{DSO}} = \frac{\Lambda_{Si}}{\Lambda_{DSO}} \frac{C_{DSO}}{C_{Si}} = 88$. This is consistent with our experiment data which shows no change in the pyroelectric

coefficient at ~ 1 kHz. We can expect that the secondary effect will show up with f > 100 kHz. Unfortunately, we are not able to get a correct data fitting for the pyroelectric coefficient because of the capacitance effect which can cause a error bar larger than change of the pyroelectric coefficient by the secondary contribution.

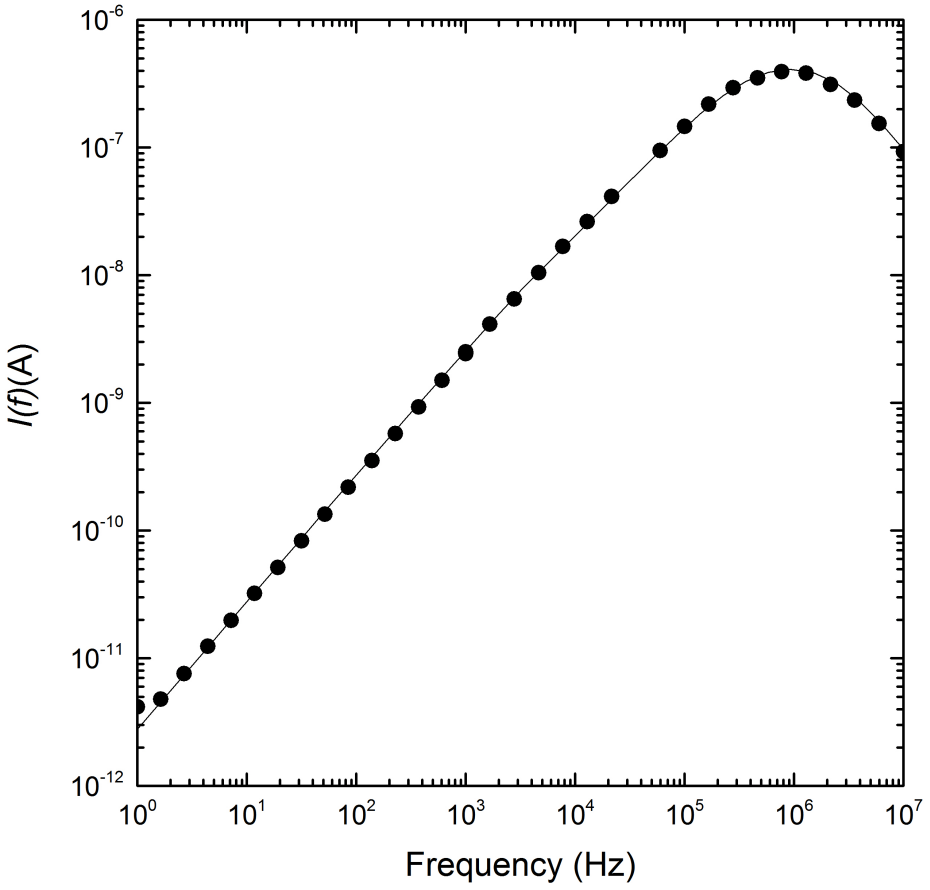

Figure 6.4 Frequency dependence of the amplitude of the pyroelectric current of the PZT film with the thickness of 174 nm. Measured data are shown as open circles and the solid line is the model calculations for a fixed value of the pyroelectric coefficient. The laser power is 10 mW. The top electrode radius is 50 μm.

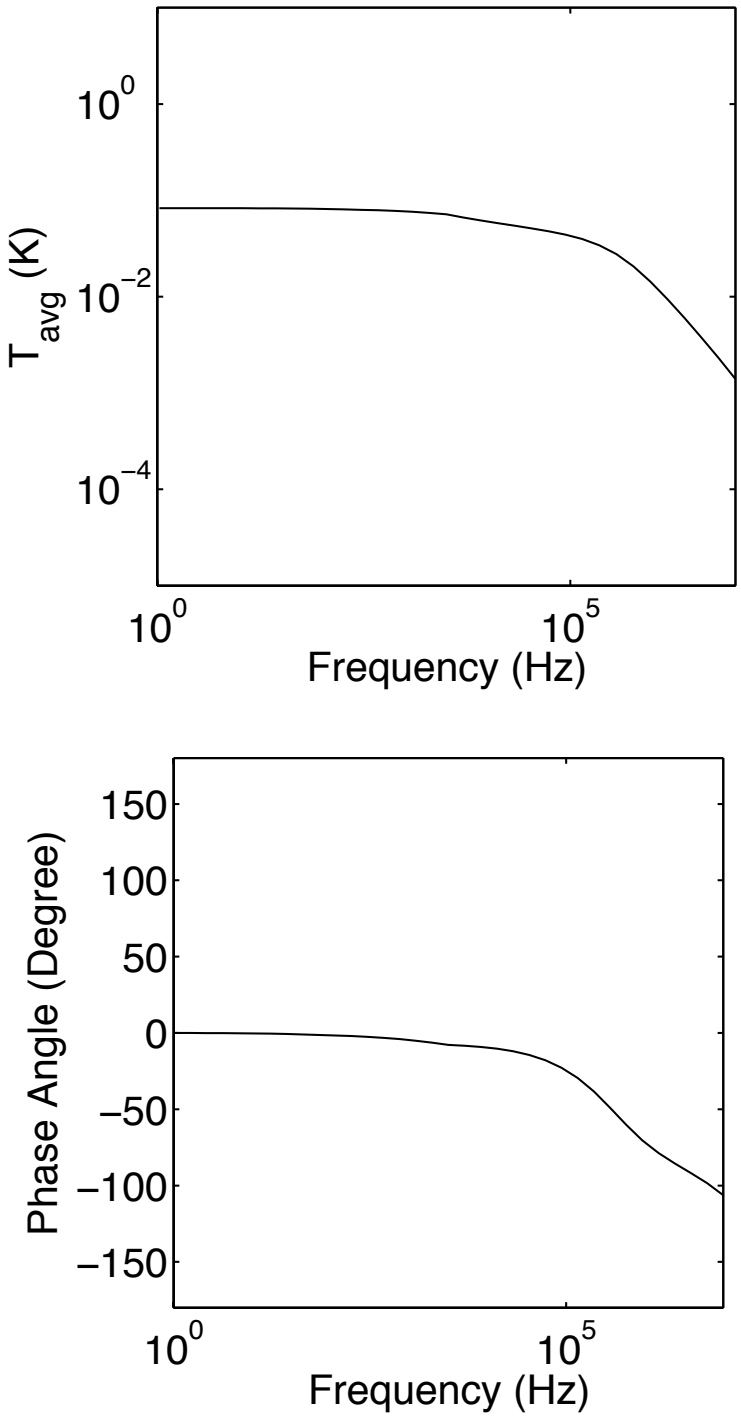

Figure 6.5 The frequency dependence of the average temperature amplitude and phase angle of the PZT film on Pt/Ti/SiO2/Si substrate.

6.4 Conclusion

We successfully fabricated PZT thin films by the sol-gel method. The PZT thin films have the tetragonal crystal structure with (100) orientation preferred. The pyroelectric coefficient of the PZT thin films is measured to be 135 $\mu C\ m^{-2}\ K^{-1}$. A long thermal penetration depth prevents ability to measure the secondary pyroelectric contribution.

CHAPTER 7

CONCLUSIONS

The novel laser-based techniques are powerful tools for studying the pyroelectric and electrocaloric effects in thin films. These techniques overcome limitations of conventional methods to enable direct measurements of both effects in thin films. Furthermore, the pyroelectric measurement is capable of measuring the secondary pyrolectric effect by probing thin films in different boundary conditions by changing the thermal penetration depth. Combining the pyroelectric and electrocaloric measurement enables to study the secondary electrocaloric effect.

The implementation and data analysis of the pyroelectric and electrocaloric techniques are described in detail in Chapter 2 and 4. In the same optical setup, both measurements can be performed with few adjustments. While the laser power is used to create change of the temperature in the pyroelectric measurement, it is used to measure the temperature change generated by the electrocaloric effect through change of the reflected laser intensity. Lock-in technique is applied to both methods to

improve signal-to-noise ratio. The modulation frequency range is from 1 Hz to 10 MHz, which provides wide-ranging control on the thermal penetration depth. Multilayer thermal heat transport models are successfully developed to provide analytical solutions of the temperature change generated by a modulated laser power or spatially distributed heat flux in the pyroelectric and electrocaloric measurement, respectively.

The wide range frequency pyroelectric measurement is applied to study $Pb(Zr,Ti)O_3$ and $(Ba,Sr)TiO_3$ thin films grown by Pulse Laser Deposition (PLD). We found that the pyroelectric coefficients at high and low frequency limits are different. This is due to different boundary conditions caused by short and long thermal penetration depths at high and low frequencies. The secondary contribution to the pyroelectric coefficient of the PZT and BST films are measured to be ~ 15% and 20% respectively.

The pyroelectric and electrocaloric measurement are applied to measure $Pb(Zr,Ti)O_3$ thin films by PLD under different temperatures and applied electric fields. The measured pyroelectric and electrocaloric coefficients are different at the same measurement conditions due to secondary contribution to the total electrocaloric effect that is created by a combination of piezoelectric and elastocaloric effects. The secondary contribution to the electrocaloric coefficient has the opposite sign as the primary effect and therefore reduces the overall entropy change of PZT thin

films in an electric field. The absolute magnitude of the secondary effect is comparable to the primary effect at elevated temperatures of ≈200°C.

The pyroelectric coefficient of PZT thin films grown by a sol-gel method on $Pt/Ti/SiO_2/Si$ substrates is measured to be ~ 135 W m^{-2} K^{-1} and the secondary pyroelectric effect is not observed. We attribute this observation to the fact that high thermal conductivity substrates pushes low and high frequency limit boundary toward a higher frequency at which the capacitance effect prevents a correct measurement of the secondary contribution.

APPENDIX A

THERMAL CONDUCTIVITY OF InGaN ALLOYS

This chapter is published in "Suppression of thermal conductivity in $In_xGa_{1-x}N$ alloys by cation substitution and nanometer-scale disorder", T. Tong, D. Fu, A. X. Levander, W. J. Schaff, B. N. Pantha, B. Liu, R. Zhang, J. Y. Lin, H. X. Jiang, J. Wu, and David. G. Cahill, *Appl. Phys. Lett.* **102**, 121906 (2013)

A.1 Introduction

$In_xGa_{1-x}N$ alloys with Ga-rich compositions ($x < 0.3$) are used as active layers for light emitting diodes in the short-wavelength region, $400 < \lambda < 530$ nm. Applications at longer wavelengths, green emission, are limited by an abrupt drop in the quantum efficiency that typically occurs at $x > 0.3$. Compositional inhomogeneities and structural defects have been proposed as possible reasons for this drop in quantum efficiency. [99] We have recently demonstrated that thermal conductivity measurements can reveal disorder in epitaxial layers that is difficult to identified by traditional x-ray diffraction (XRD) or transmission electron microscopy (TEM). [100] Here, we use thermal conductivity measurements to reveal nanometer-scale disorder

in $In_xGa_{1-x}N$ alloys that extends over a wide range of compositions, and the results indicate the strongest disorder exists for compositions $0.2 < x < 0.6$, approximately corresponding to the $In_xGa_{1-x}N$ miscibility gap. [101,102]

$In_xGa_{1-x}N$ alloys show promise for efficient thermoelectric energy conversion in addition to their applications in solid-state lighting. [103,104] The thermoelectric figure-of-merit, $ZT = S^2\sigma T/\Lambda$, where S, σ, Λ and T are the Seebeck coefficient, electrical conductivity, thermal conductivity and temperature, respectively, has been reported to be comparable to the figure-of-merit of SiGe alloys. [103,105] High-efficiency conversion of heat to electrical power requires low lattice thermal conductivity while maintaining high mobility of the charge carriers. The binary InN and GaN materials have high thermal conductivity materials[106-111](the room-temperature thermal conductivity of GaN and InN are 230 and 120 W m^{-1} K^{-1}, respectively) however, the thermal conductivity of even relatively dilute $In_xGa_{1-x}N$ alloys is significantly reduced because of scattering of high-frequency phonons by mass disorder. [112]

A.2 Sample preparation

Four sets of $In_xGa_{1-x}N$ epitaxial layers with various thicknesses were grown by molecular beam epitaxy (MBE) and metalorganic chemical vapor deposition (MOCVD) on *c*-sapphire substrates at four different institutions. [113-115] Growth conditions, sample structures, compositions, and thermal conductivities are summarized in Table A.1. Sample numbers 5 and 9 were

the subject of a prior study of composition modulation in $In_xGa_{1-x}N$ alloys by TEM and XRD. [114] Liliental-Weber *et al.* (see Ref. [114]) observed periodic modulations in composition along the *c*-axis with a period of ≈5 nm for x = 0.55 and ≈7 nm for x = 0.78. They observed a columnar growth morphology with columns separated by edge dislocations, where the average dislocation density was $\approx 10^{11}$ cm^{-2} and 6×10^{10} cm^{-2} for x = 0.55 and x = 0.78, respectively.

A.3 Sample characterization

Figure A.1(a) shows XRD θ-2θ scan data of the (0002) reflections for selected $In_xGa_{1-x}N$ samples. All samples show a single (0002) reflection; the lack of secondary peaks indicates that these samples do not exhibit gross extended domains that are phase-separated into Ga-rich and In-rich alloys. [116,117] Figure A.1(b) shows the $In_xGa_{1-x}N$ *c*-lattice parameter as a function of the In content of selected samples determined by Rutherford backscattering spectrometry (RBS). The *c*-lattice parameters are in good agreement with Vegard's law, where the layers are assumed to be fully relaxed. The full-width-at-half-maximum (FWHM) of the XRD peaks is plotted in Figure A.1(c). The XRD peaks are strongly broadened, presumably by inhomogeneous strain fields created by plastic deformation that relaxes the epitaxial stresses imposed by the substrate.

Table A.1 Summary of all $In_xGa_{1-x}N$ samples investigated. The samples were grown by MOCVD or MBE method on sapphire substrates with GaN or AlN buffer layers at four institutions. The composition is determined by XRD and RBS. The thermal conductivities are measured by time-domain thermoreflectance.

Samples	Growth technique	In fraction (RBS)	In fraction (XRD)	Thickness (nm)	Buffer layer	Thermal conductivity Λ ($W\ m^{-1}\ K^{-1}$)
1	MOCVD	0.08	0.07	229	GaN	24
2	MOCVD	0.11	0.10	233	GaN	13
3	MOCVD	0.17	0.16	268	GaN	8.5
4	MOCVD	0.25	0.25	608	AlN	2.8
5	MBE	0.44	0.48	147	GaN	2.2
6	MBE	0.56	0.55	398	GaN	2.5
7	MOCVD	0.64	0.65	560	AlN	3.8
8	MBE	0.70	0.64	500	GaN	4.1
9	MBE	0.72	0.72	364	GaN	4.3
10	MBE	0.80	0.78	302	None	5.1
11	MOCVD	0.80	0.82	723	AlN	5.3
12	MOCVD	0.79	0.83	223	GaN	4.8
13	MOCVD	0.84	0.90	222	GaN	5.6
14	MOCVD	0.90	0.93	756	AlN	8.5
15	MBE	0.98	0.99	4600	GaN	73

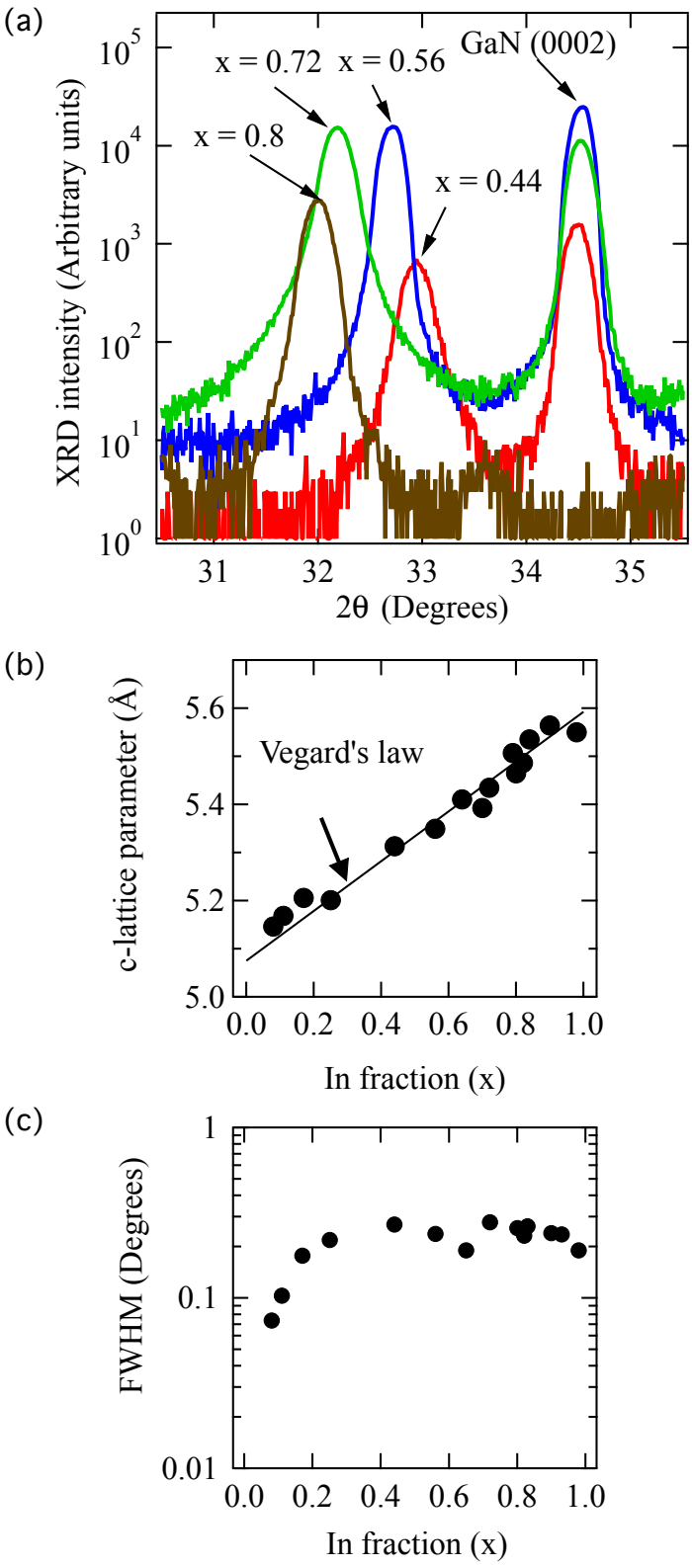

Figure A.1 (a) XRD θ-2θ scan patterns for selected $In_xGa_{1-x}N$ samples in the vicinity of the (0002) reflection. (b) XRD c-lattice parameter of $In_xGa_{1-x}N$

(*fig. A.1 cont.)* alloys vs. In composition measured by RBS. The solid line shows the prediction of Vegard's law; the good agreement suggests that the $In_xGa_{1-x}N$ layers are fully relaxed. (c) Full-width-at-half-maximum (FWHM) of the $In_xGa_{1-x}N$ (0002) reflection vs. In composition

Each sample was coated with a ≈80 nm thick layer of Al by magnetron sputter deposition at room temperature to prepare the samples for thermal conductivity measurements. This Al layer serves as an optical transducer in the measurement of thermal conductivity by time-domain thermoreflectance (TDTR). [49] Details of the measurement setup are described in Ref. [118]. In a TDTR measurement, a laser beam from a mode-locked Ti: sapphire laser is split into a pump beam and a probe beam with the relative optical path adjusted by a mechanical delay stage. The pump beam is modulated at 9.8 MHz by an electro-optic modulator. The pump and probe beam are focused on the sample to a $1/e^2$ radius of ≈5 μm. The Al layer is heated by the pump beam and the temperature change of the Al layer is monitored by the probe beam through the temperature dependence of the optical reflectivity of Al. Signals obtained by a photo-detector are sent to a lock-in amplifier to detect the 9.8 MHz component that is synchronous with the modulation of the pump beam.

The ratio of in-phase (V_{in}) and out-of-phase (V_{out}) signals were compared with a multilayer thermal transport model. [49] Fitting parameters used in the model include thickness, heat capacity and thermal conductivity of each layer. The Al thickness was determined by picosecond acoustics. The rule of mixtures was used to calculate heat capacities of $In_xGa_{1-x}N$ alloys, C_{InGaN} =

$xC_{InN} + (1-x)C_{GaN}$; here $C_{InN} = 2.1$ J cm^{-3} K^{-1} [119] and $C_{GaN} = 2.6$ J cm^{-3} K^{-1}. [120] The thermal penetration depth is $\delta = \sqrt{\Lambda/(C\pi f)} \approx 200$ nm. Alloy layers with thickness $d > \delta$ are "thermally-thick" and the thermal conductance of the alloy-layer/buffer-layer interface G_b and the thermal conductivity of buffer-layer are unimportant in the model. Since the acoustic impedance difference between alloy layers and GaN buffer layers is small, for the low-In alloy layers with $d < \delta$, it can expected that the interfacial thermal conductance is high. Furthermore, the intermediate In composition alloys with $d < \delta$ grown on high thermal conductivity GaN buffer layers produce only a small correction to the model. Hence, we do not include the interfacial thermal conductance in the model. Since the samples grown on AlN buffer layers are thermally thick, the uncertainty of the thermal conductivity of AlN layers which could be as low as 1 W m^{-1} K^{-1} [121]has no effect on the model. The thermal conductivity of the $In_xGa_{1-x}N$ layer and the thermal conductance of the interface between the Al layer and the $In_xGa_{1-x}N$ layer are the only significant unknowns. These two free parameters were adjusted to give the best fit between the model and the experimental data.

A.4 Results

The thermal conductivity of $In_xGa_{1-x}N$ alloys at room temperature is plotted in Figure A.2(a). We include data from prior studies of $In_xGa_{1-x}N$ alloys for comparison. Sztein *et al.* studied *n*-type $In_xGa_{1-x}N$ films[122] (81 to 190 nm thick) deposited by MOCVD on Fe:GaN/sapphire. Pantha *et al.*

studied $In_xGa_{1-x}N$ films (≈110 nm thick) grown by MOCVD on GaN/sapphire templates. In these studies, the thermal conductivity of the epitaxial layers was measured by a differential 3ω method. The thermal conductivity of $In_xGa_{1-x}N$ alloys reaches a minimum in our data set of 2.2 W m^{-1} K^{-1} at x = 0.44.

A.5 Calculation of the thermal conductivity of InGaN alloys

A Callaway model[123] as modified by Morreli *et al.* [124] is used to calculate the lattice thermal conductivity to gain quantitative insight into the strength of the phonon scattering mechanisms. In this model, the longitudinal and transverse phonon modes are independently investigated. The total thermal conductivity is a sum over one longitudinal (Λ_L) and two degenerate transverse (Λ_T) components, $\Lambda=\Lambda_L + 2\Lambda_T$ where $\Lambda_L = \Lambda_{L1} + \Lambda_{L2}$ and $\Lambda_T = \Lambda_{T1} + \Lambda_{T2}$. The partial conductivities Λ_{L1}, Λ_{L2}, Λ_{T1} and Λ_{T2} are the Debye-Callaway terms (See Eqs. 3a, 3b, 4a, 4b of Ref. [124]). Debye temperatures and speeds of sound are calculated separately for acoustic phonon branches in the [001] direction. The cutoff frequencies f_c are set at the zone boundary of the acoustic phonon dispersion curves and the Debye temperatures were calculated from these frequencies, $T_D = hf_c/k_B$**,** where k_B is Boltzmann constant.

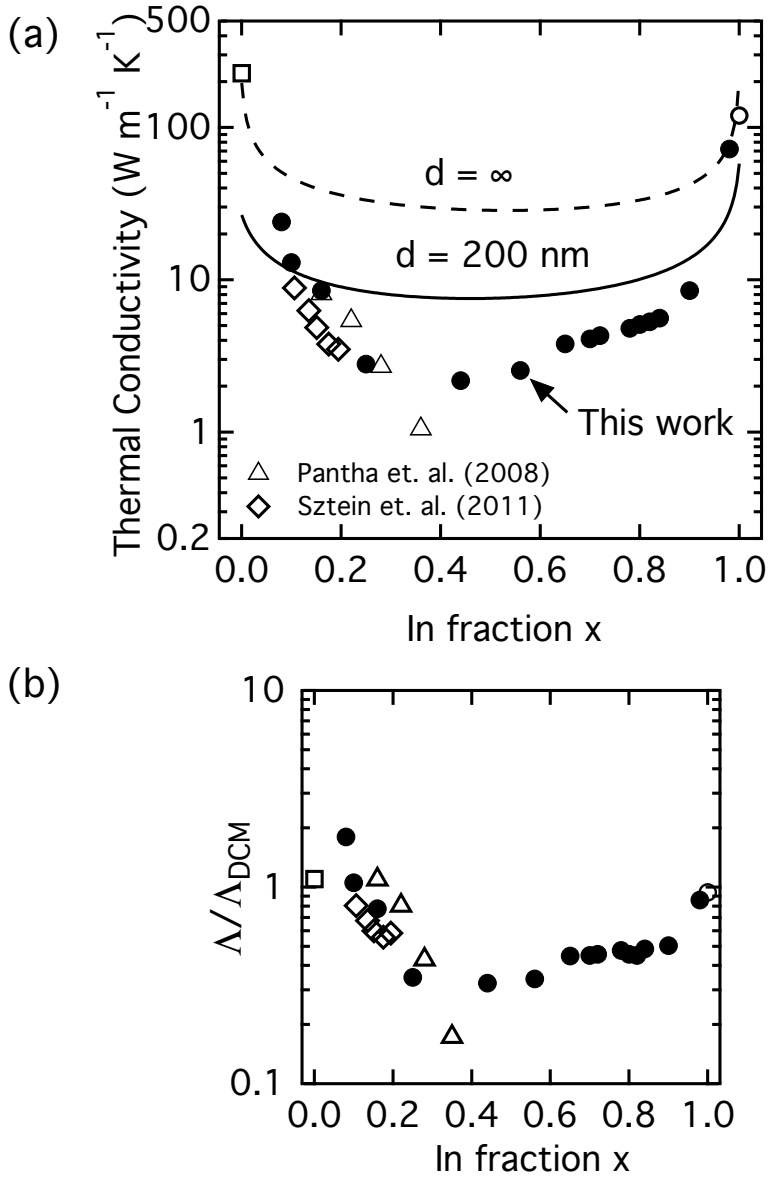

Figure A.2 (a) The thermal conductivity (Λ) at room temperature of $In_xGa_{1-x}N$ alloys as a function of In fraction compared to the predictions of the modified Callaway model. Previously reported thermal conductivities of GaN, InN and $In_xGa_{1-x}N$ alloys are included for comparison. The open-square and open-circle is the thermal conductivity of pure GaN (Ref. [106]) and pure InN (Ref. [107]) respectively. The dashed line is calculated for the limit of large layer thickness; the solid line is calculation for a layer thickness of d = 200 nm. (b) Ratio of the measured thermal conductivity from this work to the calculated thermal conductivity (Λ_{DCM}) at each thickness as a function of In content.

Grüneisen parameters of $\gamma_L = 0.73$ and $\gamma_T = 0.51$ were assumed for all alloy compositions and a virtual crystal model was used to determine the speeds of sound, densities, and cut-off frequencies of the alloys. The longitudinal speeds of sound were measured for selected samples (x = 0.44, 0.65, 0.9 and 0.93) by picosecond acoustics to provide greater confidence in the validity of this approximation. The data are in good agreement with the virtual crystal approximation. Table A.2 Material parameters of InN and GaN used in the Callaway-type model of the thermal conductivity of $In_xGa_{1-x}N$ alloys. summarizes the parameters used in our model.

Table A.2 Material parameters of InN and GaN used in the Callaway-type model of the thermal conductivity of $In_xGa_{1-x}N$ alloys.

	$T_D^L(K)$[a]	$T_D^T(K)$[a]	υ_L[b] (m/s)	υ_T[b] (m/s)
InN	278	194	5720	2650
GaN	305	157	7770	3950

[a] T_D^L and T_D^T are, respectively, longitudinal and transverse cut-off Debye temperatures calculated from Ref. {Bungaro:2000um}.
[b] υ_L and υ_T are, respectively, speeds of sound for longitudinal and transverse phonon dispersion branches calculated from Ref. {Wright:1997jm}.

The resistive scattering rate includes contributions from phonon-phonon Umklapp scattering (τ_U); point defect scattering due to mass disorder and bond length disorder (τ_I); and boundary scattering (τ_B). Typically the high temperature form of the normal process scattering rate[125] is taken as[126]:

$$(\tau_N)^{-1} = \frac{k_B \lambda^2 V^{1/3}}{M \upsilon^3} \omega^2 T \tag{A.1}$$

Here, γ is the Grüneisen parameter, V is the volume per atom, M is the average mass of the atoms in the alloys given by $M = xM_A + (1\text{-}x)M_B$ and M_A, M_B are the atomic weights of alloy components (GaN and InN for $In_xGa_{1-x}N$ alloys), υ is speed of sound, ω is the phonon frequency.

Klemens derived a form of the phonon scattering due to point defect disorder[127]

$$(\tau)^{-1} = \frac{\Gamma V}{4\pi \upsilon^3} \omega^4 \tag{A.2}$$

Γ is a coefficient that characterizes the strength of phonon scattering and for mass disorder in alloys with a basis of 2 atoms, [128]

$$\Gamma = x\left(\frac{M_A - M}{M}\right)^2 + (1-x)\left(\frac{M_B - M}{M}\right)^2 \tag{A.3}$$

The phonon boundary scattering rate is given by $(\tau_B)^{-1} = \upsilon/d$, where d is the thickness of the sample and υ velocity of each acoustic mode. The thicknesses of the samples in our study are not constant but the dependence of the model on the boundary scattering rate is weak. (Changing d by a factor of 2 creates a change in the thermal conductivity of a factor of 1.2). Moreover, since the thermal conductivity of semiconductor alloys measured by TDTR is not governed by the phonons with mean free paths larger than the thermal penetration depth, the thermal penetration depth can be used as an effective film thickness for alloys with $d > \delta$.

The contribution of phonon scattering by dislocation cores and the long-ranged strain field of dislocations was also considered. [129] Dislocations significantly reduce the thermal conductivity of high thermal conductivity pure crystals such as GaN. [121] However, these calculations show that the disorder alloy scattering rate is approximately an order of magnitude higher than the dislocation scattering rate even for a very high dislocation density of 10^{12} cm^{-2}. Inclusion of the dislocation scattering rate at a density of 10^{12} cm^{-2} suppresses the thermal conductivity by only ≈10% for In compositions $0.2 < x < 0.9$. Therefore, phonon scattering by dislocations was not used in this model.

A.6 Comparison between experimental data with modeling

The solid line in the Figure A.2 (a) The thermal conductivity (Λ) at room temperature of $In_xGa_{1-x}N$ alloys as a function of In fraction compared to the predictions of the modified Callaway model. Previously reported thermal conductivities of GaN, InN and $In_xGa_{1-x}N$ alloys are included for comparison. The open-square and open-circle is the thermal conductivity of pure GaN (Ref. [106]) and pure InN (Ref. [107]) respectively. The dashed line is calculated for the limit of large layer thickness; the solid line is calculation for a layer thickness of d = 200 nm. (b) Ratio of the measured thermal conductivity from this work to the calculated thermal conductivity (Λ_{DCM}) at

each thickness as a function of In content.(a) shows the results of this calculation for the thermal conductivity as a function of InN composition at a fixed thickness of 200 nm, which is the average value of the effective thickness of the films. It is noted that the calculated thermal conductivity of the pure GaN and InN samples is much smaller than the experimental data. This discrepancy is created by the boundary scattering in this modelwhich, creates a much stronger reduction of the thermal conductivity of the pure crystals than the alloy. (The thicknesses of the GaN and InN layers were 200 μm and 1 μm, respectively). If the boundary scattering is removed, this model (the dashed line in Figure A.2 (a) The thermal conductivity (Λ) at room temperature of $In_xGa_{1-x}N$ alloys as a function of In fraction compared to the predictions of the modified Callaway model. Previously reported thermal conductivities of GaN, InN and $In_xGa_{1-x}N$ alloys are included for comparison. The open-square and open-circle is the thermal conductivity of pure GaN (Ref. [106]) and pure InN (Ref. [107]) respectively. The dashed line is calculated for the limit of large layer thickness; the solid line is calculation for a layer thickness of d = 200 nm. (b) Ratio of the measured thermal conductivity from this work to the calculated thermal conductivity (Λ_{DCM}) at each thickness as a function of In content.(a)) matches the experimental values of pure InN and GaN. The thermal conductivity at each thicknesses is also calculated and plotted as the ratio of the measured thermal conductivity and the calculated thermal conductivity as a function of In composition in

Figure A.2(b). It is noted that the thermal conductivity of the alloy layer with x = 0.08 is higher than calculation by the model. One possibility is that the boundary scattering is not as high as prediction because of small acoustic impedance mismatch between the alloy layer and the GaN buffer layer.

A significant reduction of the $In_xGa_{1-x}N$ thermal conductivity below the prediction of the model is observed for In compositions in the range $0.2 < x < 0.9$. This suppression is stronger for $0.2 < x < 0.6$ which falls within the miscibility gap. This reduction is much larger than the uncertainties in the TDTR experiment of ± 10%. (The error bar is approximately the size of symbols used to plot the data points in Figure A.2(a)). While the model predicts well the thermal conductivity for the alloy with x = 0.98, the abrupt reduction of the thermal conductivity for $x < 0.9$ prevents using the possibility of bond-length disorder as an significant phonon-scattering mechanism in these alloys. Therefore the enhanced phonon scattering at $0.2 < x < 0.9$ is tentatively attributed to nanometer-scale compositional inhomogeneities in alloys that are thermodynamically unstable. [101,102] There has been no systematic study of the thermal conductivity of thermodynamically unstable alloys prior to this work but the strong reduction of thermal conductivity by the precipitation of nanometer scale second phase particles has been widely investigated. [130,131]

The existence of compositional inhomogeneities in $In_xGa_{1-x}N$ has been controversial, [132-134] partly because electron-beam damage during

imaging by TEM can generate changes in composition, and some of the early studies misinterpreted these experimental artifacts as compositional inhomogeneities formed during epitaxial growth. Low In content alloys have been best studied and most of these studies have concluded that for $x < 0.20$ in the form of thin layers lattice matched to GaN, the microscopic structure is best described as a random alloy. [135,136] The microstructure of higher concentration alloys and unstrained layers have been less studied. [102]

A.7 Conclusion

In conclusion, at low and high In concentrations ($x < 0.2$ and $x > 0.9$), the thermal conductivity of $In_xGa_{1-x}N$ is adequately described by a model based on phonon Rayleigh scattering of mass disorders. At intermediate compositions, a suppression in the thermal conductivity has been observed which has been attributed to nanometer-scale compositional inhomogeneities that strongly scatter thermal phonons.

REFERENCES

[1] R. W. Whatmore, Reports on Progress in Physics (ISSN 0034-4885) **49**, 1335 (1986).
[2] S. B. Lang, Physics Today **58**, 31 (2005).
[3] C. R. Bowen, J. Taylor, E. LeBoulbar, D. Zabek, A. Chauhan, and R. Vaish, Energy & Environmental Science **7**, 3836 (2014).
[4] G. Sebald, D. Guyomar, and A. Agbossou, Smart Mater Struct **18**, 125006 (2009).
[5] A. Glass and M. Lines, Phys Rev B **13**, 180 (1976).
[6] R. T. Smith and F. S. Welsh, J Appl Phys **42**, 2219 (1971).
[7] J. Mangin and A. Hadni, Physical Review B (Condensed Matter) **18**, 7139 (1978).
[8] Q. Peng and R. E. Cohen, Phys Rev B **83**, 220103 (2011).
[9] J. Karthik, J. C. Agar, A. R. Damodaran, and L. W. Martin, Phys. Rev. Lett. **109**, 257602 (2012).
[10] S. B. Lang, Nature **224**, 798 (1969).
[11] I. I. Lubomirsky and O. O. Stafsudd, Rev. Sci. Instrum. **83**, 051101 (2012).
[12] X. Li, S.-G. Lu, X.-Z. Chen, H. Gu, X.-S. Qian, and Q. M. Zhang, J. Mater. Chem. C **1**, 23 (2013).
[13] J. D. Zook and S. T. Liu, J Appl Phys **49**, 4604 (1978).
[14] H. H. S. Chang, R. W. Whatmore, and Z. Huang, J Appl Phys **106**, 4110 (2009).
[15] Y. Y. Yang, W. W. Guo, K. C. K. Pradel, G. G. Zhu, Y. Y. Zhou, Y. Y. Zhang, Y. Y. Hu, L. L. Lin, and Z. L. Z. Wang, Nano Lett **12**, 2833 (2012).
[16] M. Dawber, I. Farnan, and J. F. Scott, American Journal of Physics **71**, 819 (2003).
[17] S. Domanski, Proceedings of the Physical Society **72**, 306 (2002).
[18] L. Pintilie and M. Alexe, Appl. Phys. Lett. **87**, 112903 (2005).
[19] S. B. Lang and F. Steckel, Rev. Sci. Instrum. **36**, 929 (1965).
[20] A. M. Glass, J Appl Phys **40**, 4699 (1969).
[21] Z. Li, A. Sun, J. Wu, G. Xu, Y. Li, J. Jiang, and P. Cui, Materials Letters **63**, 2070 (2009).
[22] M. Davis, D. Damjanovic, and N. Setter, J Appl Phys **96**, 2811 (2004).
[23] A. Chynoweth, J Appl Phys (1956).
[24] S. B. Lang and D. K. Das-Gupta, Ferroelectrics **60**, 23 (1984).
[25] J. Scott, Annual Review of Materials Research (2011).
[26] S. Fähler, U. K. Rößler, O. Kastner, J. Eckert, G. Eggeler, H. Emmerich, P. Entel, S. Müller, E. Quandt, and K. Albe, Advanced Engineering Materials **14**, 10 (2011).
[27] J. Liu, T. Gottschall, K. P. Skokov, J. D. Moore, and O. Gutfleisch, Nature Materials **11**, 620 (2012).
[28] T. Furukawa, Ferroelectrics **57**, 63 (1984).
[29] G. Akcay, S. Alpay, and G. Rossetti Jr, J Appl Phys (2008).
[30] S. G. Lu, B. Rozic, Q. M. Zhang, Z. Kutnjak, and B. Neese, Appl. Phys. Lett. **98**, 2906 (2011).
[31] J. Karthik and L. W. Martin, Appl. Phys. Lett. **99**, 032904 (2011).
[32] X. Zhang, J. B. Wang, B. Li, X. L. Zhong, X. J. Lou, and Y. C. Zhou, J Appl Phys **109**, 126102 (2011).
[33] P. D. Thacher, J Appl Phys **39**, 1996 (1968).
[34] A. Mischenko, Q. Zhang, J. Scott, R. Whatmore, and N. Mathur, Science **311**, 1270 (2006).
[35] B. Neese, B. Chu, S.-G. Lu, Y. Wang, E. Furman, and Q. M. Zhang, Science **321**, 821 (2008).

[36] S. Kar-Narayan and N. Mathur, J Phys D Appl Phys **43**, 032002 (2010).
[37] Y. Bai, G. Zheng, and S. Shi, Appl. Phys. Lett. **96**, 192902 (2010).
[38] X. Li, X.-S. Qian, S. G. Lu, J. Cheng, Z. Fang, and Q. M. Zhang, Appl. Phys. Lett. **99**, 2907 (2011).
[39] S. G. Lu, B. Rozic, Q. M. Zhang, Z. Kutnjak, X. Li, E. Furman, L. J. Gorny, M. Lin, B. Malic, M. Kosec, R. Blinc, and R. Pirc, Appl. Phys. Lett. **97**, 2904 (2010).
[40] Y. Bai and G. Zheng, Appl. Phys. Lett. (2010).
[41] F. L. Goupil, A. Berenov, A.-K. Axelsson, M. Valant, and N. M. Alford, J Appl Phys **111**, 124109 (2012).
[42] I. I. Ponomareva and S. S. Lisenkov, Phys. Rev. Lett. **108**, 167604 (2012).
[43] M. Dawber and J. F. Scott, Reviews of Modern Physics **77**, 1083 (2005).
[44] D. M. Kim, C. B. Eom, V. Nagarajan, J. Ouyang, R. Ramesh, V. Vaithyanathan, and D. G. Schlom, Appl. Phys. Lett. **88**, 2904 (2006).
[45] V. Nagarajan, S. Prasertchoung, T. Zhao, H. Zheng, J. Ouyang, R. Ramesh, W. Tian, X. Q. Pan, D. M. Kim, C. B. Eom, H. Kohlstedt, and R. Waser, Appl. Phys. Lett. **84**, 5225 (2004).
[46] N. Setter, D. Damjanovic, L. Eng, G. Fox, S. Gevorgian, S. Hong, A. Kingon, H. Kohlstedt, N. Y. Park, G. B. Stephenson, I. Stolitchnov, A. K. Taganstev, D. V. Taylor, T. Yamada, and S. Streiffer, Journal of Applied … **100**, 051606 (2006).
[47] A. Sharma, Z. G. Ban, S. P. Alpay, and J. V. Mantese, Appl. Phys. Lett. **84**, 4959 (2004).
[48] L. Pintilie, I. Vrejoiu, D. Hesse, and G. LeRhun, Phys Rev B (2007).
[49] D. Cahill, Rev. Sci. Instrum. **75**, 5119 (2004).
[50] W. S. Capinski, H. J. Maris, T. Ruf, M. Cardona, K. Ploog, and D. S. Katzer, Physical Review B (Condensed Matter and Materials Physics) **59**, 8105 (1999).
[51] A. Schmidt, M. Chiesa, X. Chen, and G. Chen, Rev. Sci. Instrum. **79**, 064902 (2008).
[52] J. F. Scott, Science **315**, 954 (2007).
[53] S. B. Lang, Phys Rev B **4**, 3603 (1971).
[54] Y. Tang, S. Zhang, Z. Shen, W. Jiang, J. Luo, R. Sahul, and T. R. Shrout, J Appl Phys **114**, 4105 (2013).
[55] H. H. S. Chang and Z. Huang, Appl. Phys. Lett. **92**, 2903 (2008).
[56] K. H. Chew, F. G. Shin, B. Ploss, H. L. W. Chan, and C. L. Choy, J Appl Phys **94**, 1134 (2003).
[57] Y. Yvry, V. Lyahovitskaya, I. Zon, I. Lubomirsky, E. Wachtel, and A. L. Roytburd, Appl. Phys. Lett. **90**, 172905 (2007).
[58] N. Izyumskaya, Y. I. Alivov, S. J. Cho, H. Morkoç, H. Lee, and Y. S. Kang, Critical Revs. in Solid State & Mat. Sc. **32**, 111 (2007).
[59] J. Karthik, A. R. Damodaran, and L. W. Martin, Adv. Mater. Weinheim **24**, 1610 (2012).
[60] C. Hubert, J. Levy, E. J. Cukauskas, and S. W. Kirchoefer, Phys. Rev. Lett. **85**, 1998 (2000).
[61] K. R. Carroll, J. M. Pond, D. B. Chrisey, J. S. Horwitz, R. E. Leuchtner, and K. S. Grabowski, Appl. Phys. Lett. **62**, 1845 (1993).
[62] D. Tenne, A. Soukiassian, M. Zhu, A. Clark, X. Xi, H. Choosuwan, Q. He, R. Guo, and A. Bhalla, Phys Rev B **67**, 012302 (2003).
[63] M. Tyunina and J. Levoska, Phys Rev B **70**, 132105 (2004).
[64] R. J. Zednik, P. C. McIntyre, J. D. Baniecki, M. Ishii, T. Shioga, and K. Kurihara, J Appl Phys **101**, 066104 (2007).
[65] H. Kueppers, T. Leuerer, U. Schnakenberg, W. Mokwa, M. Hoffmann, T. Schneller, U. Boettger, and R. Waser, Sensors and Actuators a: Physical **97-98**, 680 (2002).
[66] J. F. Shepard, F. Chu, I. Kanno, and S. Trolier-McKinstry, J Appl Phys **85**, 6711

(1999).
[67] J. Karthik and L. W. Martin, Phys Rev B **84**, 24102 (2011).
[68] M. Botea, A. Iuga, and L. Pintilie, Appl. Phys. Lett. **103**, 232902 (2013).
[69] Y. Wang, J. Y. Park, Y. K. Koh, and D. G. Cahill, J Appl Phys **108**, 3507 (2010).
[70] D. Cahill, Rev. Sci. Instrum. (1990).
[71] K. Lefki and G. J. M. Dormans, J Appl Phys **76**, 1764 (1994).
[72] S. Boffi, G. Caglioti, and G. Cortellazzi, J. Phys. Chem Solids **39**, 5 (1978).
[73] R. W. Munn, Journal of Physics C: Solid State Physics **6**, 3213 (1973).
[74] S. V. Kalinin, B. Mirman, and E. Karapetian, Phys Rev B **76**, 212102 (2007).
[75] Y.-Z. Chen, T.-H. Liu, C.-Y. Chen, C.-H. Liu, S.-Y. Chen, W.-W. Wu, Z. L. Wang, J.-H. He, Y.-H. Chu, and Y.-L. Chueh, Acs Nano **6**, 2826 (2012).
[76] R. V. K. Mangalam, J. Karthik, A. R. Damodaran, J. C. Agar, and L. W. Martin, Adv Mater **25**, 1761 (2013).
[77] G. Suchaneck, G. Gerlach, and A. Deyneka, Mat. Res. Soc. .Proc. **718**, D8.4.1 (2002).
[78] S. Yamanaka, T. Maekawa, H. Muta, T. Matsuda, S.-I. Kobayashi, and K. Kurosaki, Journal of Solid State Chemistry **177**, 3484 (2004).
[79] F. M. Jaeger and W. A. Veenstra, Recl. Trav. Chim. Pays-Bas **53**, 677 (2010).
[80] J. Karthik, R. V. K. Mangalam, J. C. Agar, and L. W. Martin, Phys Rev B **87**, 024111 (2013).
[81] M. Grossmann, O. Lohse, D. Bolten, U. Boettger, T. Schneller, and R. Waser, J Appl Phys **92**, 2680 (2002).
[82] M. B. Okatan and S. P. Alpay, Appl. Phys. Lett. **95**, 2902 (2009).
[83] L. J. Dunne, M. Valant, G. Manos, A.-K. Axelsson, and N. Alford, Appl. Phys. Lett. **93**, 122906 (2008).
[84] M. Valant, L. J. Dunne, A.-K. Axelsson, N. M. Alford, G. Manos, J. Peräntie, J. Hagberg, H. Jantunen, and A. Dabkowski, Phys Rev B **81**, 214110 (2010).
[85] J. Hagberg, A. Uusimaki, and H. Jantunen, Appl. Phys. Lett. **92**, 132909 (2008).
[86] G. Akcay, S. P. Alpay, J. V. Mantese, and G. A. Rossetti, Appl. Phys. Lett. **90**, 252909 (2007).
[87] V. Nagarajan, A. Stanishevsky, L. Chen, T. Zhao, B. T. Liu, J. Melngailis, A. L. Roytburd, R. Ramesh, J. Finder, Z. Yu, R. Droopad, and K. Eisenbeiser, Appl. Phys. Lett. **81**, 4215 (2002).
[88] D. V. Taylor and D. Damjanovic, Appl. Phys. Lett. **76**, 1615 (2000).
[89] B. Bhatia, J. Karthik, D. G. Cahill, L. W. Martin, and W. P. King, Appl. Phys. Lett. **99**, 3103 (2011).
[90] S. Lisenkov and I. Ponomareva, Phys Rev B **86**, 104103 (2012).
[91] E. E. Bonnot, R. R. Romero, L. L. Mañosa, E. E. Vives, and A. A. Planes, Phys. Rev. Lett. **100**, 125901 (2008).
[92] J. J. Ebelmen, Ann **57**, 1 (1846).
[93] V. G. Kessler, G. I. Spijksma, G. A. Seisenbaeva, S. Håkansson, D. H. A. Blank, and H. J. M. Bouwmeester, J Sol-Gel Sci Technol **40**, 163 (2006).
[94] J. Livage, M. Henry, and C. Sanchez, Progress in Solid State Chemistry **18**, 259 (1988).
[95] G. L. Brennecka, J. F. Ihlefeld, J.-P. Maria, B. A. Tuttle, and P. G. Clem, Journal of the American Ceramic Society **93**, 3935 (2010).
[96] A. Dixit, S. B. Majumder, A. Savvinov, R. S. Katiyar, R. Guo, and A. S. Bhalla, Materials Letters **56**, 933 (2002).
[97] T. Tani, J.-F. Li, D. Viehland, and D. A. Payne, J Appl Phys **75**, 3017 (1994).
[98] R. W. Schwartz, T. J. Boyle, S. J. Lockwood, M. B. Sinclair, D. Dimos, and C. D. Buchheit, Integrated Ferroelectrics **7**, 259 (1995).
[99] J. M. Phillips, M. E. Coltrin, M. H. Crawford, A. J. Fischer, M. R. Krames, R. Mueller-Mach, G. O. Mueller, Y. Ohno, L. E. S. Rohwer, J. A. Simmons, and J. Y.

Tsao, Laser & Photon. Rev. **1**, 307 (2007).
[100] D.-W. Oh, J. Ravichandran, C.-W. Liang, W. Siemons, B. Jalan, C. M. Brooks, M. Huijben, D. G. Schlom, S. Stemmer, L. W. Martin, A. Majumdar, R. Ramesh, and D. G. Cahill, Appl. Phys. Lett. **98**, 221904 (2011).
[101] I. Ho and G. Stringfellow, Appl. Phys. Lett. **69**, 2701 (1996).
[102] G. B. Stringfellow, J Cryst Growth **312**, 735 (2010).
[103] B. N. Pantha, R. Dahal, J. Li, J. Y. Lin, H. X. Jiang, and G. Pomrenke, Appl. Phys. Lett. **92**, 042112 (2008).
[104] E. N. Hurwitz, M. Asghar, A. Melton, B. Kucukgok, L. Su, M. Orocz, M. Jamil, N. Lu, and I. T. Ferguson, J Electron Mater **40**, 513 (2011).
[105] J. P. Dismukes, L. Ekstrom, E. F. Steigmeier, I. Kudman, and D. S. Beers, J Appl Phys **35**, 2899 (1964).
[106] G. Slack, L. Schowalter, D. Morelli, and J. Freitas, J Cryst Growth **246**, 287 (2002).
[107] A. X. Levander, T. Tong, K. M. Yu, J. Suh, D. Fu, R. Zhang, H. Lu, W. J. Schaff, O. Dubon, W. Walukiewicz, D. G. Cahill, and J. Wu, Appl. Phys. Lett. **98**, 012108 (2011).
[108] Y. K. Koh, Y. Cao, D. G. Cahill, and D. Jena, Adv Funct Mater **19**, 610 (2009).
[109] D. Florescu, V. Asnin, F. Pollak, and A. Jones, Applied Physics … (2000).
[110] V. Asnin, F. Pollak, J. Ramer, and M. Schurman, Applied Physics … (1999).
[111] E. Sichel, J Phys Chem Solids (1977).
[112] P. Carruthers, Reviews of Modern Physics (1961).
[113] B. Pantha, J. Li, and J. Lin, Appl. Phys. Lett. (2008).
[114] Z. Liliental-Weber, D. N. Zakharov, K. M. Yu, J. W. Ager, W. Walukiewicz, E. E. Haller, H. Lu, and W. J. Schaff, Journal of Electron Microscopy **54**, 243 (2005).
[115] B. Liu, W. Luo, R. Zhang, Z. Zou, Z. Xie, and Z. Li, … Status Solidi (C) (2010).
[116] B. Pantha, J. Li, and J. Lin, Appl. Phys. Lett. (2010).
[117] R. Singh, D. Doppalapudi, T. Moustakas, and L. Romano, Appl. Phys. Lett. **70**, 1089 (1997).
[118] K. Kang, Y. K. Koh, C. Chiritescu, X. Zheng, and D. G. Cahill, Rev. Sci. Instrum. **79**, 114901 (2008).
[119] S. Krukowski, A. Witek, J. Adamczyk, and J. Jun, … And Chemistry of Solids (1998).
[120] J. Leitner, A. Strejc, D. Sedmidubsky, and K. Ruzicka, Thermochim Acta **401**, 169 (2003).
[121] Z. Su, L. Huang, F. Liu, J. P. Freedman, L. M. Porter, R. F. Davis, and J. A. Malen, Appl. Phys. Lett. **100**, 201106 (2012).
[122] A. Sztein, H. Ohta, J. E. Bowers, S. P. Denbaars, and S. Nakamura, J Appl Phys **110**, 123709 (2011).
[123] J. Callaway, Phys Rev (1959).
[124] D. Morelli and J. Heremans, Phys Rev B (2002).
[125] D. Cahill, F. Watanabe, and A. Rockett, Phys Rev B (2005).
[126] C. Herring, Phys Rev (1954).
[127] P. Klemens, Proceedings of the Physical Society. Section A (1955).
[128] B. Abeles, Phys Rev (1963).
[129] J. Zou, D. Kotchetkov, and A. Balandin, Journal of Applied … (2002).
[130] N. Mingo, D. Hauser, N. P. Kobayashi, M. Plissonnier, and A. Shakouri, Nano Lett **9**, 711 (2009).
[131] Y. K. Koh, S. L. Singer, W. Kim, J. M. O. Zide, H. Lu, D. G. Cahill, A. Majumdar, and A. C. Gossard, J Appl Phys **105**, 054303 (2009).
[132] T. Smeeton, M. Kappers, J. Barnard, M. Vickers, and C. Humphreys, Appl. Phys. Lett. **83**, 5419 (2003).
[133] C. Kisielowski and T. P. Bartel, Appl. Phys. Lett. **91**, 176101 (2007).

[134] M. J. Galtrey, R. A. Oliver, M. J. Kappers, C. J. Humphreys, D. J. Stokes, P. H. Clifton, and A. Cerezo, Appl. Phys. Lett. **90**, 061903 (2007).
[135] T. Schulz, T. Remmele, and T. Markurt, Journal of Applied … (2012).
[136] V. B. Oezdoel, C. T. Koch, and P. A. van Aken, J Appl Phys **108**, 056103 (2010).